Magnetic-Field-Tuned Quantum Phase Transitions Exhibited by Indium Oxide

A THESIS

SUBMITTED TO THE FACULTY OF THE GRADUATE SCHOOL

OF THE UNIVERSITY OF MINNESOTA

BY

Nicholas Lewellyn

IN PARTIAL FULFILLMENT OF THE REQUIREMENTS

FOR THE DEGREE OF

Doctor of Philosophy

A. M. Goldman

July, 2021

Acknowledgements

I would like to thank my family for their support throughout my education. Their encouragement has helped me to finish this work and get to this point. They have supported my interest in science since I was a young child.

I would like to thank my advisor, Allen M. Goldman for his support and guidance. His mentorship, knowledge, patience, and intuition were immensely helpful throughout my research and the writing of my thesis.

Thanks to everyone that I worked with and learned from throughout my time as part of Goldman's group including: Terry Bretz-Sullivan, Boyi Yang, JJ Nelson, and Ilana Percher. I have learned so much about running various laboratory equipment from them. I would also like to thank my collaborators, Aviad Frydman and Irina Volotsenko for growing the films that I studied. Additionally, Thomas Vojta for helping to explain the data that I measured.

I would also like to acknowledge that this work was supported by the National Science Foundation under Grants No. DMR-1209578 and No. DMR-1704456. Additionally, portions of this work were conducted in the Minnesota Nano Center, which is supported by the National Science Foundation through the National Nano Coordinated Infrastructure Network (NNCI) under Award No. ECCS-1542202.

Abstract

The magnetic-field-tuned quantum superconductor-insulator transitions of disordered amorphous indium oxide films are a paradigm in the study of quantum phase transitions, and typically exhibit power-law scaling behavior. The properties of these films can be tuned by varying the carrier concentration and disorder which is done by adjusting the oxygen partial pressure during deposition or by annealing after deposition. These films are known to undergo disorder, magnetic field, and charge carrier density-tuned transitions, most commonly superconductor-insulator transitions. A pair of indium oxide films exhibiting an unconventional superconductor-metal transition will be discussed in this dissertation along with the noise properties of a film exhibiting a more conventional transition.

For superconducting indium oxide films with low disorder, such as the ones reported on in Chapter 4, the high-field state appears to be a quantum-corrected metal. Resistance data across the superconductor-metal transition in these films are shown here to obey an activated scaling form appropriate to a quantum phase transition controlled by an infinite randomness fixed point in the universality class of the random transverse-field Ising model. Collapse of the field-dependent resistance vs. temperature data is obtained using an activated scaling form appropriate to this universality class, using values determined through a modified form of power-law scaling analysis. This exotic behavior of films exhibiting a superconductor-metal transition is caused by the dissipative dynamics of superconducting rare regions immersed in a metallic matrix, as predicted by a recent renormalization group theory. The smeared crossing points of isotherms observed are due to corrections to scaling which are expected near an infinite randomness critical point, where the inverse disorder strength acts as an irrelevant scaling variable.

For superconducting indium oxide films with higher disorder, a more conventional superconductor-insulator transition is observed. Low frequency resistance measurements performed on such a film are shown in this dissertation. Contrary to initial expectations there were no significant changes in the noise properties near the quantum critical point. However, it was found that the noise varied in a way that was consistent with predictions based on a percolation model. Specifically, the noise properties suggest that the superconductor-insulator transition can be modeled by p-model percolation. This model is based on random Josephson junction array models which have been used extensively to explain the properties of granular superconductors.

Contents

Acknowledgements **i**

Abstract **ii**

List of Figures **vii**

1 Introduction **1**

1.1 Overview of Results 1

1.2 Overview of Superconductivity 2

1.3 Quantum Phase Transitions 6

1.4 Scaling Analysis and Universality Classes 7

1.5 Josephson Junctions and Arrays 10

2 Characteristics of Indium Oxide Films **15**

2.1 Introduction 15

2.2 General Properties of Indium Oxide 16

2.3 Doping and Disorder 16

2.4 Photolithography and Sample Fabrication 18

2.5 Annealing of Indium Oxide 21

2.6 Effective Dimensionality of Films 24

2.7 Conclusions 26

3 Experimental Techniques and Limitations 28

3.1 Introduction 28

3.2 Temperature Control 28

3.3 Sample Temperature 30

3.4 Grounding/Circuit Isolation 33

3.5 Filtering and Noise Induced Heating 36

3.6 Conclusions 37

4 Indium Oxide Films Exhibiting An Infinite Randomness Fixed Point 39

4.1 Introduction 39

4.2 History 41

4.3 The Physics of the Griffiths Effect 41

4.4 Possible Observation of Quantum Griffiths Effects by Others 45

4.5 Transport Measurements in a Perpendicular Magnetic Field 47

4.6 Power-law Scaling Analysis 66

4.7 Power-law vs. Activated Scaling 73

4.8 Activated Scaling 75

4.9 Corrections 83

4.10 Conclusions 84

5 Low-Frequency Noise and Percolation Near the SIT 87

5.1 Introduction 87

5.2 Types of Noise 90

5.3 Percolation 93

5.4 The Perpendicular Magnetic-Field-Tuned SIT 94

5.5 Scofield Noise Measurement Technique 106

5.6 Resistance Fluctuation Measurement Apparatus 112
5.7 Resistance Fluctuations Exhibited by Indium Oxide 117
5.8 Noise Exponents and Percolation 130
5.9 Conclusions 147

6 Conclusion **150**

References **154**

Appendices **170**

List of Figures

1.1 Superconductivity of Mercury 4
1.2 Generic Phase Diagram of Quantum Phase Transition 8
1.3 Diagram of Josephson Junction 14
2.1 AFM Scan 17
2.2 Example of Annealing 23
2.3 Initial Characterization of InOx_061520_1 25
3.1 Current Induced Heating 32
3.2 Filtering Arrangements 38
4.1 Quantum Griffiths Effect Observation 48
4.2 Griffiths Experiment Sample Geometry 49
4.3 AFM Trace 50
4.4 Initial Characterization of Batch 13 Chip 3 53
4.5 Initial Characterization of Batch 15 Chip 3 54
4.6 Detailed Sample Characterization of Batch 15 Chip 3 56
4.7 2D Weak Localization: Batch 15 Chip 3 58
4.8 Hall Resistance 60
4.9 Magnetoresistance Isotherms: Batch 15 Chip 3 62
4.10 Detailed Characterization of Batch 15 Chip 2 64
4.11 2D Weak Localization: Batch 15 Chip 2 65

4.12 Magnetoresistance Isotherms: Batch 15 Chip 2 67
4.13 Crossing Magnetic Field vs. Temperature: Batch 15 Chip 3 69
4.14 νz vs. Temperature: Batch 15 Chip 3 71
4.15 νz vs. Crossing Field: Batch 15 Chip 3 72
4.16 Crossing Magnetic Field vs. Temperature: Batch 15 Chip 2 74
4.17 νz vs. Crossing Field Batch: 15 Chip 2 76
4.18 νz vs. Temperature: Batch 15 Chip 2 77
4.19 Activated Scaling Plot for Batch 15 Chip 2 79
4.20 Quality of Scaling Collapse 81
5.1 Diamagnetic Response From Scanning SQUID 91
5.2 Noise Measurement Sample Geometry 96
5.3 Noise Measurement Sample Initial Characterization 97
5.4 Solution to Laplace's Equation for Hall Bar 100
5.5 Resistance vs. Temperature: InOx_061520_2 102
5.6 Hopping Conduction Plot: InOx_061520_2 103
5.7 Magnetoresistance for InOx_061520_2 105
5.8 Power-law Scaling Plot 107
5.9 Four-Probe Noise Measurement Circuit 108
5.10 Five-Probe Noise Measurement Circuit 110
5.11 SR560 Noise Contour 111
5.12 FWHM of Resistance Fluctuations 119
5.13 Quality of Gaussian Fit Map 121
5.14 Corrected Power Spectra 123
5.15 Background Noise Power Spectra 124
5.16 Hooge Parameter vs. Sheet Resistance 126
5.17 Second Spectra Slopes vs. Magnetic Field 128

5.18 Noise at 1Hz 131
5.19 Temperature Fluctuation Noise 132
5.20 Noise Properties of YBCO Film 138
5.21 Hooge Parameter vs. Sheet Resistance Fitting 140
5.22 Hooge parameter vs. Current: 100mK 143
5.23 Hooge parameter vs. Current: 5K 144
5.24 Hooge parameter vs. Magnetic Field 145
5.25 Hooge parameter vs. Sheet Resistance Slope 148

Chapter 1

Introduction

1.1 Overview of Results

The main focus of this dissertation will be two different quantum phase transitions that were exhibited by amorphous indium oxide thin films of varying degrees of disorder. In the next chapter some of the properties of indium oxide will be discussed, starting with some general properties of the material. Additionally, techniques for tuning the carrier concentration and disorder present in films will be discussed. This is of vital importance because it plays a significant role in whether or not a quantum phase transition occurs and what type. The photolithography and deposition techniques used in the fabrication of the films studied will be described in detail. Finally, the role that annealing plays in sample preparation and how it can be used to tune the disorder will be discussed.

Chapter three will describe some of the experimental techniques that were used while characterizing the films and the limitations of the measurements. Since quantum phase transitions occur in the limit of zero temperature and low temperatures are required to observe the effects of quantum fluctuations, temperature control becomes a significant concern. The equipment used for temperature control of the Oxford dilution

refrigerators will be discussed, as will the determination of the sample temperature. Lastly, circuit grounding and isolation for the measurement circuit and the importance of electrical filtering will be detailed.

The focus of Chapter 4 will be concerned with the behavior of relatively low disorder indium oxide films. These films did not undergo a superconductor-insulator transition that follows power-law scaling, as has been commonly observed. Instead, these films underwent a superconductor-metal transition. Another difference was instead of a single crossing in the magnetoresistance isotherms corresponding to the critical field, there was a temperature dependent, or smeared crossing. In this chapter it will be shown that the transition can be fit by activated scaling and it will be argued that the quantum Griffiths effect was observed.

In Chapter 5 the resistance fluctuations of a more disordered indium oxide film will be discussed. This film exhibited a superconductor-insulator transition and followed power-law scaling as is typical for amorphous indium oxide films. The resistance noise will be characterized in a few different ways to gain insight on the nature of the transition. It will be proposed that the observed noise is consistent with a model called p-model percolation that is based on the random switching of Josephson junctions in a random array.

1.2 Overview of Superconductivity

Superconductivity has two defining phenomenological characteristics, the occurrence of zero electrical resistance and the Meissner-Ochsenfeld effect [1]. Below some critical temperature, T_c, superconductors lose all electrical resistance and superconducting rings can sustain a supercurrent with no decay. Experiments by File and Mills [2] on such persistent currents in superconducting rings have shown that once set up there is no measurable decrease in the current after a year.

The other defining characteristic is the Meissner-Ochsenfeld effect. This effect is the expulsion of magnetic fields from the material. Any applied magnetic field below some critical field, H_c, will only be able to penetrate a superconductor a short distance and exponentially decay moving in from the surface. The characteristic distance over which the field decays is called the penetration depth, λ.

Superconductivity was discovered by Kamerlingh Onnes in 1911 [3]. The first material known to be superconducting was mercury and it had a critical temperature of 4.19K. Since its discovery there has been great interest in explaining why superconductivity occurs and in finding materials with higher critical temperatures. Since 1911 much progress has been made on both fronts. Materials with much higher critical temperatures have been found, including $YBa_2Cu_3O_{7-x}$, the first superconductor with a critical temperature above the boiling point of liquid nitrogen, found in 1987. Its transition temperature is $T_c = 92K$. Many other high T_c materials, such as other cuprates, borides, pnictides, and hydrides have been found since then with the current record T_c value being 262K for yttrium superhydride, but only under extremely high pressure [4].

The discovery of both ordinary and high T_c superconductors has allowed the development of many technological applications for superconducting materials including superconducting quantum interference devices (SQUIDs), sensors and computer elements based on superconducting devices, high-field magnets for use in magnetic resonance imaging (MRI) machines, materials research, and particle accelerators. Further progress in the processing of wire could lead to commercially viable, large scale, technological applications, such as much more efficient transmission lines, electric motors, generators and electromagnets. Superconducting devices may be the hardware employed in future quantum computers.

Since the discovery of superconductivity, theories have been developed to describe the phenomenon. The Ginzburg-Landau theory is phenomenological in nature. In

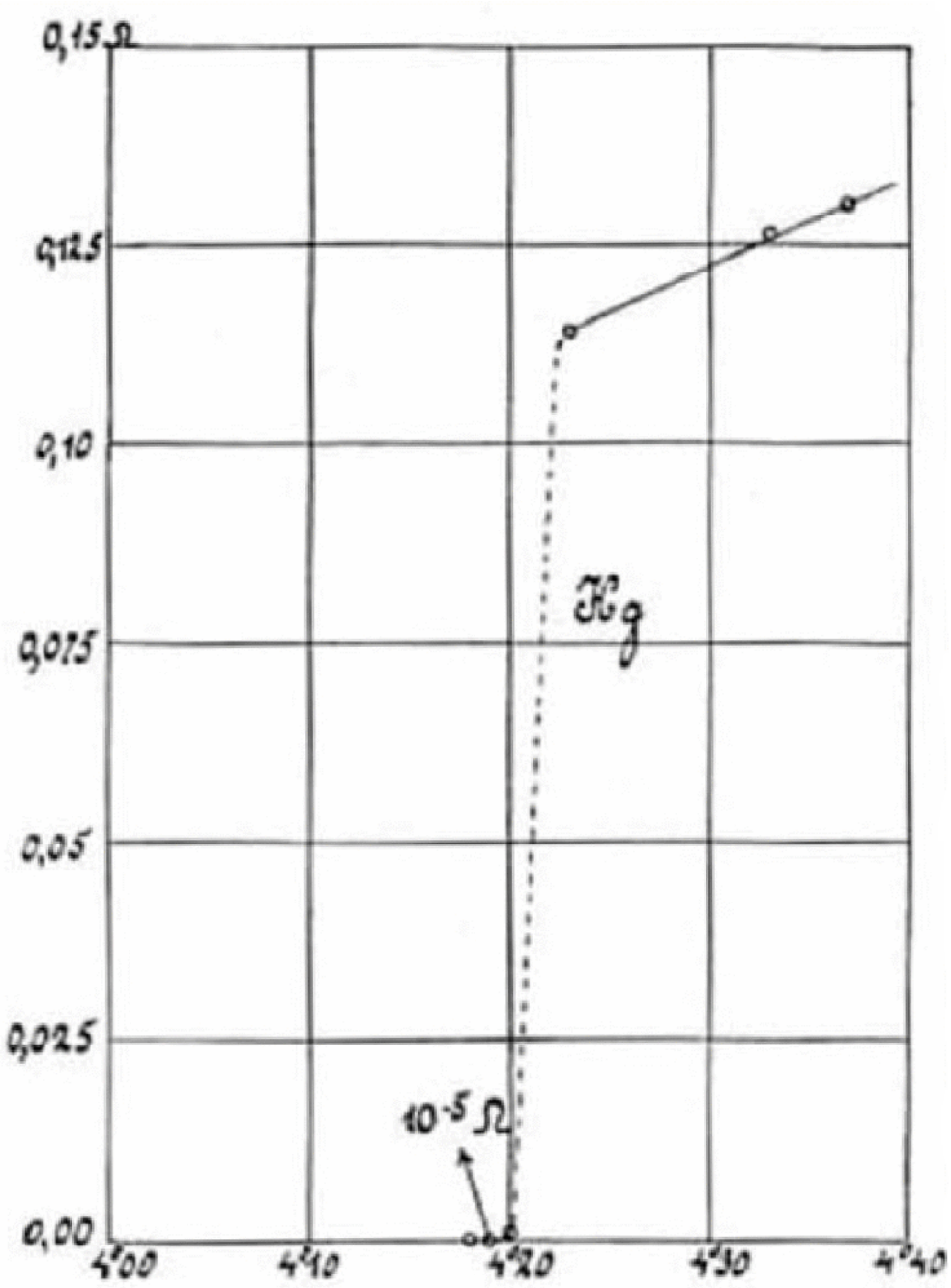

Figure 1.1: Above is a resistance versus temperature plot for mercury. This plot was the made by Kamerlingh Onnes and it shows the discovery of superconductivity [3].

this theory a complex valued pseudo-wavefunction, or order parameter $\psi(r)$, is used to describe the system. Specifically, the density of superconducting electrons as a function of position is represented by $|\psi(r)|^2$. The free energy density of the system is taken to be

$$f = f_{n0} + \alpha|\psi|^2 + (\beta/2)|\psi|^4 + \frac{1}{2m^*}|[\frac{\hbar}{i}\nabla - \frac{e^*}{c}A]\psi|^2 + \frac{h^2}{8\pi} \tag{1.1}$$

where A is the magnetic vector potential and h is the magnetic field. From equation 1.1 the critical temperature, critical field, penetration depth, coherence length and various other properties can be inter-related using experimental data.

Minimizing the free energy from equation 1.1 using variational methods results in the Ginzburg-Landau equations. From these equations it can be shown that solutions fall into one of two different categories depending on the energy of the superconducting domain wall. One group of solutions has positive surface energy and the other has negative surface energy. The two groups of solutions correspond to type 1 and type 2 superconductors, respectively. Type 1 superconductors allow no magnetic field to penetrate the bulk until the critical field is reached. Type 2 superconductors have two critical fields, H_{c1}, below which no magnetic field penetrates the bulk, and H_{c2}, above which superconductivity is completely suppressed. Between those two critical fields some magnetic flux can penetrate the superconductor forming a lattice of vortices.

The BCS theory, in contrast with the macroscopic Ginzburg-Landau theory, is a microscopic theory. Bardeen, Cooper, and Schrieffer proposed the theory in 1957 [5]. They showed that a weak attraction between electrons mediated by phonons could cause the formation of bound pairs, called Cooper pairs. This leads to a condensate and a variety of predictions that were verified by experiments. The BCS theory can be used to derive the Ginzburg-Landau equations, connecting the macroscopic phenomenological theory with microscopic theory. The phonon mediated singlet s-wave pairing of BCS theory does not describe many of the newer materials found to be superconducting, in

which various combinations of higher angular momentum pairing, triplet pairing, and magnetic excitation moderated pairing may be relevant, depending upon the details of the material.

The BSC theory does not describe superconductors such as the cuprates, which exhibit d-wave pairing [6]. As mentioned above, it does not describe the pairing state of some of the more exotic materials recently found to exhibit superconductivity, an example of which was shown by Hillier et. al. [7]. I will not discuss the issues associated with these materials, as the films investigated were conventional BCS superconductors.

1.3 Quantum Phase Transitions

A phase transition is a change in the properties of a substance, as its environment is changed only infinitesimally [8]. This infinitesimal change can be in the temperature, pressure, magnetic field, etc. Some examples include the superfluid transition of He, the melting of ice into water, ferromagnetic transitions, and superconducting transitions. These transitions can be grouped into one of two groups, based on how abrupt the transition is. First order transitions have discontinuities in the entropy and volume, which are first derivatives of the Gibbs free energy, at the phase boundary and involve latent heat. Continuous, or second-order transitions have discontinuities in higher order derivatives of the Gibbs free energy and have a diverging correlation length at the critical point. These transitions do not involve latent heat, but have critical order parameter fluctuations, resulting in divergent thermodynamic variables as the transition temperature is approached.

Everyday examples of phase transitions are classical phase transitions since they occur at nonzero temperature. They occur when the Gibbs free energies of the two states are equal. This quantifies the competition between the internal energy of a system and its entropy. Quantum phase transitions are different in that they occur at

zero temperature [9]. One example of a quantum phase transition is superconductor-insulator transitions (SIT) in two dimensions. One of the most studied systems that undergo an SIT is the field tuned transition of amorphous indium oxide.

Quantum phase transitions occur when some tuning parameter is varied and causes a change in the ground state of the system. The tuning parameter could be a property such as the applied magnetic field, disorder, charge density, or doping. The point at which the transition occurs is the quantum critical point. Crucially, even though quantum phase transitions occur at zero temperature, their presence can still influence the properties of a system at low but finite temperatures. This is possible because quantum fluctuations of the order parameter associated with the transition, can persist to nonzero temperatures. Specifically, in the regime where $\hbar\omega > k_B T$, quantum fluctuations will be dominant over thermal fluctuations. This restriction to low temperatures necessitates the use of cryogenic equipment to study these transitions.

1.4 Scaling Analysis and Universality Classes

To study direct quantum phase transitions, of the simplest two-dimensional superconducting systems, such as those which belong to the (2+1) dimensional XY universality class, it is common to apply a scaling analysis to resistance data that is measured at finite temperature [9]. Typically, the first step is to find the critical value of the tuning parameter. This is done by generating a series of constant temperature isotherms where the tuning, or control parameter is varied. At the critical value of this parameter, the resistance of the system is expected to be temperature independent. This point is easily identified as the point where the isotherms cross. Once the critical value is found, the control parameter can be defined.

The control parameter is a measure of how far the system is from criticality and is

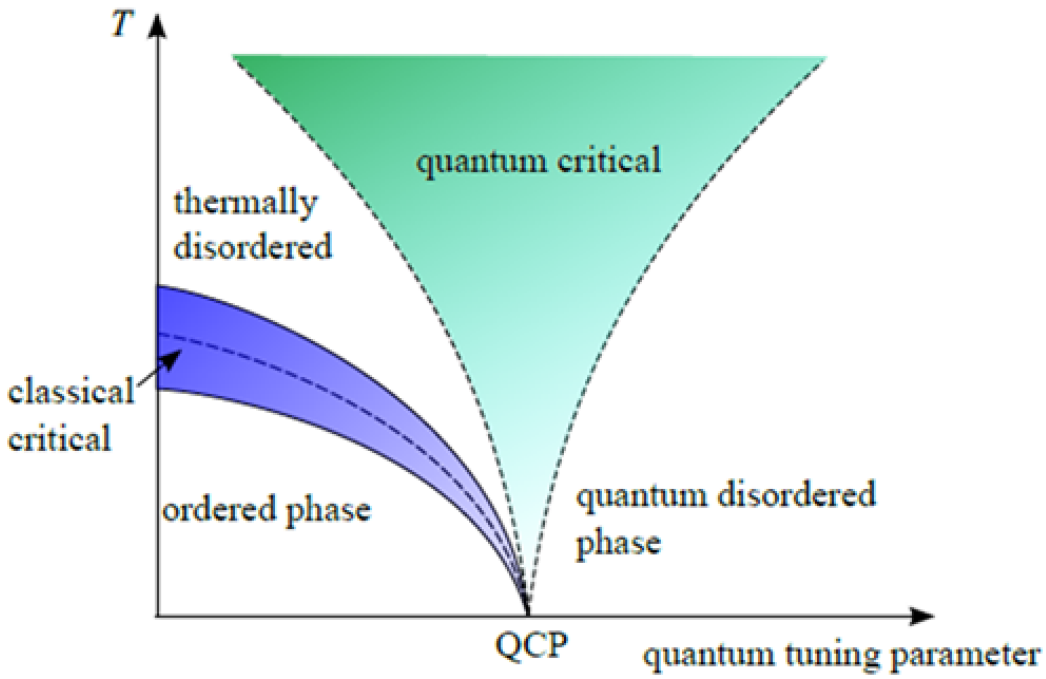

Figure 1.2: Phase diagram for a generatic system that undergoes a quantum phase transition [10].

given by,

$$\delta = |g - g_c|/g_c \tag{1.2}$$

where g is a measure of the tuning parameter and g_c is the critical value. Near the quantum critical point important properties can be described as functions of the control parameter. For example, the correlation length can be written as $\xi \propto |\delta|^{-\nu}$ and the dynamical correlation length as $\xi_\tau \propto \xi^z$ where ν and z are the correlation length exponent and dynamical critical exponent, respectively. Additionally, the resistance of the system can be written, in the case of power-law scaling, as

$$R = R_c F[\delta/T^{1/(\nu z)}, \delta/E^{\nu(z+1)}] \tag{1.3}$$

where R_c is the resistance at the critical point, E is the in-plane electric field, and F is some system specific function [11].

The next step is to plot the resistance versus $\delta/T^{1/(\nu z)}$ for the lowest temperature isotherm. If a quantum phase transition did occur and the proper scaling form is applied, there will be some value of νz that will result in the higher temperature isotherms collapsing onto the lowest temperature curve. With this technique it is not necessary to know the detailed form of the function F. The exponent product can be found numerically. An example of a well collapsed scaling plot is shown in Chapter 5. The combination of the scaling form and the resulting exponent product can be used to identify the universality class to which the transition belongs.

An important caveat regarding the above analysis is that there is always the possibility that below the temperature range spanned by the measurements, some new physics becomes relevant, resulting in the scaling analysis breaking down. It is therefore essential to carry out the measurements at the lowest temperatures that are available.

The universality class to which a transition belongs is independent of the microscopic details of the system. Instead, it depends on the symmetry, dimensionality, and

interaction range. This provides a useful tool to group transitions in seemingly very different systems and to understand the differences between transitions occurring in the same system but as a response to different tuning parameters. Some examples of relevant universality classes include the (2+1)D XY model, random transverse-field Ising model, percolation, etc. Examples of systems belonging to the random transverse field Ising model and the percolation model will be discussed in later chapters.

1.5 Josephson Junctions and Arrays

A Josephson junction consists of two superconducting electrodes that are separated by a barrier. This barrier can be an insulating or a semiconducting barrier, a constriction consisting of normal metal, or a constriction of weakly superconducting material. The latter are usually called weak links. These junctions, or weak links can support a supercurrent passing through if the critical current, I_c, is not exceeded. When the critical current is exceeded and a voltage develops across the junction or weak link, an AC supercurrent flows across the junction. These two behaviors are the DC and AC Josephson effects.

The simplest way to obtain a qualitative understanding of Josephson effects is to employ the Ginzburg-Landau theory which uses a complex valued order parameter to describe the system. Like all complex numbers, this value can be expressed in terms of a magnitude and phase. Josephson [13] predicted that the current passing through the junction with no applied voltage would be

$$I_s = I_c \sin(\Delta\phi) \tag{1.4}$$

where ϕ is the phase difference between the superconducting electrodes on either end of the junction. Additionally, with a DC voltage across the junction the phase will change

as a function of time,

$$d(\Delta\phi)/dt = 2eV/\hbar \tag{1.5}$$

resulting in an AC current with an amplitude of I_c and a frequency 2eV/h. The critical current is determined by microscopic properties of the barrier.

Combining equation 1.4 and equation 1.5 the coupling energy of the junction can be found to be,

$$F = const.\text{–}(\hbar I_c/2e)\cos(\Delta\phi) \tag{1.6}$$

by integrating the electrical work done to change the phase [9]. This equation can be further generalized by writing it in terms of a gauge-invariant phase. This is done by replacing $\Delta\phi$ with γ, where

$$\gamma \equiv \delta\phi - (2\pi/\Phi_0)\int A * ds \tag{1.7}$$

and Φ_0 is the magnetic flux quantum.

For the case of two junctions incorporated in a superconducting loop, such as in a superconducting quantum interference device (SQUID), the gauge invariant phase is crucial for determining the current through the device. Combining equation 1.7 with the fact that the phase has to be single valued results in,

$$\gamma_1 - \gamma_2 = [2\pi\Phi/\Phi_0](mod 2\pi) \tag{1.8}$$

where Φ is the magnetic flux enclosed by the loop. Comparing equation 1.8 with equation 1.4, it is clear that the maximum current is passed through the set of junctions when the phase difference across each junction is $\pi/2$ and the phase difference between the two, $\gamma_1 - \gamma_2$, is zero. It can be shown that the maximum current through the junction as a function of the flux enclosed is,

$$I_m = 2I_c|\cos(\pi\Phi/\Phi_0)| \tag{1.9}$$

These results for a loop consisting of two junctions can be generalized further for the case of a large array of Josephson junctions.

There has been a significant amount of theoretical and experimental work done on the case of large arrays of Josephson junctions. Comparing with the two junction case, it is clear that the phase difference between junctions and thus the maximum current that can flow between junctions is dependent on the applied magnetic field. As the field increases, the phase difference between junctions enclosing flux will increase and modulate the current that can flow through that set of junctions. It also decreases the coupling energy of the junctions. Eventually, the charging energy associated with the capacitance of the junctions, or the thermal energy that they experience, will exceed the coupling energy and the junction will no longer be able to pass a supercurrent [14].

As the magnetic field further increases, the coupling between progressively more junctions is suppressed. Eventually a sufficiently large number of junctions can be suppressed enough that the network as a whole is no longer able to pass a supercurrent. This can lead to metallic or insulating behavior depending on the nature of the barriers of the junctions. At even higher fields, the superconductivity of the electrodes themselves is suppressed as the critical field of the superconducting material is reached. This results in a two stage transition [15].

In a two stage transition, with weak tunneling, the resistance will initially increase with increased applied perpendicular magnetic field. This will progressively suppress the Josephson coupling between grains. However, once the Josephson coupling is suppressed, continued increasing of the field will reduce the energy gap in the grains. This will start to reduce the resistance of the array.

The Josephson junction array model has been applied to granular superconducting thin films [16]. In this case the superconducting grains are Josephson coupled with random coupling energies between individual grains. This results in a random critical

current between individual grains and a random magnetic flux necessary for the coupling energy to be reduced to less than the charging energy. This model has been used to successfully explain superconductor-insulator transitions in some thin films.

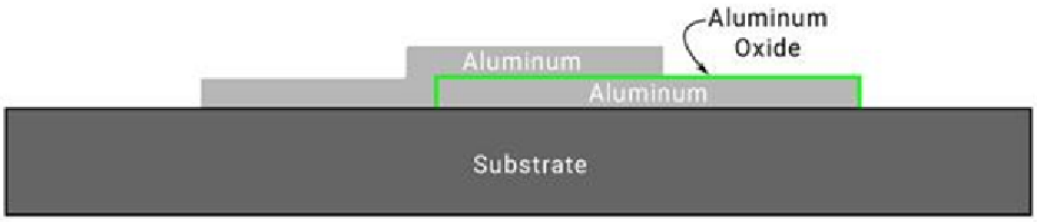

Figure 1.3: Diagram of a typical Josephson junction consisting of two aluminum superconducting electrodes separated by an insulating barrier made of aluminum oxide [12].

Chapter 2

Characteristics of Indium Oxide Films

2.1 Introduction

Indium oxide, In_2O_3, is a material that has been studied extensively for decades. It is one of the most commonly studied materials in the context of quantum phase transitions. The first reported example of a magnetic-field-tuned superconductor-insulator transition was observed in an amorphous indium oxide thin film [17]. It has also been studied and used in industry. One of its most common industrial uses is in the form of tin doped indium oxide for use in transparent conductive coatings, which are useful in numerous applications. Its properties can vary significantly depending on the growth conditions, including temperature and oxygen partial pressure, and disorder. For example, the carrier concentration can be tuned during deposition. Additionally, the disorder can be tuned both during deposition and through annealing. As with many thin film devices, indium oxide samples can be patterned using standard photolithography techniques on standard silicon wafers.

2.2 General Properties of Indium Oxide

Indium oxide is a solid that can range from having an amorphous structure to polycrystalline to crystalline. The structure is dependent on growth temperatures with higher temperatures resulting in a crystalline structure. It can take one of two crystal structures, cubic or rhombohedral. The rhombohedral structure is less common and is produced at high temperatures and pressures. The crystal structure can have a significant effect on the electronic properties of the material. For example crystalline and polycrystalline indium oxide is not known to superconduct at any accessible temperature, although metal-insulator transitions have been observed in gated polycrystalline films [18]. On the other hand, amorphous indium oxide has been observed to be insulating, metallic, or superconducting at low temperatures depending on the carrier concentration and disorder present.

2.3 Doping and Disorder

Amorphous indium oxide is a disordered material, as can be clearly seen in figure 2.1. This disorder occurs on the atomic length scale. One source of disorder is based on randomness in the interatomic spacing, as would be expected in an amorphous material. This can be tuned to some degree through deposition temperature and post deposition annealing. Another significant source is stoichiometric disorder.

Ovadyahu showed that amorphous indium oxide films typically has between 5% and 30% oxygen vacancies [20]. This can be tuned by the oxygen partial pressure present during deposition. The presence of these vacancies results in a random distribution of In atoms with a valence of +1 instead of +3 in order to preserve neutrality, resulting in stoichiometric disorder [21]. Oxygen vacancies are also responsible for the ability to tune the carrier concentration. In theory, each oxygen vacancy would contribute two

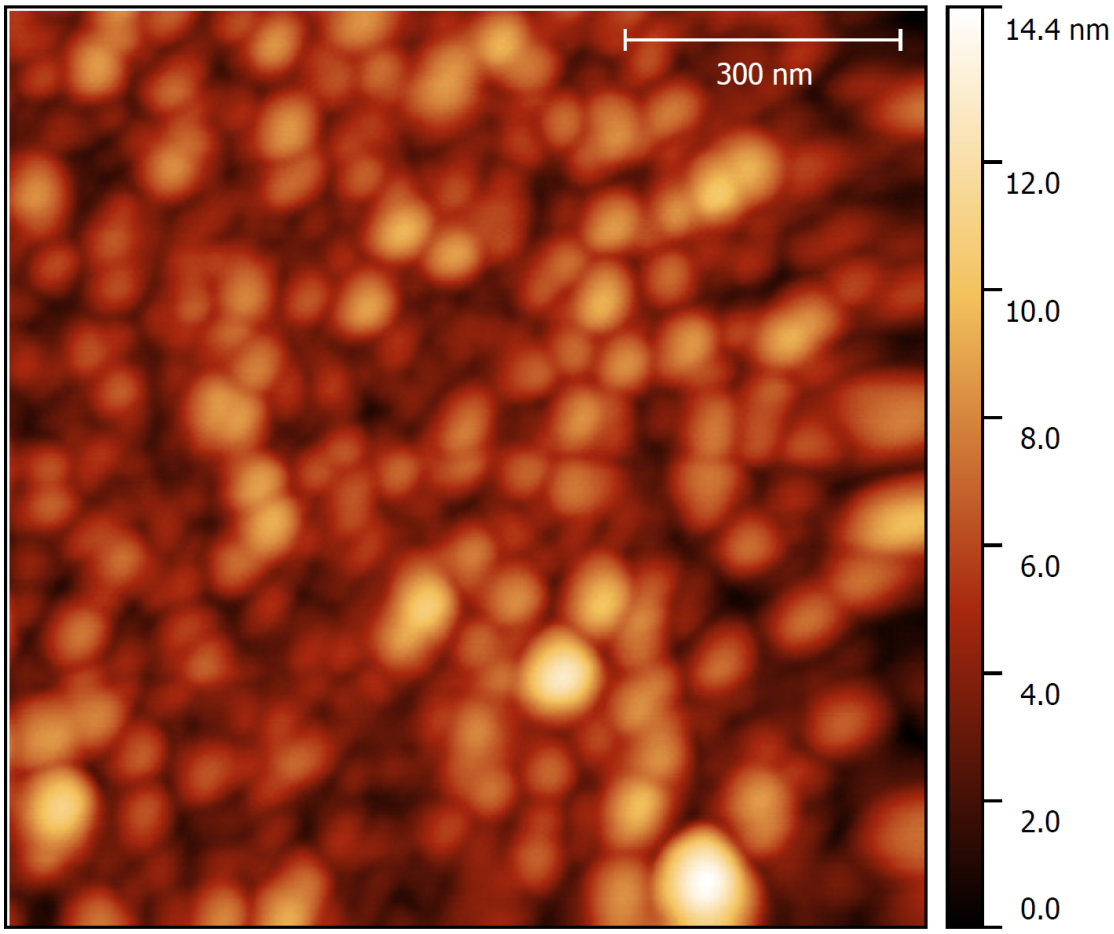

Figure 2.1: Atomic force microscope image of a portion of a 55nm thick amorphous indium oxide film. This film was grown in a similar manner to those studied in detail in Chapters 4 and 5 [19].

additional free electrons. In experiments by Bellingham et. al., it has been shown that the doping efficiency is $\sim 10\%$ [22]. The carrier concentration can also be tuned by electrostatic gating. This was done by Yeonbae et. al. with the aid of ionic liquid. This can change the carrier concentration enough to tune between superconducting and insulating behavior [23].

Another consideration is electronic granularity. This has been theoretically predicted and measured experimentally using scanning tunneling spectroscopy on other materials that undergo SITs [24, 25, 26]. Disorder on the atomic length scale can cause granularity on much larger, mesoscopic length scales. This granularity is in the form of variations in the order parameter, which results in the formation superconducting blobs in an insulating background. This happens even though the films are homogeneously disordered. Josephson coupling between these blobs allows for global superconductivity of the film. The consequences of this will be discussed in detail in Chapter 5.

2.4 Photolithography and Sample Fabrication

In this section the fabrication process for the samples discussed in Chapter 5 will be described in detail. The samples discussed in Chapter 4 were fabricated by another researcher and originally intended for a different experiment. Since these samples were previously made and repurposed for my experiment, I cannot comment on the exact details of their fabrication, however they were produced in a similar manner to what I will describe going forward.

The samples used silicon wafers as a substrate. These 4 inch diameter wafers were sourced from MTI Corporation. The wafers came with a 300nm oxide layer on 0.525mm Si (100) that was P-type and boron doped. The nominal resistivity was 1-20Ωcm. The silicon oxide layer was vital to prevent any electrical shorting of insulating films through the substrate. A silicon substrate was chosen because of the extensive information and

equipment available for silicon processing.

The first step was to cut the wafer down to a more reasonable size. The wafer was cleaned with a standard solvent rinse in acetone, methanol, isopropanol and then a layer of AZ 1512, commercially available photoresist, was spin coated for one minute at 3000rpm. This layer of photoresist was necessary to protect the oxide layer on the wafer from damage during cutting with the wafer saw. The wafer was cut down to pieces approximately 30 x 20mm to allow enough space to pattern four samples.

The first layer to be deposited on the substrate was the Ti/Au contact layer. This layer was patterned using photolithography. The first step was to clean the substrate with an acetone, methanol, isopropanol solvent rinse, in that order. Next was a three minute pre-bake at 150℃ to ensure the wafer was completely dry. This was followed by spin coating LOR3A positive photoresist for 45 seconds at 3000rpm. The substrate was then baked for two minutes at 170℃. AZ1512 was spin coated for 30 seconds at 4000rpm. Next was another bake at 100℃.

The next step was to expose the photoresist. The pattern was created using Auto-CAD software, shown in figure 5.2, outlined in darker lines. This CAD file was then used by the MNC staff to make a mask using the Heidelberg DWL200 laserwriter. This mask was loaded into a Karl Suss MA6 contact aligner to align the mask over the photoresist coated wafer and expose it for five seconds to UV light with an intensity of 12mW/cm^2.

After exposure was development. There was a one minute post bake at 95℃ followed by a 30 second rinse with CD-26 developer. The substrate was rinsed with deionized water for two minutes. Next, was a two minute bake at 120℃ followed by another 25 second rinse with CD-26 and two minute rinse with deionized water. Lastly, the substrate was cleaned using an oxygen plasma etcher to remove any residual photoresist in the patterned area. This was done with the power set to 100W and an oxygen flow rate of 225 sccm.

Two different photoresists, AZ1512 and LOR3A, were used for the contact layer pattern in order to prevent fencing. The double layer of photoresist, with the LOR3A under layer having a faster development time, allowed for an undercut to be made. This undercut prevented fencing at the edge of the Ti/Au layer which improved the contact between this layer and the subsequently deposited indium oxide layer.

The Ti/Au contact layer was deposited using the CHA electron beam evaporator in the Minnesota Nano Center cleanroom. Titanium was deposited first to help with adhesion of the gold layer to the substrate. This layer was 1.4nm thick and deposited at a rate of 0.002nm/s. The gold layer was 12.0nm thick and deposited at a rate of 0.01nm/s. During the deposition, the pressure in the chamber was on the order of 10^{-6} torr. Liftoff for the contact layer was done in NMP heated to 80℃ on a hotplate. This was followed by a standard solvent rinse.

Next, the patterning for the indium oxide layer was done, shown in lighter lines in figure 5.2. This used a single layer technique since fencing was not a concern. The first step was a three minute pre-bake at 150℃, followed by a 20 second spin coating with HMDS at 4000rpm. Then, AZ1512 was spin coated for 30 seconds at 4000rpm. Next, was a one minute soft-bake at 100℃. The photoresist was exposed for five seconds using the same MA6 contact aligner followed by a one minute post bake at 95℃. Lastly, there was a 30 rinse with CD-26 developer followed by a two minute rinse with deionized water. After inspection, the patterned substrates where then shipped to our collaborators at Bar Ilan University in Israel for deposition of the indium oxide layer.

The indium oxide layer was grown by electron beam evaporation and was 30nm thick. In_2O_3 was evaporated in a vacuum chamber that had oxygen bled in through a needle value while continuing to pump on the chamber. The partial pressure of oxygen was held between $2 * 10^{-5}$ and $9 * 10^{-4}$ mbar. The substrate was kept below 40℃ during deposition to ensure that the resulting film was amorphous. The exact partial pressure

of oxygen in the chamber was varied between depositions on multiple substrates to tune the disorder and carrier concentration of the resulting indium oxide film and thus the critical field of the superconductor-insulator transition.

Upon return of the substrates with the indium oxide film deposited, another liftoff procedure was carried out. The substrates were sonicated in acetone for 1 minute and then underwent a standard solvent rinse. After liftoff the substrates were spin coated in AZ1512 for one minute at 3000rpm. This was done to protect the devices from damage, due to wafer debris and cooling water, while cutting in the wafer saw. Each substrate was cut into four samples. Since each co-deposited sample was in close proximity to each other during deposition it was assumed that they would be uniform and have similar low-temperature resistivity characteristics and would respond similarly to annealing.

2.5 Annealing of Indium Oxide

As was discussed in detail earlier, the interplay between the carrier concentration and the quenched disorder determine, to a significant degree, the properties of the film. While the carrier concentration is largely fixed during deposition, the disorder is not. Annealing can drive a highly disordered film from an insulating state to a less disordered and more metallic state. In some cases annealing can reduce the disorder enough that a film that is insulating in zero applied magnetic field can become superconducting.

The effects of annealing indium oxide were studied extensively by Ovadyahu [27]. It was found that the resistivity of the films could be changed through heat treatment. For amorphous films, heating to temperatures between 40℃ and 60℃ and maintaining this for a period of a couple hours to weeks would reduce the resistivity. The room temperature resistivity could be reduced by up to three orders of magnitude. This change was irreversible. Annealing under vacuum or in atmosphere had negligible effect on how much the resistivity changed. Amorphous samples that were kept below 100℃

during the heat treatment exhibited no signs of crystallization. Samples heated above this temperature did exhibit at least partial crystallization.

Crystalline indium oxide samples also responded to heat treatment. The resistivity of these films could be increased. This was done by heating the samples to between 200℃ and 400℃ and allowing them to cool back down to room temperature. The resistivity could be increased by two orders of magnitude and was dependent on the cooling rate as well as the initial temperature. The faster the cooling rate, the larger the increase in the resistivity. This process was reversible, unlike for the amorphous films.

Annealing was a vital tool for preparing the amorphous indium oxide films that were studied in this dissertation. Annealing not only reduced the room temperature resistivity, but had a dramatic effect on the low temperature behavior. For example, sample InOx_072417 was annealed under vacuum for a total of 60 hours and temperatures from 40℃ to 60℃. The first 42 hours of annealing were at 40℃, the next 12 hours at 50℃, and the last 6 hours were at 60℃. After the first six hours, the sample was cooled down to ∼400mK after every three hours of annealing and the resistance versus temperature was measured, shown in figure 2.2. The resistance at base temperature dropped by three orders of magnitude. The change in resistance as a function of annealing time at a fixed temperature decreases dramatically as time goes on. Finally, the reduction of resistance appears to saturate by 60 hours of annealing, for this sample. In practice reducing the room temperature resistance to ∼2kΩ/□ was the threshold for superconducting instead of metallic or insulating behavior when cooled to low temperature.

The metallic behavior exhibited by the samples studied in Chapter 4 is believed to be the result of undergoing this annealing process to some degree. The films were never heated and the annealing process should be exponentially slower at room temperature than at 40℃-60℃, but they were measured 3 years after deposition. This was likely a sufficient amount of time for some non-negligible annealing to occur even at room

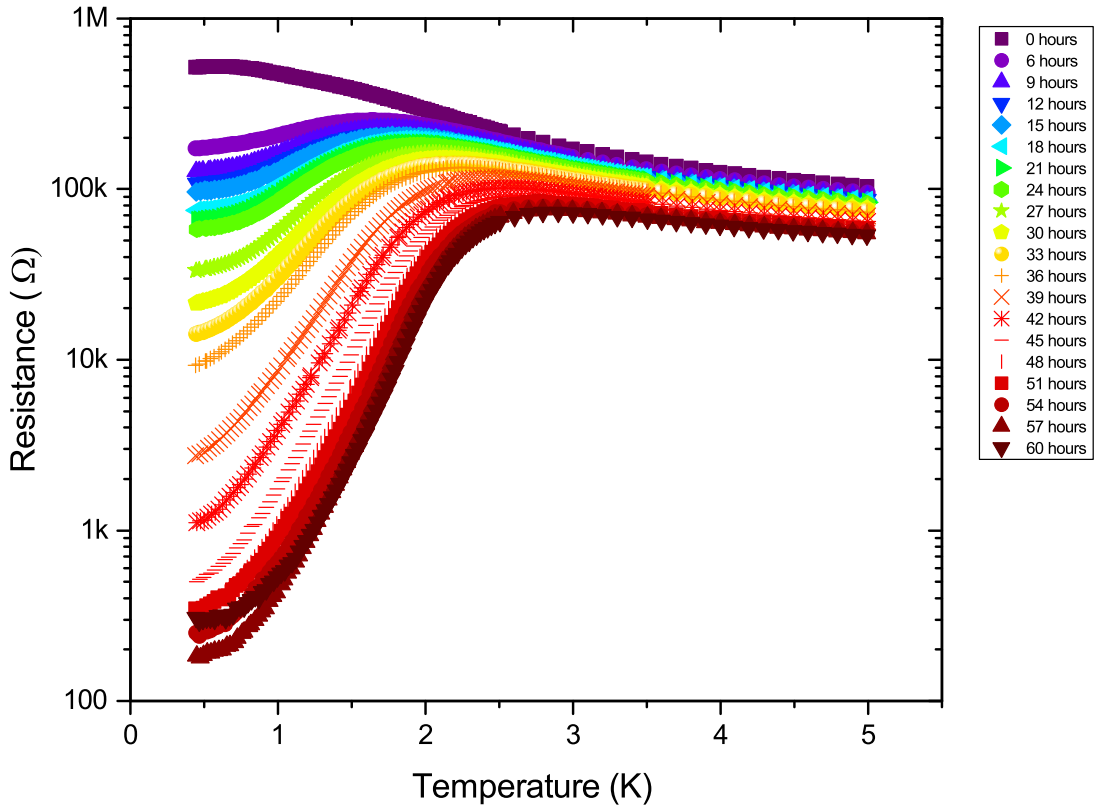

Figure 2.2: Resistance versus temperature plot for InOx_072417 with zero applied magnetic field. The legend refers to the number of hours of annealing the sample had underwent in total. The first 42 hours were at 40℃, the next 12 at 50℃, and last 6 at 60℃. The measurements were done in a Quantum Design PPMS, as was most of the annealing.

temperature. The films studied in Chapter 5 were annealed in a much more deliberate manner.

As deposited, the films studied in Chapter 5 were insulating. Looking at the resistance versus temperature plot for one of the co-deposited films, shown in figure 2.3, it is exhibiting insulating behavior in zero applied magnetic field. There is a magnetoresistance peak somewhere between 0T and 6T applied perpendicular magnetic field. This behavior is clearly not useful for studying the properties of the superconductor-insulator transition. Annealing was vital to preparing these samples. After four hours of annealing, the sample was superconducting in zero applied field with a critical field between 0T and 3T and a magnetoresistance peak between 6T and 9T, shown in figure 5.3.

This sample was subsequently annealed for another two hours at 60℃. This last step pushed the critical field up to between 3T and 9T. It also raised the magnetoresistance peak to greater than 6T. This was decided to be too high of critical field to be useful for further study, but was informative as to how to heat treat the other co-deposited samples.

2.6 Effective Dimensionality of Films

The effective dimensionality of a film depends on how thick it is in comparison to the relevant length scales of the system. For a superconducting system one relevant length scale is the penetration depth. As was discussed in the introduction, a magnetic field can only penetrate superconducting material over short distances, with the exception of vortices in type 2 superconductors, and the field decays exponentially with a characteristic length scale, λ. The London penetration depth can be estimated using the following equation [1],

$$\lambda_L(T=0) = \sqrt{(mc^2)/(4ne^2)} \tag{2.1}$$

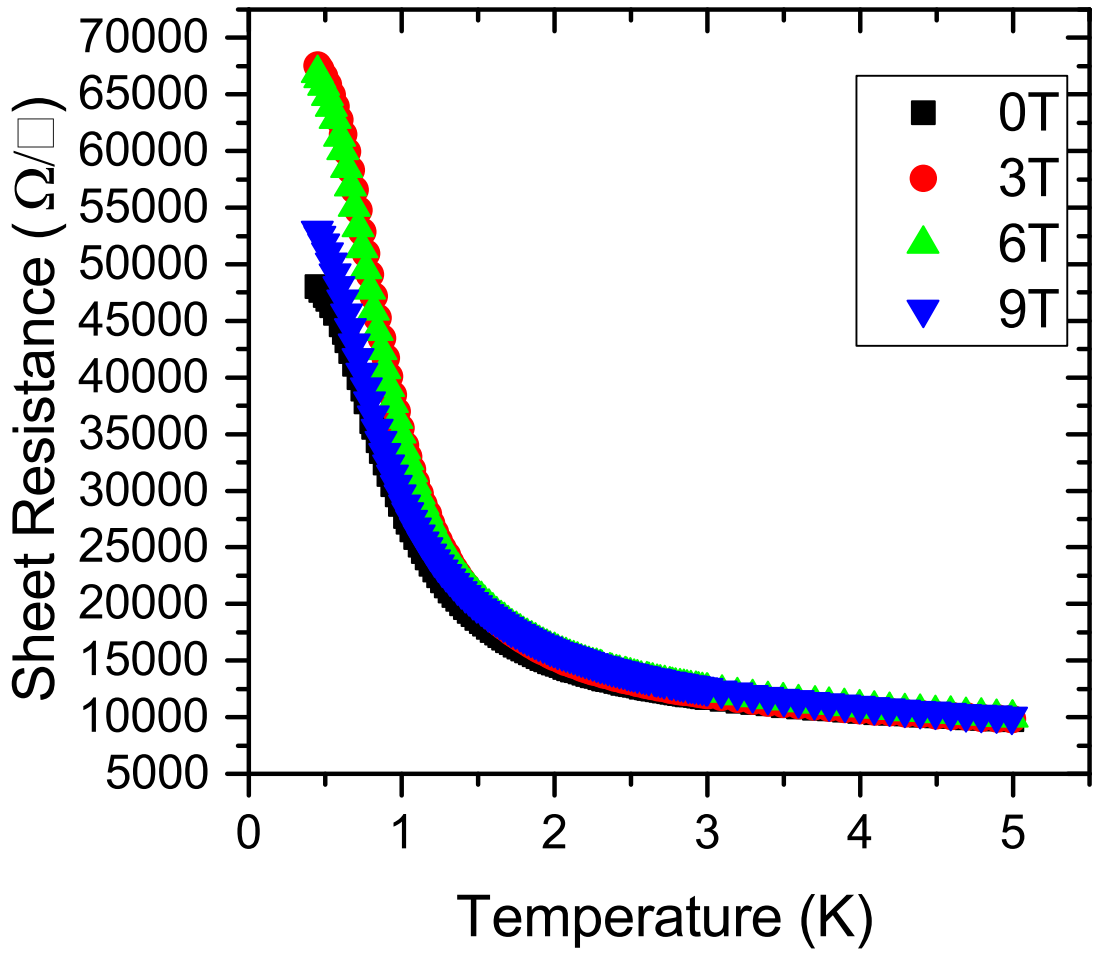

Figure 2.3: Plot of the sheet resistance of sample InOx_061520_1 as deposited, under various applied perpendicular magnetic fields. This film clearly does not exhibit an SIT.

where n is the superconducting carrier concentration. The carrier concentration of the normal state material would be an upper bound for the superconducting carrier concentration and thus allow an estimate of the lower bound of the penetration depth.

However, for thin films in a perpendicular magnetic field, the Pearl length takes the role of the penetration depth. This length corresponds to the characteristic length for the interaction energy between vortices in the film and is expected to be, $\lambda_\perp = \lambda_L^2/\mathrm{d}$, where d is the film thickness [28]. This has been shown to be on the order of several millimeters for typical superconducting systems [29]. This is much thicker than the 30nm films discussed throughout this dissertation, thus they are expected to behave as two-dimensional systems.

Another relevant length scale in the coherence length. This is relevant on both sides of any quantum phase transition when near the transition, not just on the superconducting side. Looking at equation 1.2 in the introduction and recalling that the coherence length scales as $\xi \propto |\delta|\nu$,it is clear that the coherence length diverges as the transition is approached. The thickness of the film is less than both the penetration depth and coherence length in the vicinity of any quantum phase transition and therefore it is expected to behave as a two dimensional system and belong to corresponding two dimensional universality classes.

2.7 Conclusions

Indium oxide has been studied extensively by many different research groups. In its amorphous form it exhibits one of the most commonly studied examples of a quantum phase transitions. One reason for the significant interest in studying this material is the broad range of behavior it can exhibit and the ability to tune this behavior. Indium oxide can exhibit superconducting, metallic, or insulating behavior which can be tuned by disorder or carrier concentration. This tuning can be done through tuning the growth

conditions, annealing, or electrostatic gating.

Chapter 3

Experimental Techniques and Limitations

3.1 Introduction

Carefully considered measurement techniques are vital to any successful experiment. These considerations include understanding the conditions that any sample of interest is exposed to, such as magnetic fields, electric fields, temperature, pressure, etc. Some seemingly simple things, such as the temperature of the sample, can be less than straightforward to determine at sub-Kelvin temperatures. This will be discussed extensively in this chapter. Additionally, reducing any unwanted noise in a measurement is important to accurately measuring any signal of interest.

3.2 Temperature Control

The determination and precise control of the sample temperature was of critical importance during the measurements described in the following two chapters. Sub-Kelvin

thermometry is not nearly as straightforward as thermometry in the vicinity of room temperature. A number of issues can arise. In this section I will explain in detail the temperature measurement and control techniques employed in both the Oxford Kelvinox 25 and Kelvinox 400 dilution refrigerators. I will not go over the details for the Quantum Design PPMS since this system was mainly used for rough characterization and pre-screening of samples.

Both dilution refrigerators made use of ruthenium oxide resistance thermometers. This material is a common choice for sub-Kelvin temperature measurement because of its combination of high sensitivity of the resistance to temperature at this temperature range, stability of temperature dependence over time and thermal cycles, and low sensitivity to magnetic fields. These sensors are commercially available from a number of suppliers and can come pre-calibrated. Both the K25 and K400 had 2000Ω RuO thermometers attached to their mixing chambers, which are in good thermal contact with the samples. The K25 also had an additional RuO thermometer installed on the sample holder itself, within 1cm of the sample.

In both cases the resistance was measured using a Picowatt AVS-47 resistance bridge. This device sources a low-frequency (15 Hz) AC current across the sensor. The voltage across the sensor is then measured to determine the resistance of the sensor. This resistance measurement is then compared to the calibration data to determine the temperature. The sensor is wired using a standard four terminal arrangement with independent voltage and current leads to eliminate lead resistance from the measurement. Additionally, the leads are made of wires with low thermal conductivity that are also heat sunk at various cooling stages of the dilution refrigerator to limit external heat leaks to the sensor. Lastly, only a small current is sourced to the sensor, 30nA above 120mK and 3nA below, to limit Joule heating of the sensor.

The temperature was controlled using a Picowatt TS-530 temperature controller.

This device used PID controls along with feedback from the mixing chamber thermometer to control a heater mounted to the mixing chamber. For the K25, the temperature was swept from base temperature to the maximum stable temperature of 1.7K using only the mixing chamber heater. The cooling power of the refrigerator was not directly controlled in any way. For the K400, the cooling power was only controlled by turning off an additional circulation pump when stabilizing at temperatures above 300mK. The rest of the temperature control was achieved with the heater. In both cases the power dissipated to achieve the desired temperature was on the order of 1μW to 1mW, depending on the temperature. Typically, a measured stability of better than 0.25mK could be achieved, with better stability at lower temperatures due to the increased sensitivity of the ruthenium oxide sensors.

3.3 Sample Temperature

All of the active temperature control was done referencing thermometers mounted on the respective mixing chambers. An additional concern was how reliably the temperature at the mixing chamber corresponded to the actual sample temperature. One way this difference was minimized was by having the sample substrate in good thermal contact with the mixing chamber.

For the K25, the sample was mounted to a copper sample holder using GE varnish, VGE-7031. GE varnish is commonly used for thermal anchoring in cryogenic systems because of its good thermal conductivity, low outgassing, and it is electrically insulating. For the K400, the sample was mounted to a copper sample holder using Apiezon N grease. Like GE varnish, this material improves thermal contact, has low outgassing and was used, instead of varnish, to ensure the sample could be removed from the holder without damage. Both sample holders screw onto a copper rod connected to the respective mixing chamber. Additional thermal contact directly to the indium oxide film

was provided by the wire leads that provided electrical contact to the sample. These leads are thermally anchored to the mixing chamber.

Another concern is any potential temperature difference between the lattice of the indium oxide film and the conduction electrons. It has been theorized that it is possible for the electrons in a system to interact weakly with the phonons but strongly with each other. This can lead to the electrons being overheated relative to the lattice temperature [30, 31]. Evidence for this electronic overheating has been observed in amorphous indium oxide by Levison et. al. [32]. This electronic overheating would be impossible to detect with either the mixing chamber mounted thermometer or in the case of the K25, even the sample holder mounted thermometer.

With the possibility of electronic overheating in mind, the IV characteristics at base temperature for each measured film were studied. Provided the true R(T) was not constant, any heating would result in a deviation from linear, Ohmic behavior. This heating can be clearly seen in figure 3.1. This figure shows the IV characteristics for sample InOx_061520_2 measured in the K400 dilution refrigerator. This was done at a temperature of 50mK with an applied perpendicular field of 6T. In this temperature regime, with this applied field, the fixed current R(T) measurements, shown in figure 5.5, indicate that the resistance is decreasing with increased temperature. As can be seen in figure 3.1, the slope is decreasing as the applied current increases in magnitude, corresponding to increased Joule heating. This change in slope is entirely consistent with heating and can be observed independent of thermometer readings.

In any low temperature transport measurement there is an inherent tradeoff between Joule heating and signal-to-noise ratio. Larger measurements currents improve the signal-to-noise ratio at the expense of more heating. Smaller currents have the opposite effect. The measurement currents for all the transport measurements described in this dissertation were chosen to be as large as possible while still causing minimal heating

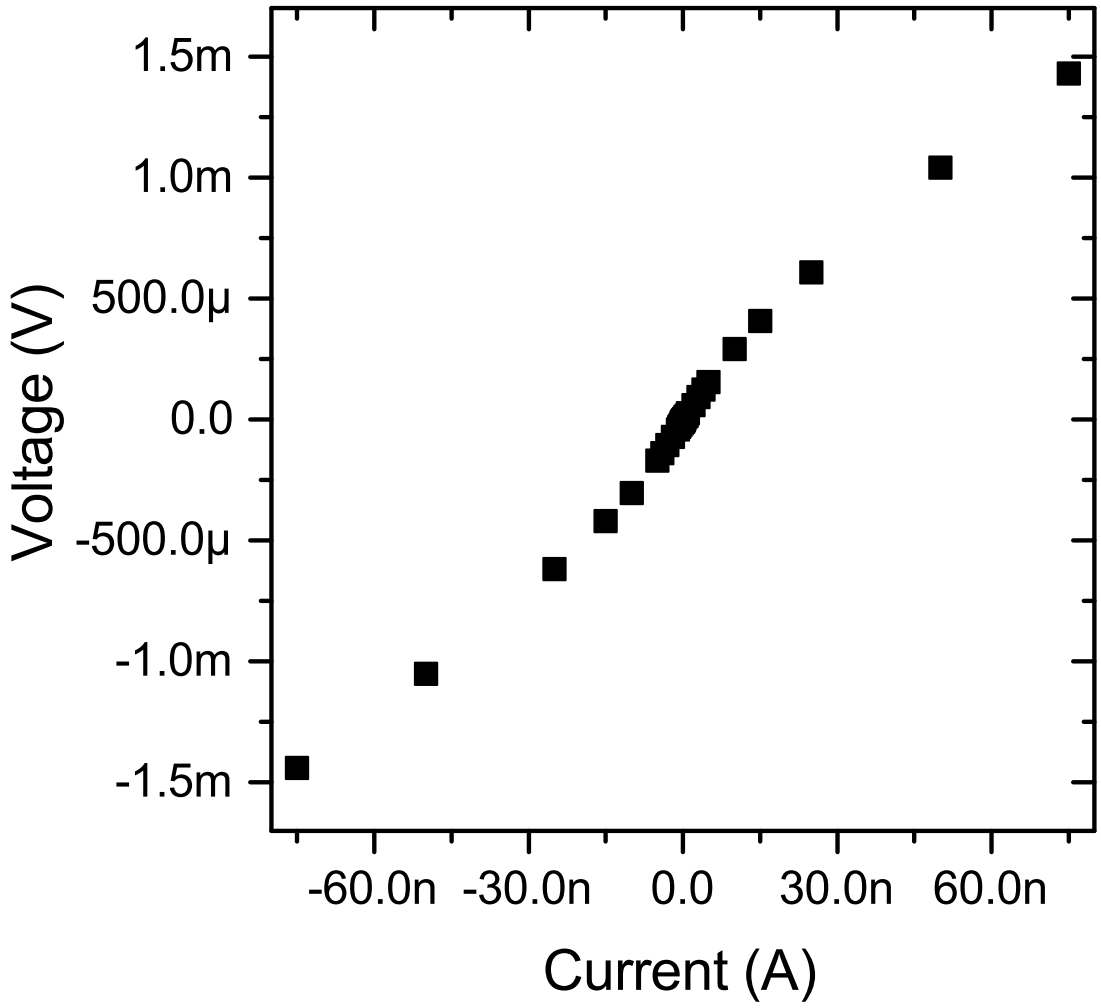

Figure 3.1: Plot of the voltage versus applied current for sample InOx_061520_2 at 50mK with a 6T perpendicular field applied. The non-linear behavior indicates heating.

over a reasonable temperature range to optimize the accuracy. The optimal current was determined by looking at the extent of the linear regime of the base temperature IV measurements.

Regardless of the cause, failure to cool will be evident as a flattening of the R(T) curves at low temperatures. This is evident when looking at figure 5.5. All the curves appear to flatten at temperatures below 100mK. This is most apparent in the curves around 6T, where the sample resistance is the highest and the slope is the steepest just above 100mK. There is no reason to believe that the sample resistance should suddenly become temperature independent below 100mK. This strongly suggests a disconnect between the mixing chamber thermometer reading and the sample temperature. Since this flattening occurs even when the sample resistance is much lower and Joule heating should be significantly lower, combined with the linear IV characteristics in the vicinity of the measurement current, it was determined that this failure to cool was not caused by the measurement current. External noise can be another source of heating.

3.4 Grounding/Circuit Isolation

Much thought was put into the grounding of the equipment used and the isolation of the measurement circuits, whether setup for measuring resistance fluctuation or the resistance itself. This was done to reduce external noise present in any measurement and to reduce heating of the samples. Both the K25 and K400 were grounded at a single point using heavy gauge cable. The ground was provided by a dedicated instrument ground for the building. This ground is separate from the standard building ground and meant to limit interference from noisy equipment in the building, such as large electric motors and power supplies.

The purpose of single point grounding was to eliminate ground loops. Any ground loops present could result in current flowing through the ground and a voltage difference

between different ground points. This causes unwanted noise and reduces the accuracy of any measurement referencing ground. Ground currents can be induced by stray AC magnetic fields, such as those produced by the transformers present in the power supplies of most electrical equipment. Ground loops were systematically eliminated with careful circuit arrangement and testing.

Unwanted connections to ground were eliminated in a variety of ways. First of all, the measurement electronics were not plugged directly into the building power supply. Instead, they got their power through an isolation transformer. This prevented any connection through their power cords to the standard building ground, instead they were grounded with a grounding strap to the dilution refrigerator and then to instrument ground. Additionally, the electronics were mounted to the electronics rack using screws with plastic grommets to prevent electrical contact with the rack.

The BNC and triaxial cabling between the various measurement electronics was another concern. These cables have a shielding layer that is meant to be grounded. Isolation boxes were fabricated to mount to the various cable bulkheads in strategic places to ensure all the shielded cables were grounded, but did not form any loops. This also determined the location of the ground reference in the measurement circuit.

The bellows used in gas handling for the dilution refrigerators was another potential avenue for an unwanted path to ground. The bellows leading to the circulation pumps and gas handling control box all had at least one section of PVC tubing, or a connection using a plastic centering ring and clamp for the KF connection, to isolate the dilution refrigerator from the ground for the control box and pumps. The K400 had an MBE system attached to the bottom for in-situ sample growth capability. This adds more equipment that needs to be isolated. The turbo pump for the inner vacuum chamber was electrically isolated from the refrigerator using a ConFlat connector with

a ceramic insulating segment. The ion pump was isolated using a similar ceramic coupler and rubber grommets where the support rods connected to the scaffolding for the refrigerator.

Since the temperature controllers, magnet power supplies, and final readout of the measured data needed to be handled by a computer, this was another potential unwanted path to ground. The communication cables, GPIB and USB, between the computer and various pieces of equipment had grounded shield layers. To isolate the computer ground from any measurement electronics, special isolator boxes were used. The equipment using GPIB for communication with the computer had the signals routed through a National Instruments GPIB-120A Bus Expander/Isolator to isolate from the computer ground. The equipment that used USB for communication made use of a BB Electronics Rugged USB Isolator.

Testing was done to identify the presence of any additional ground loops. This was done using a commercially available product called a Loop Slooth. This device used an exciter and detector module to test for ground loops without disconnecting or interrupting the circuit in question in any way. This was done by inductively coupling to the cable with the exciter module that would drive a 100kHz AC signal in any loop, and using the detector module to detect the current if there was a loop. The device also indicated a quantitative measure of the induced current.

This device was useful to verify that all ground loops were removed and was also sensitive to capacitive coupling to ground. Several sources of capacitive coupling were removed or reduced. For the K25, there was no measureable capacitive coupling to ground. For the K400, it was not possible to remove all coupling to ground. The source of at least one relatively weak capacitive path to ground was never identified or removed. This may have been caused by something as obscure as capacitive coupling between the aluminum scaffolding supporting the K400 and the rebar in the reinforced concreate it is

bolted to. It also could have been across a KF connection that used a plastic clamp and centering ring. Regardless, this coupling is expected to have had minimal impact on the measurements conducted because no signals were sourced or measured at frequencies greater than 1kHz. The coupling was already weak at 100kHz and would be far weaker at frequencies two orders of magnitude lower.

3.5 Filtering and Noise Induced Heating

In addition to the measurement current, external noise can be a significant source of heating. External noise was reduced significantly by avoiding ground loops in the measurement circuit and by electrically isolating it from noisy electrical equipment such as electric motors. Unfortunately, this is not sufficient to eliminate all external noise. Electromagnetic noise, such as RF noise, significantly limits the lowest temperatures at which accurate transport measurements can be made.

It has been theorized that superconducting thin films are extremely sensitive to external noise. Experimental evidence of this was found by Tamir et. al. [33]. They studied the effect of electronic filtering on the properties of thin films, including amorphous indium oxide. It was found that with improved low-pass filtering of the signal lines to the sample, the saturation of the measured resistance at low temperatures could be reduced or in some cases completely eliminated. The saturation that was filtering dependent was very similar to the measurement current induced saturation that is observed when excessively large measurement currents are used. Based on this, they concluded that external radiation causes significant heating that affects the accuracy of low temperature resistance measurements.

Similar effects were observed when measuring the indium oxide thin films discussed in the following chapters. Both the K25 and K400 dilution refrigerators employed low-pass Pi filters to limit heating due to external radiation. The effects of this filtering were

tested, as shown in figure 3.2. Adding Pi filters to the measurement leads had a greater effect than lowering the measurement current from 20nA to 2nA. As can be seen, when there was more filtering the measured resistance was lower and the flattening of the R(T) curves did not start until lower temperatures were reached. This clearly demonstrates that reducing the measurement current and ensuring linear IV characteristics is not sufficient to minimize heating effects.

The filters for both systems were low-pass Pi filters. These filters had a cutoff frequency of 100kHz and were mounted in a breakout box near the top of the cryostat. Inside the breakout box the feedthrough Pi filters were mounted to a copper plate that was grounded and positioned such that it covered the entire cross-section of the box between the input and output sides. This provided additional shielding and limited RF coupling between the two sides of the filters.

3.6 Conclusions

Many precautions were taken to ensure the accuracy of the low temperature measurements that were made. The temperature of the sample was carefully controlled using thermometers and temperature controllers that are commercially available and commonly used in sub-Kelvin measurement apparatus. Testing with each sample was done to ensure that the temperature measured by the thermometry was an accurate representation of the actual temperature of the sample. This was done by studying the IV characteristics and comparing the sample resistance at the lowest temperatures to the expected trend. Additionally, extensive testing was done to reduce the background noise level of the measurement system, which was also shown to reduce heating. All these factors combined to achieve a minimum temperature at which the sample could be measured of $\sim$100mK.

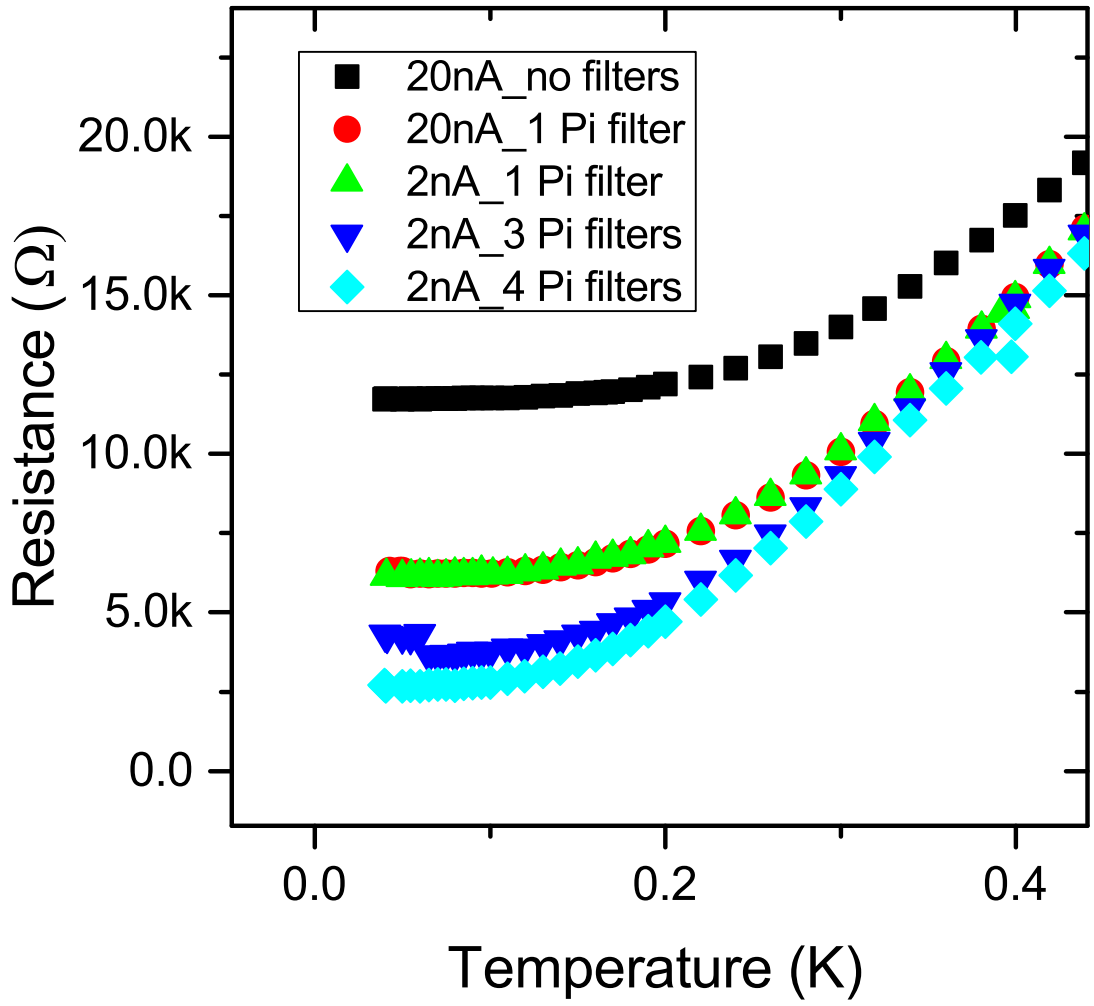

Figure 3.2: Plot of the resistance versus temperature for sample InOx_111017_2 as measured in the K400 with various measurement currents and degrees of electrical lead filtering. These curves were measured with a 3T perpendicular magnetic field applied. This indium oxide sample underwent a superconductor-insulator transition with a critical field of ∼6T. This shows that adding additional filtering seemed to reduce the resistance and temperature at which flattening occurred. The use of current below 20nA had negligible effect as shown by the red circles and green upright triangles.

Chapter 4

Indium Oxide Films Exhibiting An Infinite Randomness Fixed Point

4.1 Introduction

The Griffiths effect is a group of unconventional behaviors, such as a singularity in the free energy and various observables, in the vicinity of a phase transition that are the result of rare, ordered regions [34]. These rare regions are caused by the interplay between quenched disorder and the phase transition in a material. When this quenched disorder is sufficient so as to cause rare ordered regions when near the critical point it causes slow dynamics and such a system will exhibit the Griffiths effect. If the phase transition is a quantum phase transition, the Griffiths effect is referred to as the quantum Griffiths effect. Under the right circumstances, which I will describe in more detail later, such a system can also have an infinite-randomness fixed point. The Griffiths effect was originally predicted over 40 years ago, but has recently gained

renewed experimental interest. It has been observed in some magnetic systems, but only recently in superconducting systems, specifically those undergoing a superconductor-metal quantum phase transition.

The reports of the observation of this effect in several superconducting materials led us to investigate whether this effect could explain unusual superconductor-metal transitions observed in some indium oxide samples. These samples were not able to be analyzed using the usual power-law, finite-size scaling technique described earlier because there was not a single value of the magnetic field at which magnetoresistance isotherms crossed, a feature of the data on which the analysis depends. Gantmakher et. al. [35] reported observing similar behavior in amorphous indium oxide films, but did not explain why it occurred. For these films there appeared to be a continuum of crossover field values. These fields were given by the crossing points of magnetoresistance isotherms.

This is qualitatively similar to what others had observed in systems reported to exhibit the quantum Griffiths effect. Upon further analysis, a result similar to what others had was found. This result was a divergent product of the correlation length and the dynamical critical exponents in the limit of zero temperature, when power-law scaling was applied at selected crossing points. However, considered this analysis was not strong enough evidence to make the claim of having found a quantum Griffiths effect, because there was no justification for the procedure used to analyze the data. Furthermore, activated scaling rather than power law scaling is expected to describe the critical behavior of the quantum Griffiths effect.

We were able to use additional analyses for what would be expected near the critical points of systems exhibiting the quantum Griffiths effect. These will be described later in this chapter, to provide further evidence that this effect was observed. In particular, with these results as a stepping-stone, we were able to perform an activated scaling analysis

of the data. This provided very strong evidence for the quantum Griffiths effect with an infinite randomness fixed point. This type of scaling has been predicted to describe systems exhibiting the quantum Griffiths effect, however, there are no examples in the literature of it being applied to a superconductor-metal quantum phase transition other than our work.

4.2 History

The Griffiths effect was first described in 1969 by Robert Griffiths in a paper studying a special case of the paramagnetic/ferromagnetic phase transition [36]. Griffiths studied the Ising model for the case of a random ferromagnet. In this scenario only a portion of the sites on the lattice are occupied by an Ising spin. He showed that for a finite temperature range below T_c of the bulk system, the magnetization is non-analytic and that there is a singularity in the free energy. This temperature range is now called the Griffith phase. Since this paper was published there has been considerable theoretical and experimental work done regarding this effect.

4.3 The Physics of the Griffiths Effect

Quenched disorder can have a significant effect on phase transitions, especially, quantum phase transitions. As an example of the Griffiths effect it is simplest to consider the case of a diluted Ising ferromagnet as was originally done by Griffiths himself. In this scenario, many lattice sites in the system do not have an Ising spin and the critical temperature, T_c, between the ferromagnetic and paramagnetic states of the system is reduced from the undiluted critical temperature, T_{c0}. Within the temperature range between T_c and T_{c0} the system as a whole is in the paramagnetic state, however, some individual clusters of spins within the system can behave like the bulk undiluted system.

Some of these clusters will locally be in a ferromagnetic state since the temperature is below the T_{c0}. These so called rare regions that are locally ordered within an overall disordered system can completely smear out the phase transition of the complete system in some cases, and have a negligible effect in other cases, depending on the nature of the disorder.

Whether disorder leads to rare regions and its effect the transition depends on how the disorder behaves under coarse graining. This involves looking at how the average disorder strength changes as longer length scales are considered. This can be predicted based on the Harris criterion. Taking into account how the spread in values for individual T_c^* for each rare region is related to the correlation length and how the correlation length varies as the system nears the transition, Harris was able to show that $d\nu > 2$ was the cutoff between the different behaviors [34]. In this expression, d is the dimension of the rare region and ν is the correlation length exponent. Systems that violate this Harris criterion are not stable in the presence of disorder and form rare, ordered regions. Systems that meet this criterion may or may not be stable, as it is a necessary, but not a sufficient condition for stability [37]. Systems that meet the Harris criterion and are stable against quenched disorder have an average disorder strength that decreases under coarse graining. Systems that violate the criterion are unstable and can have either finite or infinite disorder strength under coarse graining. For the case of finite disorder, the system follows power-law scaling. For infinite disorder, the system can follow activated scaling or be smeared and not follow any type of scaling.

Getting back to the earlier example of the ferromagnetic/paramagnetic transition, which does violate the Harris criterion, we consider how the rare regions effect the transition. The effect of rare regions on the transition depends on the interplay of the probability of a rare region occurring within a given volume with the strength of its effect on the properties of the system. This is determined by both the effective dimensionality

of the rare regions and the lower critical dimension of the phase transition. If the dimensionality of the rare regions is less than the lower critical dimension, the rare regions cannot undergo individual phase transitions independent of the system as a whole and have a limited effect on the transition. This type of system is expected to still follow power-law scaling.

If the dimensionality of the rare regions is greater than the lower critical dimension, the rare regions can undergo individual transitions independently of the system as a whole. In this case the dynamics of the rare regions are static and the transition becomes smeared and doesn't exhibit scaling behavior. For the special case of the dimensionality of the rare regions being equal to the lower critical dimension, the rare regions don't undergo the transition with the bulk system, but are not completely independent either. The dynamics of the rare regions are slow, but they are not static. This results in the system following activated scaling and exhibiting an infinite randomness fixed point as opposed to power-law scaling or a smeared transition.

Even though the systems that we studied are clearly not magnetic systems there are still important comparisons that can be made between these magnetic systems and superconducting systems. For example instead of thinking about a diluted ferromagnet, we can consider a diluted superconductor, with applied perpendicular magnetic field taking the role of temperature. In a film with quenched disorder, such as indium oxide, different regions of the film can have different local values of superconducting critical magnetic field. Similar to the case of the ferrromagnet/paramagnet transition, there can be applied magnetic fields near, but above the global superconducting critical field where the bulk of the film is metallic, but there are isolated rare regions that are still superconducting.

The analogy between magnetic systems and superconducting systems can be taken a step further by looking at the symmetry of the systems. As described in the introduction,

superconductors can be described using Ginzburg-Landau theory and have an associated spatially dependent order parameter. This order parameter is complex valued and therefore belongs to the O(2) symmetry group. Similarly, the Heisenberg model in two dimensions allows for each individual spin to have a full rotational degree of freedom and thus has O(2) symmetry as well, as opposed to the Ising model which only allows for spin values of ± 1. Since both of these systems belong to the same symmetry group, they are expected to have similar behavior in the presence of quenched disorder when near their respective phase transitions. This has been shown exactly for the case of one dimensional nanowires [37].

The Heisenberg anti-ferromagnetic transition has been studied in detail by Vojta and Schmalian [38]. They showed that in the presence of Ohmic damping the Heisenberg anti-ferromagnet model is at its lower critical dimension and has quantum Griffiths behavior. Without this Ohmic damping the transition is expected to follow conventional power law scaling. Additionally, Hoyos et al. showed using strong-disorder renormalization group theory applied to Landau-Ginzberg-Wilson theory that the quantum phase transition is in the same universality class as the random transverse-field Ising model. This implied that the transition had an infinite randomness critical point and therefore the transition should follow activated scaling [39, 40].

Such a system, with slow dynamics due to the presence of rare regions, has a correlation time which has the form,

$$\xi_T = e^{cont.*\xi^{\psi}} \tag{4.1}$$

where ξ is the correlation length and ψ is the tunneling critical exponent. The name of the tunneling exponent, ψ, comes from the random transverse-field Ising model. This scaling was first found when studying this model. The flipping of spin clusters within this model is proceeded by the tunneling of a domain wall through the cluster. The dynamics of this process are described in part by this exponent [41]. The modified

correlation time leads to the activated scaling form,

$$R(\delta, ln(T_0/T)) = \Psi[\delta * (ln(T_0/T)^{1/(\nu\psi)})] \tag{4.2}$$

where T_0 is a microscopic temperature scale, ν is the correlation length exponent, and δ is the distance from the critical point.

Based on the exponential relation between the length and time scales in this system it has been shown [40] that the dynamical critical exponent is expected to diverge as the critical point is approached and take the modified form,

$$z' \sim |p - p_c|^{-\nu\psi} \tag{4.3}$$

where $|p\text{-}p_c|$ is a generic distance from criticality, where p is the control parameter of the quantum phase transition. The critical temperature for quantum Griffiths behavior takes the form,

$$T_c \sim e^{-const*|p-p_c|^{-\nu\psi}} \tag{4.4}$$

Numerical calculations [42, 43] have shown that in two dimensions, ψ is expected to have a value of approximately 0.5 and the correlation length exponent has a value of approximately 1.25. Both of these values are believed to be universal for a given model and are independent of disorder strength provided the conditions for an infinite-randomness fixed point are met.

4.4 Possible Observation of Quantum Griffiths Effects by Others

There are many examples of the quantum Griffiths effect potentially being observed experimentally. Unsurprisingly, since most of the theoretical work on the effect has been done with regard to magnetic systems, some of the earliest examples are magnetic

systems. In fact, most examples involve magnetic systems. The first example of the possible observation of the effect was in 1991 and was used to describe anomalies in the magnetic susceptibility of $Y_{0.8}U_{0.2}Pd_3$ [44].

The first example in the literature of the quantum Griffiths effect being observed in a superconducting system was in 2015 by Xing et. al [45]. The studied the superconductor-metal transition of gallium thin films as a function of applied perpendicular magnetic field. When looking at the magnetoresistance isotherms measured for their samples, they found a smeared crossing instead of a single crossing. Due to this, standard power-law scaling could not be applied to the system. Instead they applied power-law scaling over successive narrow temperature ranges in a process that I will describe in more detail later.

With the above approach, they were able to determine the exponent product, νz, as a function of magnetic field, and found that it diverged in the limit of the critical magnetic field. Additionally, the divergence fit the form of equation 4.3 with a $\nu\psi$ value of 0.6. This is close to the numerically predicted value of 0.625 (ψ=0.5 and ν=1.25) for the two dimensional random transverse field Ising model. Based on this they concluded that they had observed the quantum Giffiths effect.

Since 2015, a similar divergent exponent product has been observed in many other materials undergoing superconductor-metal transitions including $LaAlO_3/SrTiO_3$ interfaces, $PdTe_2$, Ta_2PdS_5, ultrathin crystalline lead films, ZrNCl, and MoS_2 films [46, 47, 48, 49, 50, 51]. It has also been observed in a system that undergoes a superconductor-insulator transition, TiO [52]. However, in this case the effect is only observed in samples that become weakly insulating, and are probably metallic. In all of these examples a divergent exponent product is taken as evidence of the quantum Giffiths effect occurring. None of them apply activated scaling, which is also expected to describe their data. They also did not explain why the crossing was smeared in the

first place.

Recently, there has been some ongoing debate on the cause of the quantum Griffiths effect in various systems. Many have argued that it is caused primarily by disorder while others have argued for other causes. Zhang et. al. [53] have argued that it is due to size related effects. They studied a series of WSi thin films in a bridge configuration with varying widths. The widest bridges exhibited two stage transitions from a superconductor to Bose insulator to Fermi insulator. In films of intermediate width a direct superconductor to Fermin insulator transition was observed. In the narrowest bridges, narrower than the Pearl length, the quantum Griffiths effect was believed to be observed, once again based on a diverging exponent product.

4.5 Transport Measurements in a Perpendicular Magnetic Field

The amorphous indium oxide films studied for this work were deposited onto pre-patterned SiO_2/Si wafers. This patterning was done using standard photolithography techniques. The pre-patterning included the electrical leads that would lead to the indium oxide film, this is indicated by the central square in figure 4.2, among other features. These other features include in-situ ruthenium oxide thermometers on either side of the indium oxide film. A heating element, made of ruthenium oxide, was deposited on the substrate as well. Additionally, the substrate was etched, using HF, for unknown reasons. This can be seen in figure 4.3. These additional features are present because the samples were originally intended to be used for a different experiment involving the Nernst effect. These additional features are not believed to have affected the transport measurements of the indium oxide film in any way and were not wired during any of the measurements described later in this chapter.

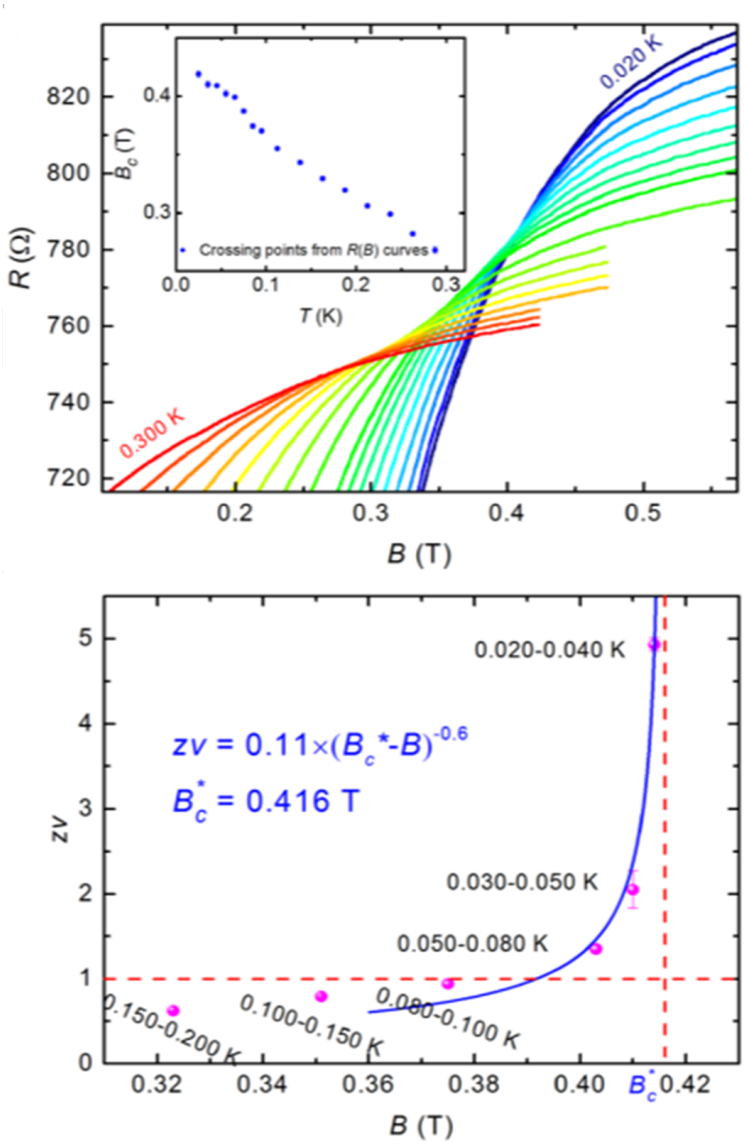

Figure 4.1: From the experiment on $LaAlO_3/SrTiO_3$ interfaces, on the top is a plot of the magnetoresistance isotherms which is zoomed in on the crossing region. This crossing is clearly smeared. On the bottom is a plot of the exponent product as a function of crossing field that includes a fit of the expected functional form [47].

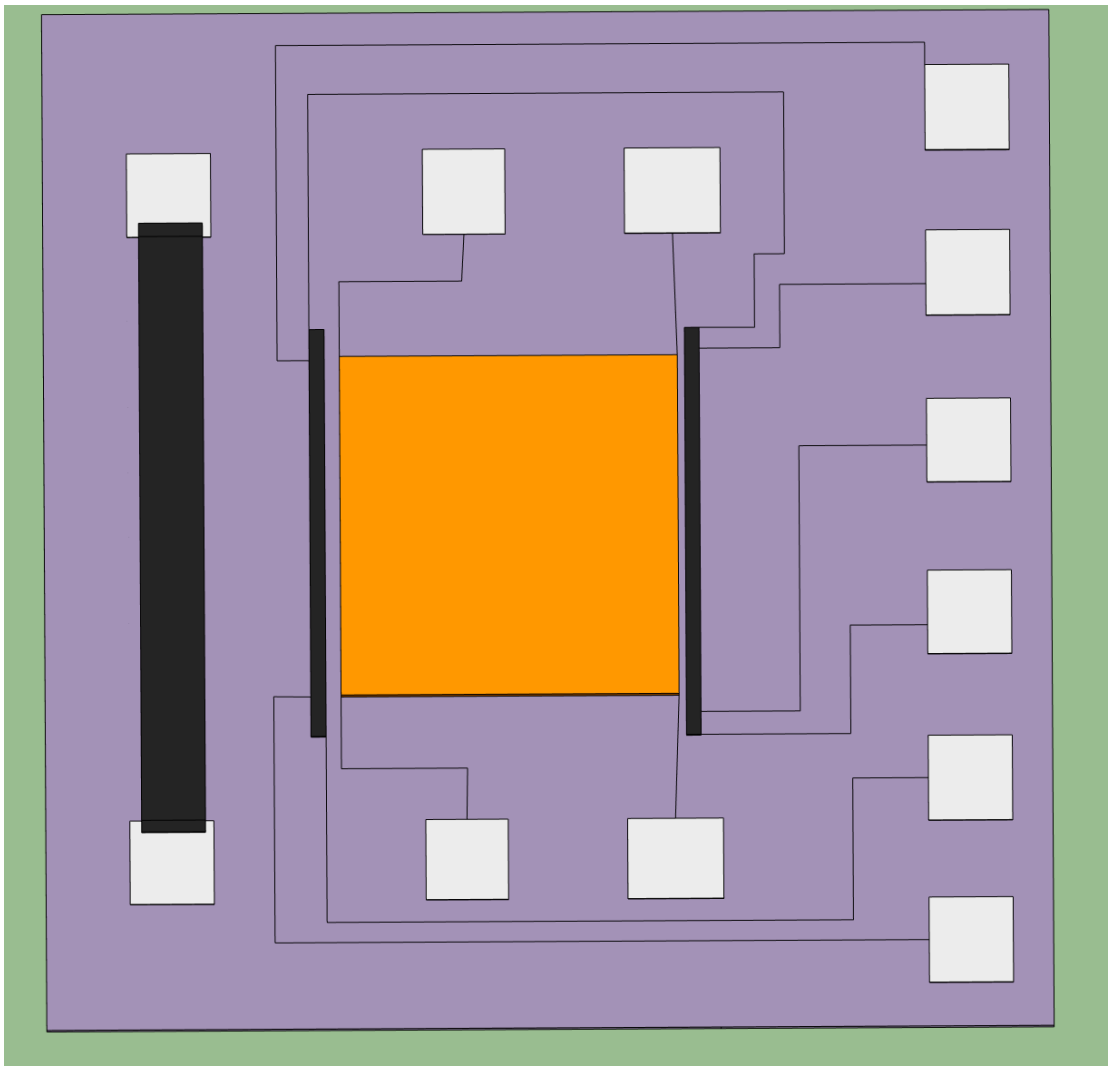

Figure 4.2: Diagram of the indium oxide samples used for these studies. The center square layer is the indium oxide film. The smaller outer squares are contact pads for wire-bonding. The black strips near the indium oxide are the thermometers and the black strip to the left is the in-situ heater.

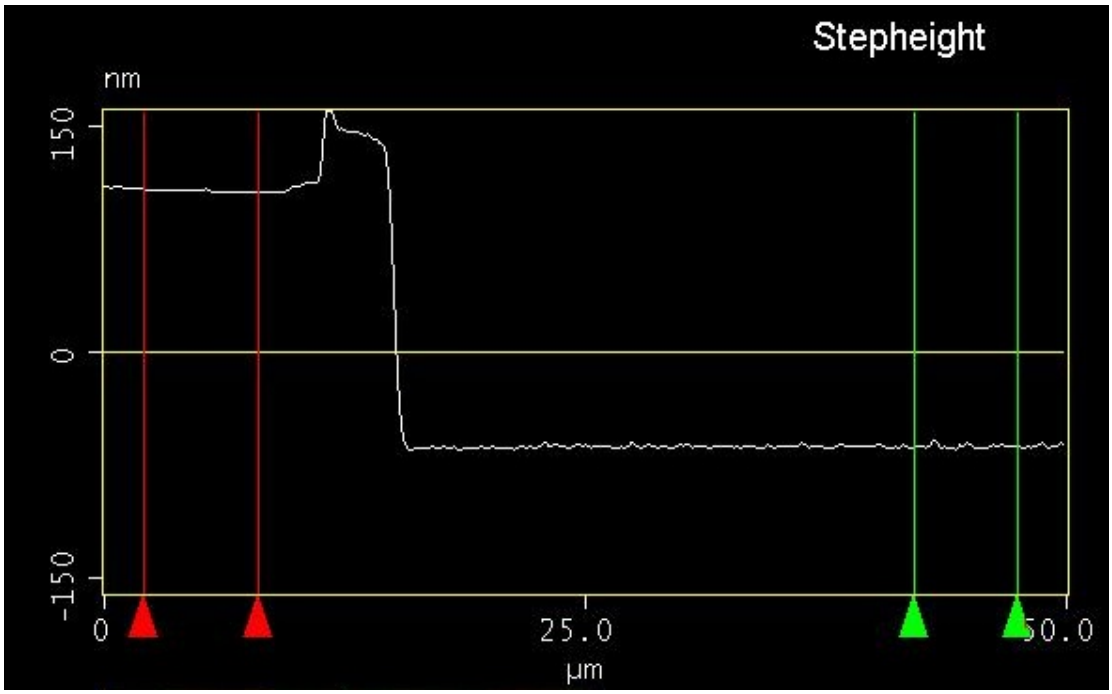

Figure 4.3: AFM measurement trace of indium oxide batch 15 chip 3 showing that etching was done to the substrate. The indium oxide film is about 150nm below the original surface of the SiO_2/Si substrate.

The amorphous indium oxide films studied were approximately 30nm thick. They were grown using electron beam evaporation of In_2O_3 source material in a partial pressure of O_2, between $2*10^{-5}$ and $9*10^{-4}$ mbar. During deposition the substrate temperature was kept below 40°C to prevent crystallization of the films. Since these films were originally intended to be used in another experiment, it was roughly three years after initial deposition that the transport measurements discussed in this chapter were actually carried out. During this time, the films were stored at ambient temperature and in air. Presumably these films gradually annealed during this time, reducing their disorder, but not the carrier concentration [27].

Many samples were deposited with differing oxygen partial pressures during deposition to tune the disorder and carrier concentration. This in turn tuned the resistance of the films and determined whether or not a superconductor to insulator or superconductor to metal transition occurred and at what critical magnetic field. These films were initially characterized in a Quantum Design Physical Property Measurement System (PPMS) with a ^{3}He refrigerator insert prior to more detailed measurement in an Oxford Kelvinox-25 (K25) dilution refrigerator. Initial characterization was done in a PPMS because it could cycle between different samples twice a day versus once a week for the dilution refrigerator. Detailed measurements were done in the dilution refrigerator because it can reach lower temperatures and allows for lower electrical noise levels in the measurement circuit.

To characterize the films, the resistance was measured at various temperature points from the base temperature of the ^{3}He insert up to 4.0K. The resistance measurements were made by sourcing a constant current of 200nA DC across one side of the sample, using a Keithley 6221 current source, and measuring the voltage across the opposite side, using a Keithley 2182 nanovoltmeter. Resistances were measured using a four-contact configuration to eliminate contact and lead resistance. Measurements were also

carried out in orthogonal directions and the contact configuration was changed using a Keithley 7001 switch system. These resistance versus temperature sweeps were done in both zero applied magnetic field and in a 9T perpendicularly applied magnetic field for all of the tested samples. Additionally, voltage versus current sweeps were measured at various temperatures and the source current for the resistance versus temperature sweeps was chosen such that it fell within the linear regime of the base temperature IV characteristic. This was done to limit self-heating due to the measurement current.

Five samples were characterized in the PPMS and three of them did not have the desired properties. Indium oxide batch 6 chip 1, batch 13 chip 2, and batch 13 chip 3 were too metallic, as can be seen in figure 4.4. These films were still superconducting at the lowest temperatures and with a 9T perpendicular applied magnetic field, the highest field available with the PPMS. Since it could not be verified that these films could be driven out of the superconducting state by the 12T maximum magnetic field of the Kelvinox-25, and even if they could, not much of the metallic or insulating side of the transition would be accessible, it was decided that these films were not worth measuring in more detail.

Indium oxide samples batch 15 chip 2 and batch 15 chip 3 were able to be driven out of the superconducting state with a 9T perpendicular applied magnetic field, shown in figure 4.5. The zero-field transition temperatures were approximately 2.8K. Indium oxide samples that exhibit a quantum phase transition typically undergo a superconductor-insulator transition. These samples were found to undergo a superconductor-metal transition instead, as will be shown in more detail later. They were more metallic than typical samples, likely as a result of annealing and a corresponding decrease in disorder of the films.

Samples batch 15 chip 2 and batch 15 chip 3 were measured in much more detail and down to lower temperatures in the K25. Resistance versus temperature traces were

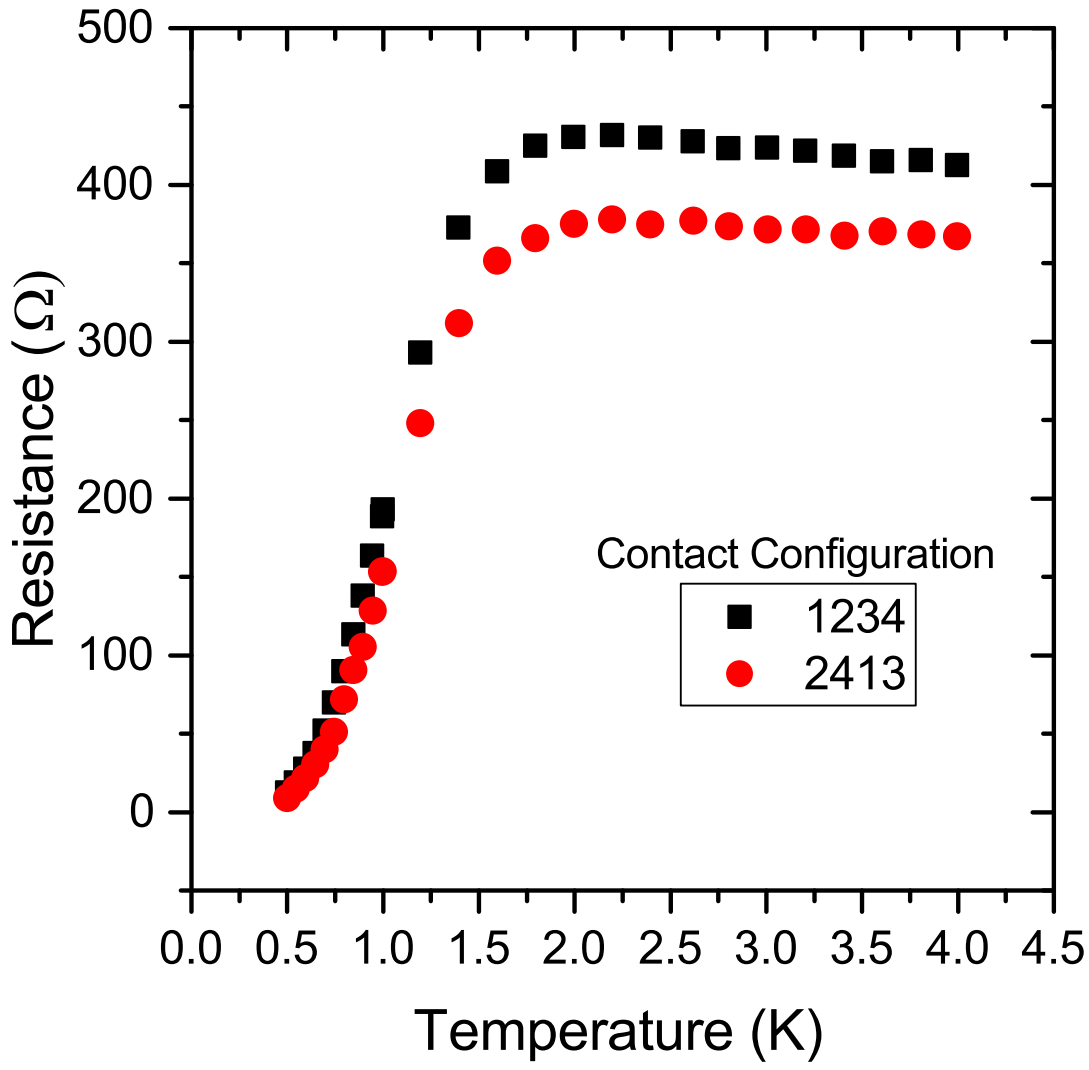

Figure 4.4: Resistance versus temperature plot for indium oxide batch 13 chip 3 with a 9T perpendicular applied magnetic field. Both contact configurations, in orthogonal directions, are shown with squares and circles.

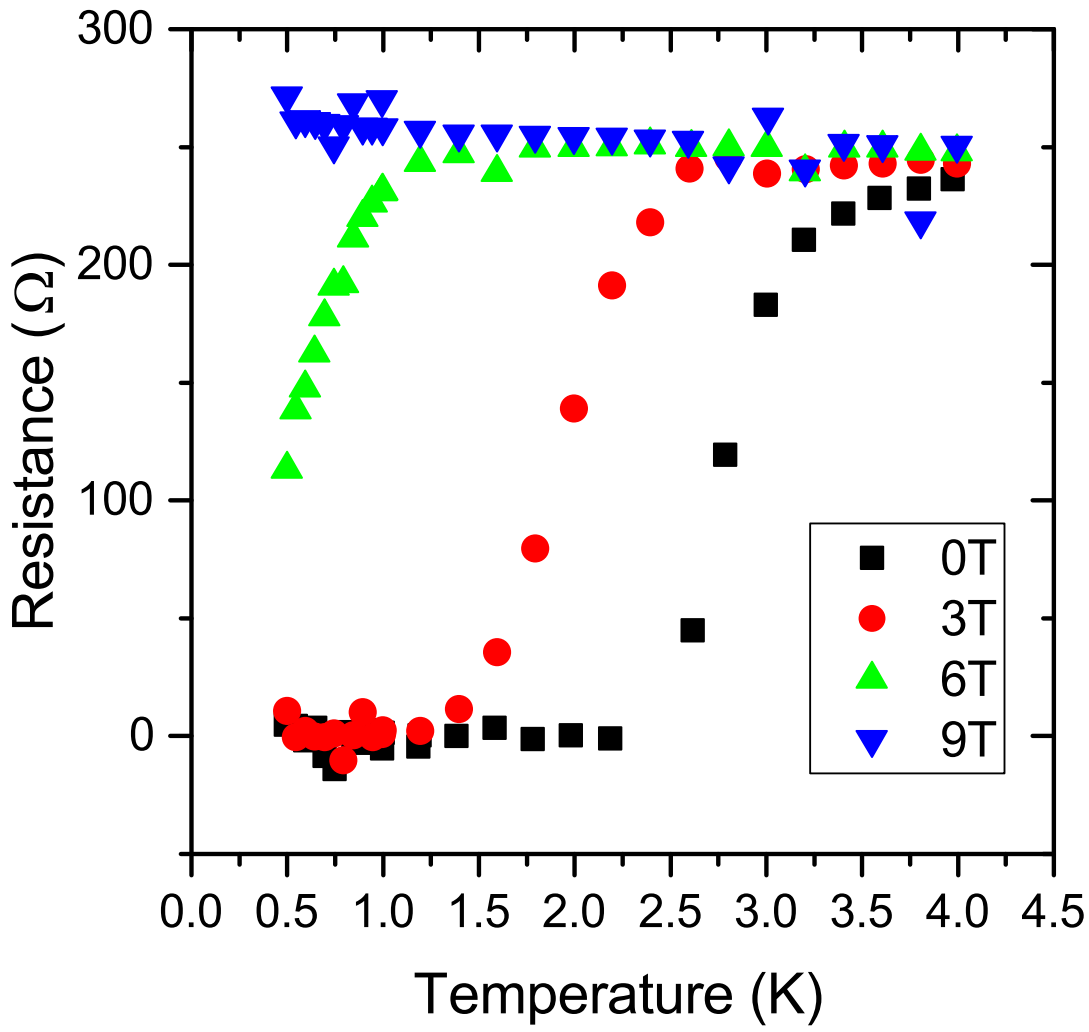

Figure 4.5: Resistance versus temperature plot for indium oxide batch 15 chip 3 with 0, 3,6, and 9 T perpendicular applied magnetic fields. Data for only one of the two measured contact configurations is shown.

measured with many different applied perpendicular magnetic field values ranging from zero field up to 12T. The first sample to be measured in the K25 was batch 15 chip 3. The resistance was measured using the same model Keithley instruments as was used for the measurements in the PPMS, however a different measurement technique was used.

Instead of applying a constant DC current, a pulsed current technique was used. With this technique the Keithley 6221 current source would send a pulse of current across the sample for a set amount of time, 12ms in this case. Then it would send a signal to the Keithley 2182 nanovoltmeter to measure the voltage after a set delay, 6 ms in this case. These pulses were synchronized with the power line cycle used to power the instruments in order to minimize the noise. Between pulses there was a wait time set in the number of power line cycles. This wait was 100 power line cycles at 120mK and below. Above this temperature the wait was 80 power line cycles. This technique was used to limit the heating of the film due to the measurement current. The limited amount of time that the current is on limits the energy dissipated and the time between pulses allows the film to cool between successive measurements.

To balance the need for an adequate signal-to-noise ratio with the need to limit Joule heating, the measurement current was carefully chosen. Below 250mK, where heating effects are most likely to be an issue, the current pulse was 50nA. Above this temperature the current pulse was 200nA. To reduce the uncertainty in the resistance at the lowest temperatures the voltage measurement was averaged over 100 pulses below 250mK instead of the 25 pulses at higher temperatures. This resulted in an uncertainty of approximately 0.4Ω below 250mK, and 0.2Ω at higher temperatures.

Similar to what was done when measuring in the PPMS, the contact configuration was changed using a Keithley switch system to allow measurement of the resistance

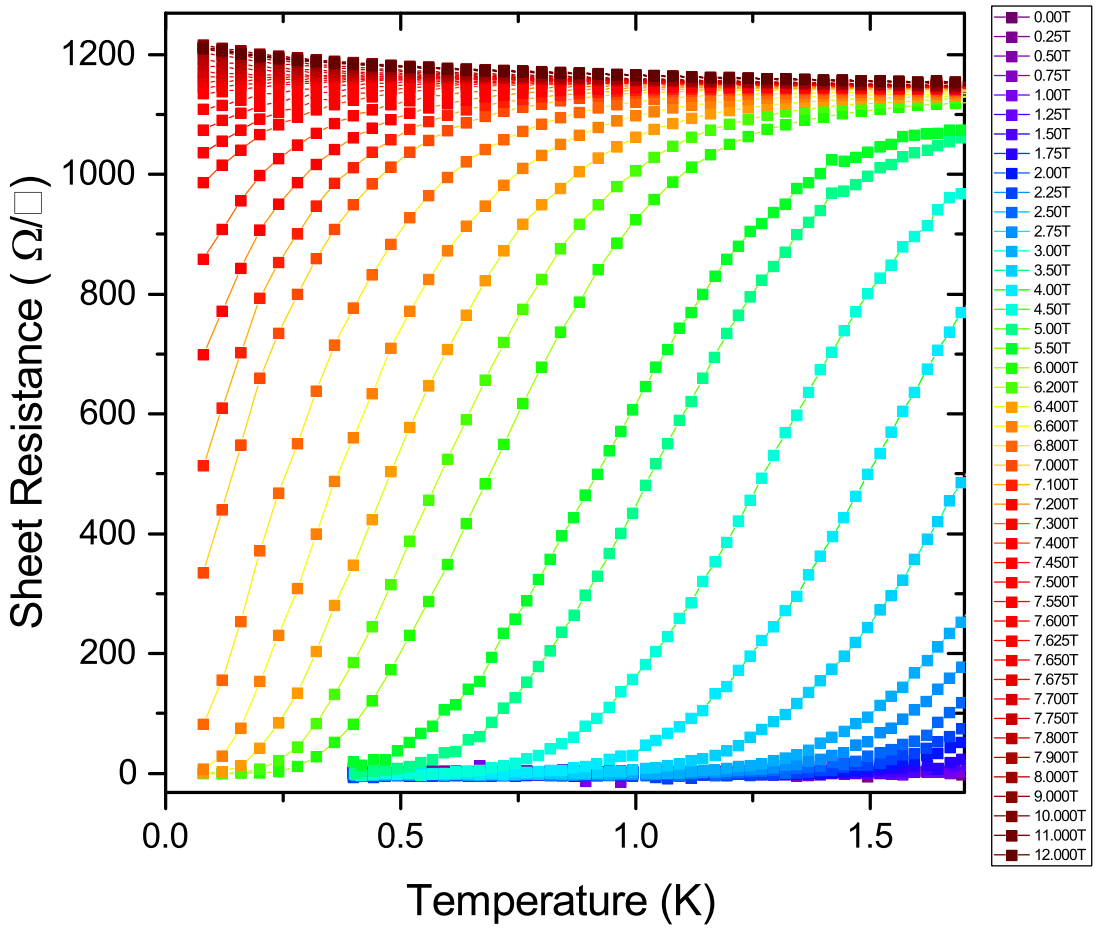

Figure 4.6: Sheet resistance versus temperature sweeps for batch 15 chip 3 at various applied perpendicular magnetic fields measured in the Kelvinox-25.

along orthogonal directions. By measuring the resistance along vertical and horizontal directions the Van der Pauw method could be used. With this method the sheet resistance could be calculated using the following equation [54],

$$e^{-\pi R_{vert.}/R_s} + e^{\pi R_{horiz.}/R_s} = 1 \tag{4.5}$$

where R_s is the sheet resistance. This has units of $\Omega/\square$ and takes the resistivity and thickness into account, but does not depend on the geometry of the film. This makes it easier and more useful to compare with resistance values measured for different samples and values stated in the literature.

Looking at the sheet resistance versus temperature traces, figure 4.6, it can be seen that with applied perpendicular magnetic field, the film is driven from the superconducting state and towards a metallic state. This is signified by the temperature dependence of the resistance, dR/dT changing sign at a perpendicular field of B≈7T. The resistance at this transition is much lower than what is typical of a direct superconductor-insulator transition. The resistance at the transition is ∼1150Ω/□ instead of the quantum resistance for Cooper pairs, $h/4e^2$ (6450Ω/□).

The metallic behavior of the film in high fields was further verified by looking at the conductance of the film plotted against the logarithm of the temperature (figure 4.7). The linear dependence of the conductance for fields above 7.8T is consistent with weak localization in a 2D metallic system [55, 56]. The flattening below ln(T)=-2.0 is likely due to failure to cool and corresponds to a temperature of ∼135mK. Additional evidence for metallic behavior is provided by Hall effect measurements of the film.

The Hall resistance for sample batch 15 chip 3 was measured as a function of perpendicular magnetic field at three different temperatures. Since the film is not of the typical hall bar geometry used for Hall effect measurements, a slightly modified approach was taken to make this measurement. Current was applied across diagonal corners of the film and the voltage was measured across the other two corners. This measurement was

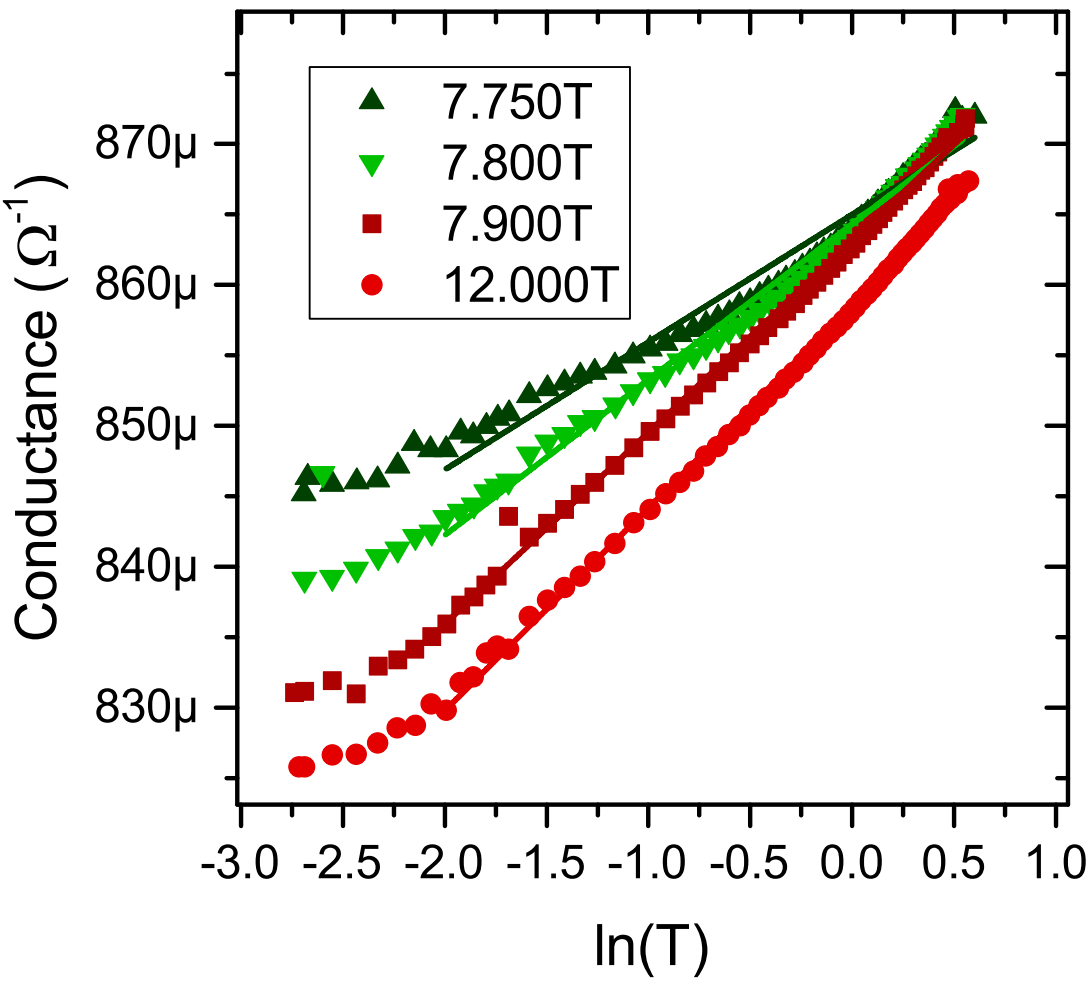

Figure 4.7: Conductivity versus the logarithm of the temperature for batch 15 chip 3. The linear dependence above 7.8T indicates metallic behavior. The straight lines are added to guide the eye.

done in orthogonal directions and using a pulsed current technique as described earlier. The measured voltage was averaged over these two directions and over 100 pulses. The current pulse was 100nA. The Hall resistance was taken to be this average voltage divided by the current.

In the superconducting regime the Hall resistance was zero, to within the experimental uncertainty, as would be expected (figure 4.8). For higher magnetic fields, above ∼8T, the hall resistance varied linearly with applied magnetic field, as would be expected for a metal. However, between these two regimes, indicated by the shading, the Hall resistance rises quickly. It doesn't fall neatly into superconducting or metallic behavior.

Between the superconducting and metallic regimes, an anomalous metallic regime was observed. In this regime the Hall resistance is non-zero and also does not have a linear dependence on magnetic field, indicated by the middle region in figure 4.8. Additionally, the conductance did not vary linearly with ln(T) as would be expected for a metal, yet the resistance did not fall to zero at the lowest temperatures. This is believed to be due to a failure to cool the electrons at the lowest temperatures, since $dR/dT>0$ in this regime, suggesting the onset of superconductivity. The transition between $dR/dT>0$ and $dR/dT<0$ is taken to be the boundary between the metallic and superconducting ground states.

Using the resistance versus temperature sweeps, magnetoresistance isotherms were generated. This was done by first interpolating the R(T,B) curves so that at each magnetic field value each temperature had a corresponding resistance value. Once a R(T,B) data set with uniform temperature points was generated, magnetoresistance isotherms were generated by carrying out a matrix inversion of the temperature swept data. At first glance the isotherms (figure 4.9) appear to cross at a single point as would be typical for a superconductor-insulator transition. However, looking at the crossing in

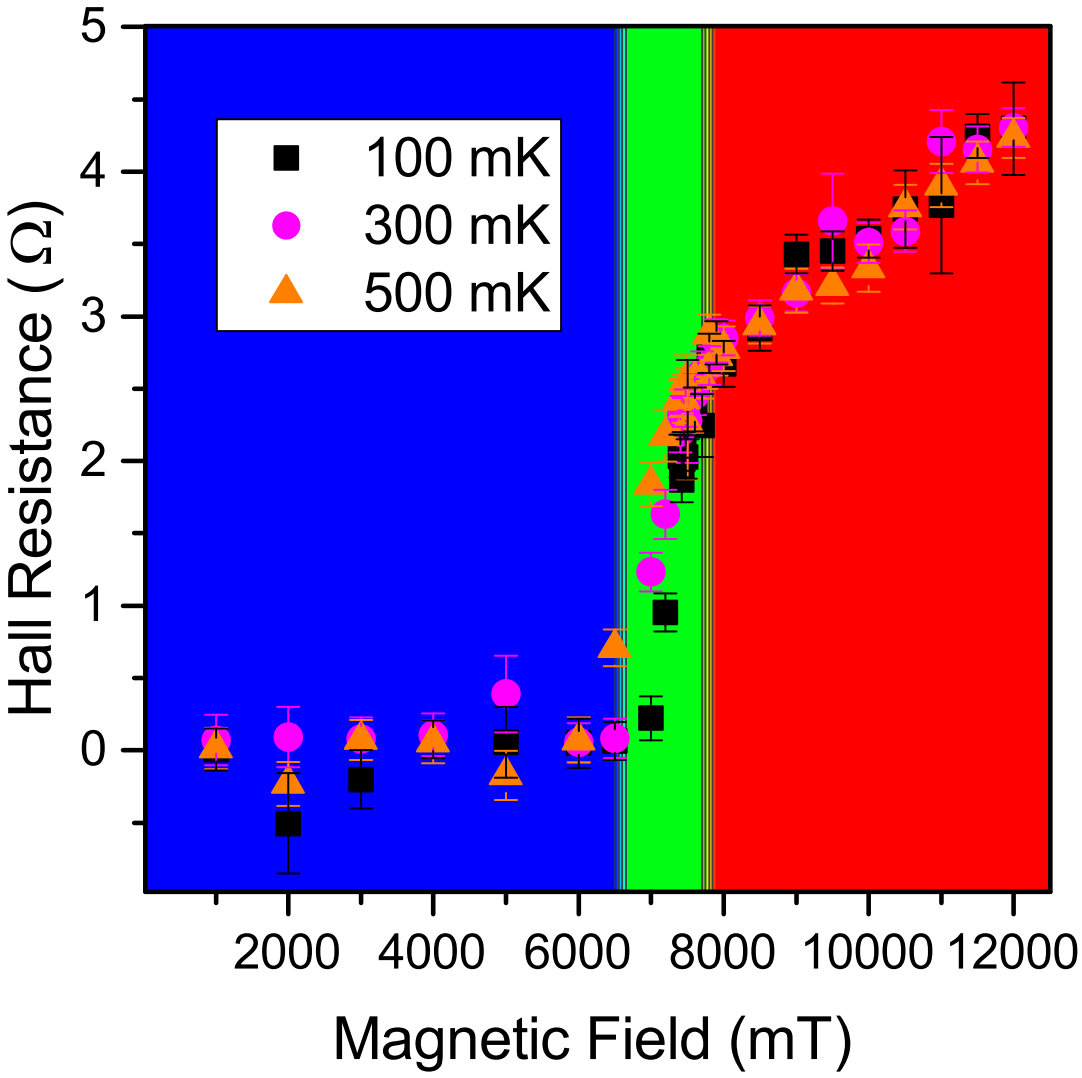

Figure 4.8: Hall resistance versus applied perpendicular magnetic field for sample batch 15 chip 3. The left region corresponds to the superconducting regime, the right to the metallic, and the middle region to an anomalous metallic regime.

more detail revealed that there was a continuum of crossing points spread over a range of temperatures and magnetic fields. The crossing points clearly had both temperature and field dependence and was not just random noise around some average value. This dependence will be looked at more closely in the following sections.

Indium oxide sample batch 15 chip 2 was measured in detail several months after batch 15 chip 3. This sample was measured to see if similar behavior could be seen in another sample and to try to improve the quality of the data and reduce the experimental error with more careful measurements. The transport measurements were conducted using a modified measurement technique and improved temperature measurement.

The first change made was to improve the accuracy of the measured temperature. This was done by installing another thermometer on the sample holder of the K25. Previous temperature readings were taken using a ruthenium oxide thermometer mounted on the mixing chamber of the refrigerator. This thermometer had been used for more than a decade and there was no independent means of temperature measurement to verify the calibration of this thermometer. Additionally, since the sample is mounted about 30 cm away from the mixing chamber the possibility of a thermal gradient between the mixing chamber and the sample could not be ruled out.

Both of these issues were solved with the new thermometer. The new thermometer was a Lake Shore Cryotronics ruthenium oxide thermometer, model RX-202A-AA-0.05B-QT. This thermometer came independently calibrated by the manufacturer from 50mK to 40K. It was also mounted on the sample holder itself, within 2cm of the sample, instead of on the mixing chamber. When given enough time to come to thermal equilibrium, this thermometer read about 8mK lower than the mixing chamber thermometer. During the temperature sweep it would lag behind the mixing chamber thermometer by as much as 15mK at times. Clearly both thermal gradients and calibration were issues when relying on the other thermometer.

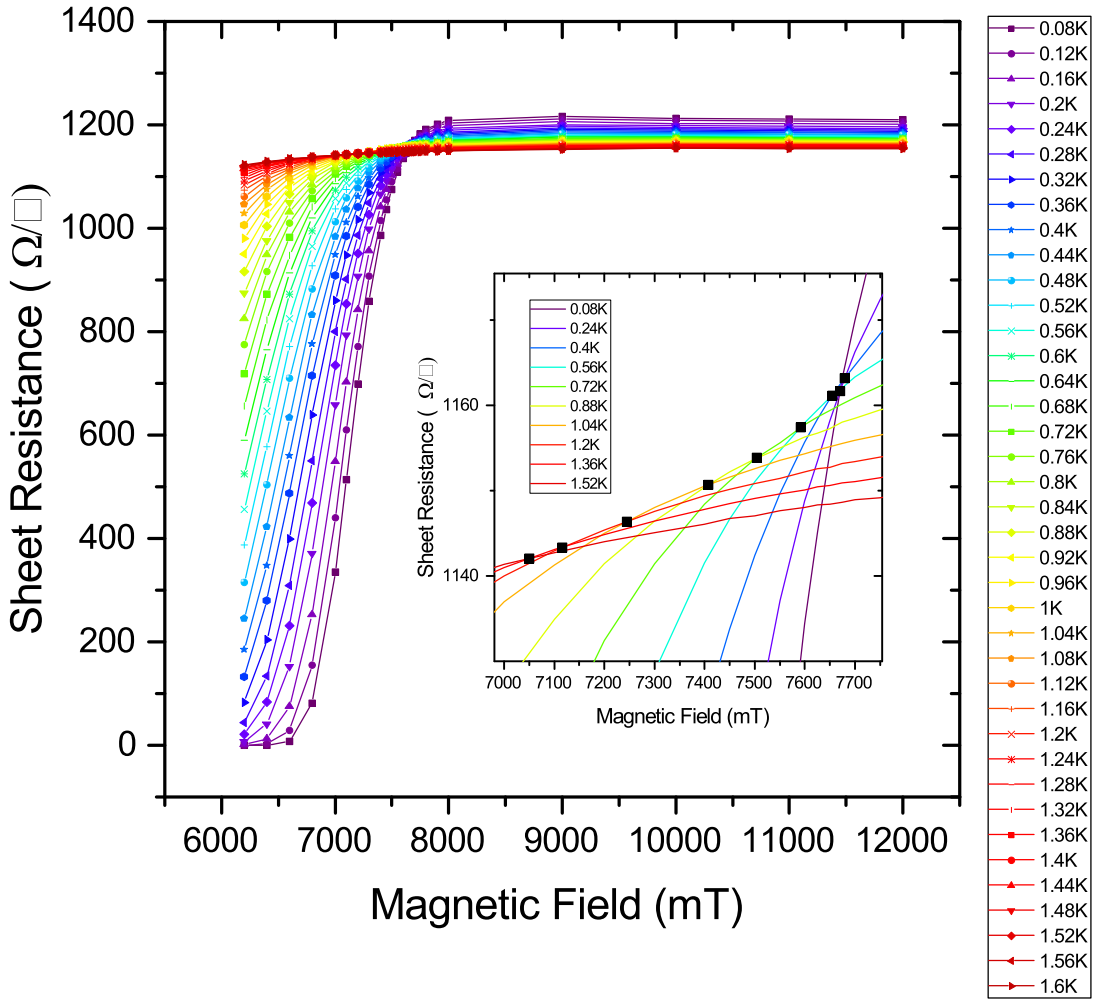

Figure 4.9: Resistance versus magnetic field isotherms for batch 15 chip 3. Inset: Select isotherms zoomed in on the crossing region to show a smeared crossing as opposed to a single crossing point. The black squares indicate the crossing of neighboring isotherms.

An AC measurement technique was attempted with this sample. Using the Keithley 6221 an AC current of 40nA was applied across the sample at a frequency of 17Hz. The voltage was measured using a Stanford Research Systems SR2124 lock-in amplifier. Once again the contact configuration was changed using a switch system so that the Van der Pauw method could be used to find the sheet resistance. This AC technique allowed for lower measurement currents, resulting in less heating, and less random noise in the voltage measurement due to the filtering nature of lock-in amplifiers. Unfortunately, the error between sensitivity settings on the lock-in amplifier was much greater than the random noise from using a DC measurement. Due to this error, the AC method proved to be worse than the original DC method.

The same pulsed DC measurement technique was used with the exception of measuring more carefully near the transition region at the lowest temperatures. The measurement current was decreased to 10nA and the number of pulses was increased to 1000, at 150mK and below. For the 180mK and 200mK data the current was 100 and 250nA, respectively. For both cases 600 pulses were averaged. This resulted in an experimental uncertainty of less than 0.1Ω near the transition.

The resulting resistance versus temperature sweeps at various applied magnetic fields showed very similar behavior to what was observed in the previous sample (figure 4.10). The film was superconducting at the lowest magnetic fields and showed metallic behavior in larger applied fields. This transition occurred around B≈7T, again, although at a slightly lower field than with the previous sample. Once again in the metallic state the conductance versus natural logarithm of temperature was linear, as expected (figure 4.11).

Once again, the resistance versus temperature sweeps were used to generate a series of magnetoresistance isotherms. These isotherms also have a smeared crossing with temperature and magnetic field dependence. This can be seen in the inset of figure 4.12.

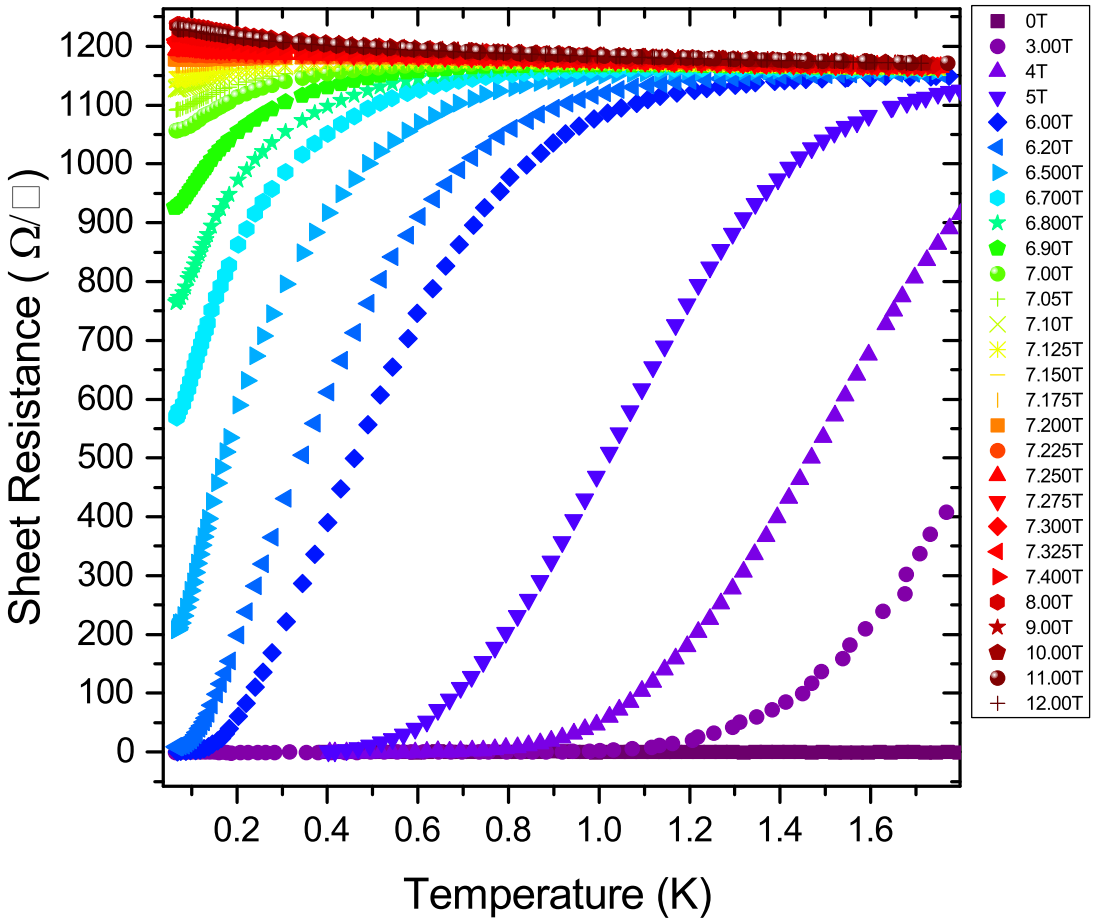

Figure 4.10: Sheet resistance versus temperature sweeps for batch 15 chip 2 at various applied perpendicular magnetic fields measured in the Kelvinox-25.

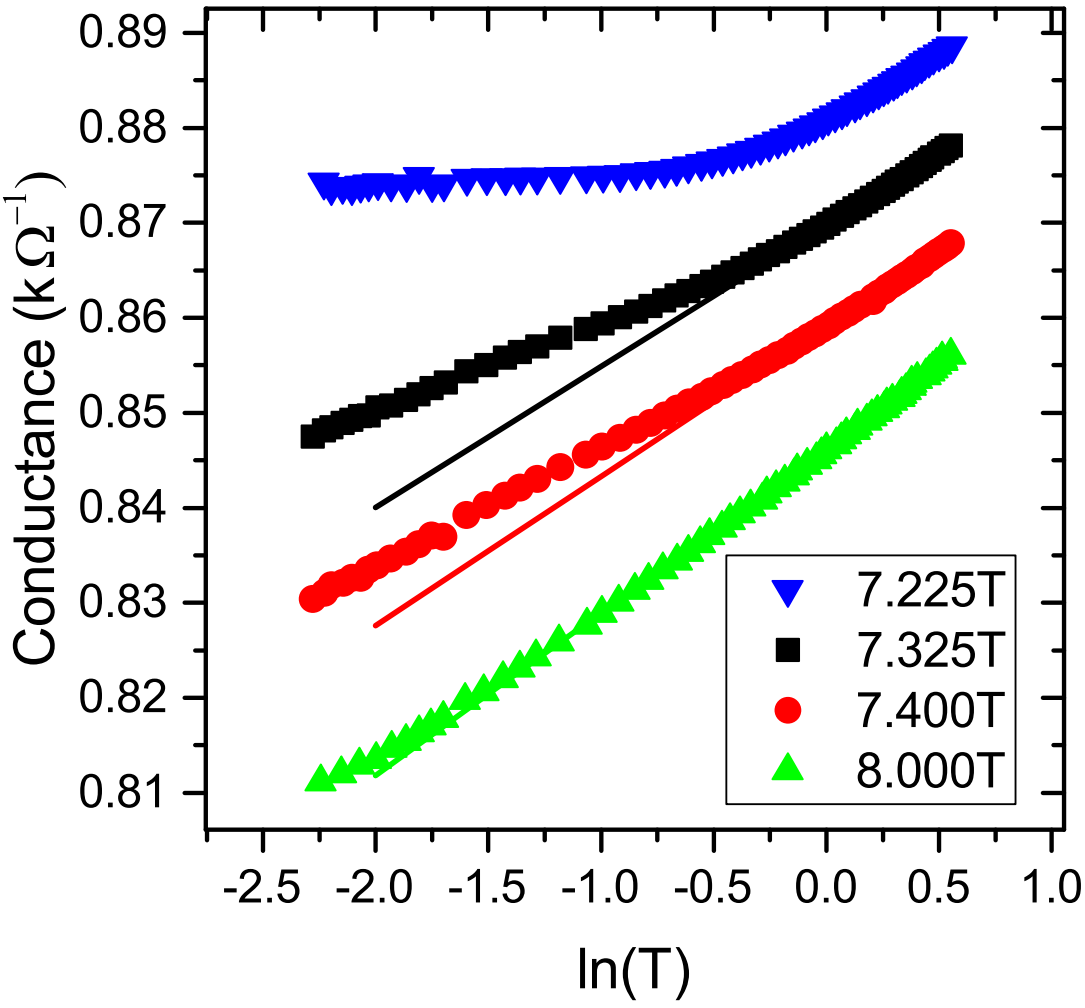

Figure 4.11: Conductivity versus the logarithm of the temperature for batch 15 chip 2. The linear dependence above 7.325T indicates metallic behavior. Once again, the straight lines are added to guide the eye.

The crossing points between neighboring isotherms are marked with a black square. This behavior is qualitatively the same as previously observed, but shifted to lower magnetic fields.

As can be seen, both of the samples studied underwent superconductor-metal transitions as the applied perpendicular magnetic field was varied. Both also had unconventional smeared crossings points that were not just random noise around some average value. Instead there was a systematic change in the crossing point as the temperature and magnetic field was varied. The next sections will go over this dependence in more detail and go over its implications.

4.6 Power-law Scaling Analysis

In the past when a smeared crossing of magnetoresistance isotherms at a quantum phase transition has been observed by others, generally the sample has been disregarded. It has typically been assumed that the smearing was due to various regions of the sample undergoing the transition at different values of the quantum tuning parameter, independent from the film as a whole. This would correspond to the case where the dimensionalities of any rare regions are greater than the lower critical dimension of the system. In this case the sample is not expected to have any sort of scaling behavior. At first this seems like a reasonable assumption to make based on the data. In effect the sample was inhomogeneous. However, further analysis shows that this is not the case.

In 2015 when Xing et al. [45] observed a qualitatively similar superconductor-metal transition in gallium thin films, they eventually concluded that the quantum Griffiths effect had been observed. The rest of this section will follow an analysis similar to what they used.

Since there was not a single crossing of the magnetoresistance isotherms the standard power-law scaling analysis could not be used. This unusual phenomenology required a

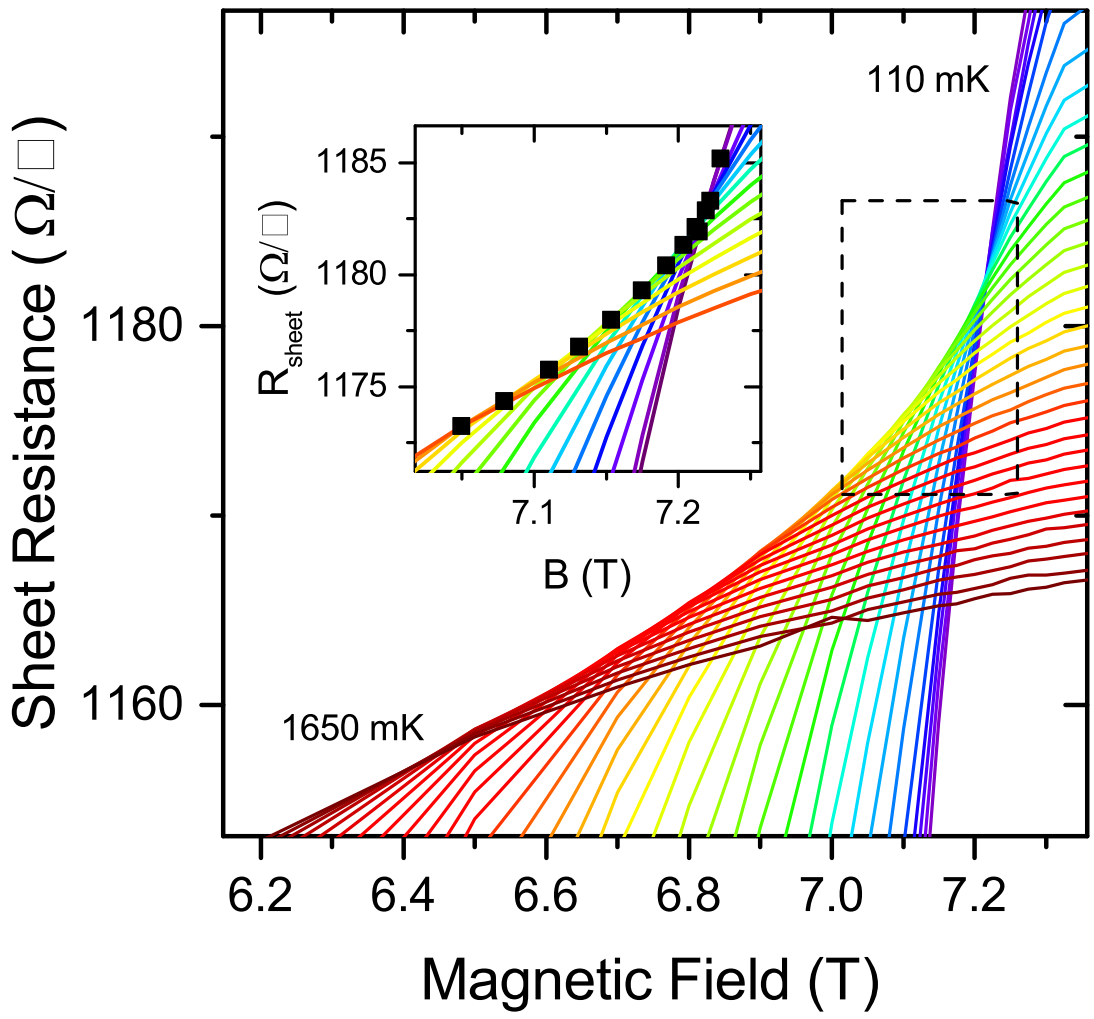

Figure 4.12: Resistance versus magnetic field isotherms for batch 15 chip 2 zoomed in on the crossing region. Inset: Select isotherms zoomed in further on the crossing region to show the crossing points as indicated by the black squares.

modified approach to the standard power-law scaling analysis. Instead of scaling data measured over a wide range of temperatures around a single critical field, data measured over a series of narrow temperature intervals was scaled around a well-defined crossing point $B_x(T)$. Over these narrow intervals the standard power-law scaling was used.

The first step in this modified power-law scaling analysis was to determine the crossing field as a function of temperature (figure 4.13). Many resistance versus temperature sweeps were measured in and near the crossing regime to ensure adequate data density once the magnetoresistance isotherms were generated. Even with the higher data density, more than one crossing occurred between two magnetic field values in some cases. To overcome this fitting was used.

Over a narrow region, near the crossing, the magnetoresistance isotherms could be approximated as quadratic in field. The crossing point was found by fitting neighboring isotherms with a quadratic using several points on either side of the crossing and determining where the best fit lines crossed. The crossing was assigned a temperature equal to the average temperature of the neighboring isotherms. Additionally, the uncertainty in the crossing field was estimated using the uncertainty in the resistance measurement. The interval over which the difference between the best fit lines of resistance versus magnetic field were less than or equal to the uncertainty in the resistance, were taken as the error bounds for the crossing field.

The crossing field was found to vary systematically as the temperature varied. For batch 15 chip 3, the crossing field saturated in the limit of zero temperature at a value of approximately 7.7T. As the temperature increased the crossing field decreased and it reached a value of $\sim$6.5T at the highest temperature measured, 1.7K. This is shown in figure 4.13.

Once the crossing fields were found power-law scaling analysis could be applied to successive narrow temperature intervals, using the average crossing field value within

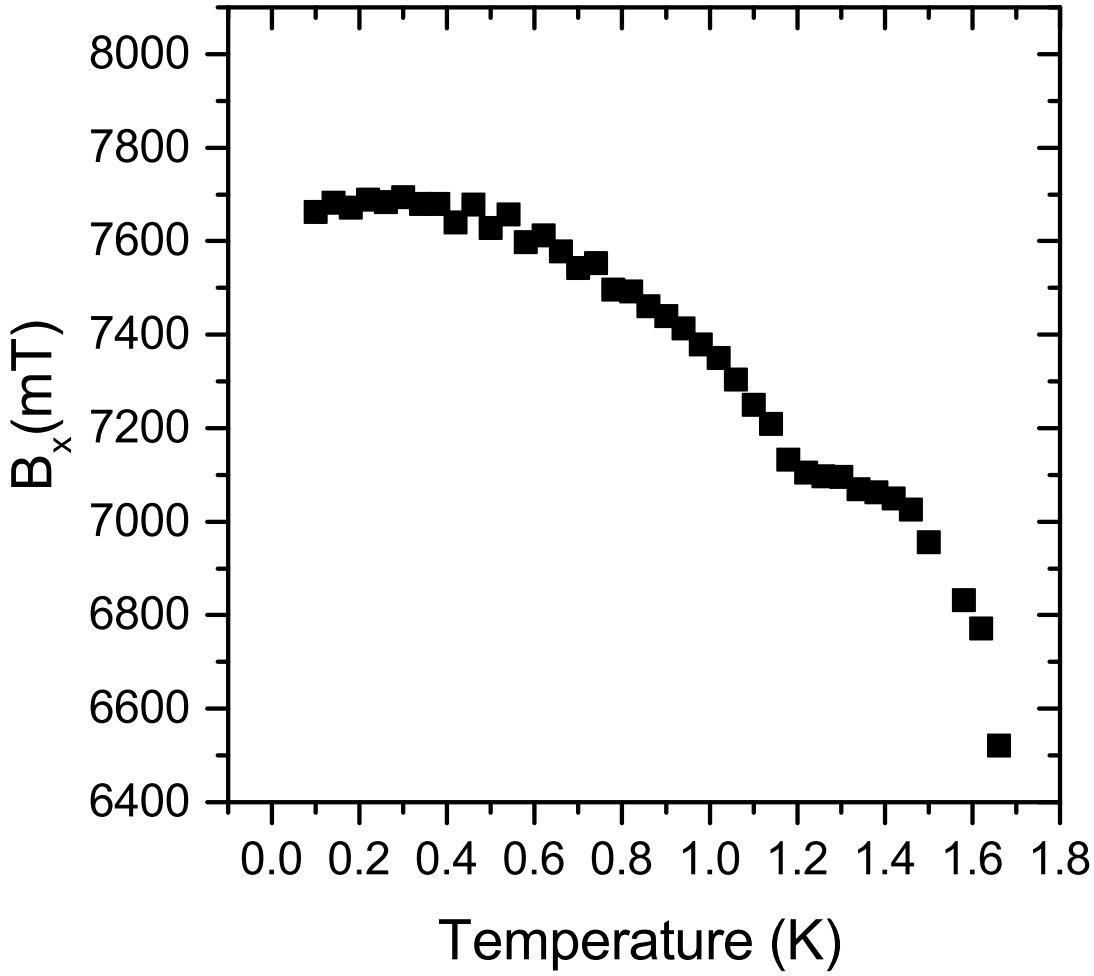

Figure 4.13: Crossing field versus temperature for sample batch 15 chip 3.

that interval as the critical magnetic field. The value of the exponent product, νz, that resulted in the best collapse of the data was found. To do this it was important to quantify the extent to which the curves collapsed. This was done by considering points near the crossing, where the logarithm of the scaling function, Φ, could be approximated as linear as a function of the scaling parameter.

Using a programming script written in Matlab, many different values of νz were tested and the difference in the slope of ln(R) vs $\delta T^{-1/\nu z}$ for the lowest temperature in the interval and the others was tracked for both the upper and lower branches of the plot. The upper and lower branches correspond to resistance values above and below the critical resistance, respectively. The νz value that minimized these two slope differences combined was taken as the value that resulted in the best collapse. This value of νz was assigned a temperature equal to the average temperature of the isotherms in the interval and the critical field at that temperature. With this technique, νz as a function of both temperature and critical field could be found, shown in figure 4.14 and figure 4.15, respectively.

Looking at figure 4.14, it is clear that the exponent product increases as the temperature decreases. It also potentially diverges in the limit of zero temperature. Looking at figure 4.15, the exponent product increases as the crossing field increases and reaches a maximum at some finite maximum crossing field. This also looks like it could potentially diverge as some maximum crossing field is reached. This is qualitatively consistent with the quantum Griffiths effect, as shown by equation 4.3. Similar behavior has been observed by others in different materials.

Even though this behavior is qualitatively consistent with the quantum Griffiths effect, it is far from conclusive. As was mentioned earlier, a system exhibiting the quantum Griffiths effect and having an infinite-randomness fixed point is expected to follow activated scaling instead of power-law scaling. An important improvement in

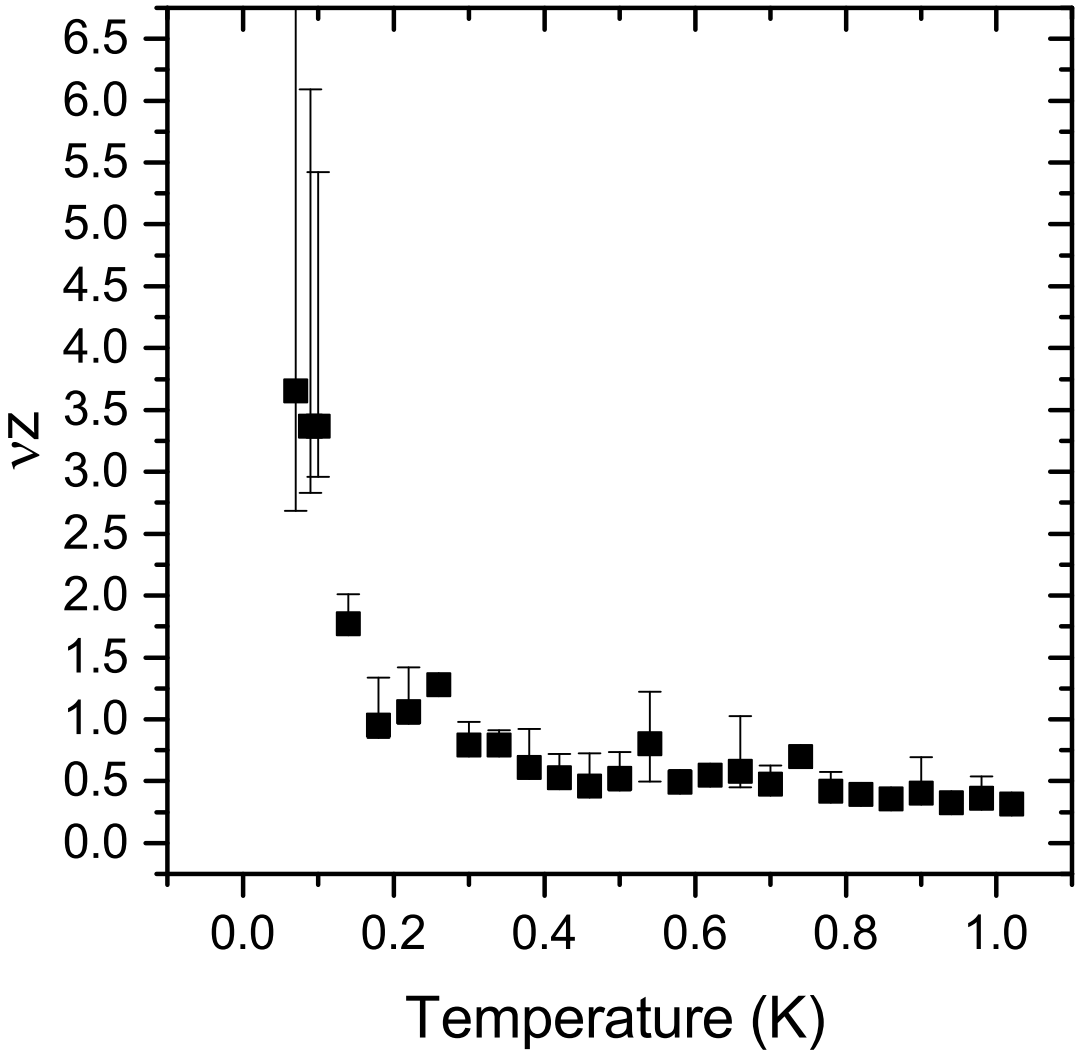

Figure 4.14: Exponent product, νz, as a function of temperature as found by the modified power-law scaling technique. This is for sample batch 15 chip 3. The upper and lower bound of the error bars correspond to the values that best minimize the difference in slopes for the upper and lower branches.

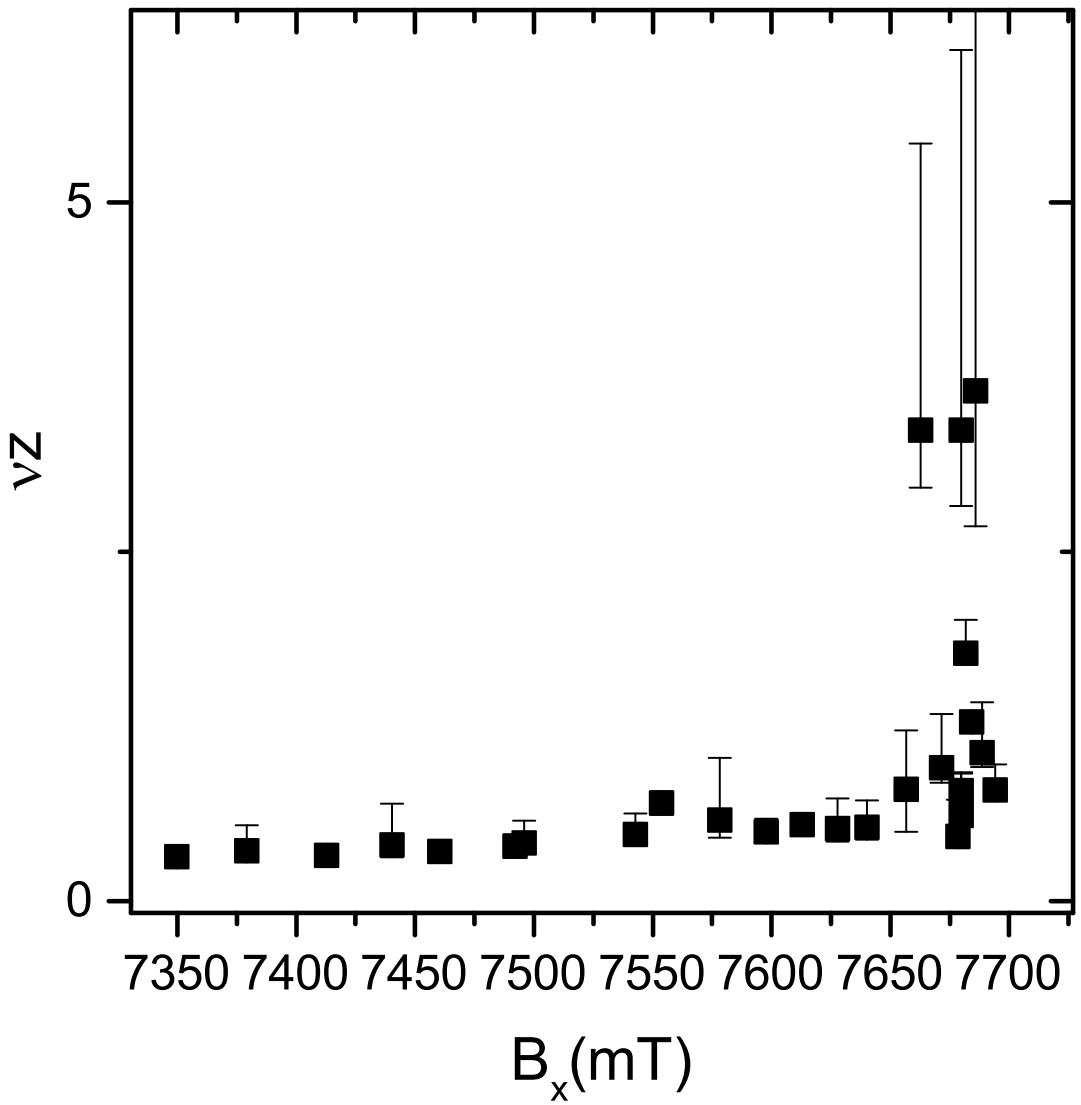

Figure 4.15: Exponent product, νz, as a function of crossing field, B_x, as found by the modified power-law scaling technique. This is for sample batch 15 chip 3.

the analysis was made by quantifying the relationship between activated scaling and conventional power-law scaling.

4.7 Power-law vs. Activated Scaling

To quantify the relationship between activated and power-law scaling, the scenario where a system governed by activated scaling, but analyzed using power-law scaling was considered. It is shown in the appendix that in such a scenario there will be an effective value of the exponent product, νz, that varies systematically. Specifically the effective value of νz is expected to vary with temperature in the following way [57],

$$\frac{1}{(\nu z)_{eff}} = \frac{1}{(\nu\psi)_{eff}} \frac{1}{ln(T_0/T)} \tag{4.6}$$

where ψ once again is the tunneling exponent and T_0 is a microscopic temperature scale. Additionally, it has been shown [6] that the dynamical critical exponent should diverge as the critical point is approached and for the case of a magnetic field tuned transition the exponent product takes the following form:

$$\nu z = C|B_x - B_c|^{-\nu\psi} \tag{4.7}$$

where B_x is the crossing field at a given temperature and B_c is the critical magnetic field. C is a fitting parameter.

The uncertainty in the values of νz found for sample batch 15 chip 3 were too large to fit either equation 4.6 or equation 4.7 to the data in a meaningful way. However, due to improved measurement techniques, the uncertainties in the measured resistance values for batch 15 chip 2 were lower. This resulted in reduced uncertainty in the νz values when the modified power-law scaling analysis was applied. The reduced uncertainty allowed for a meaningful fit of equation 4.6 and equation 4.7 to the data.

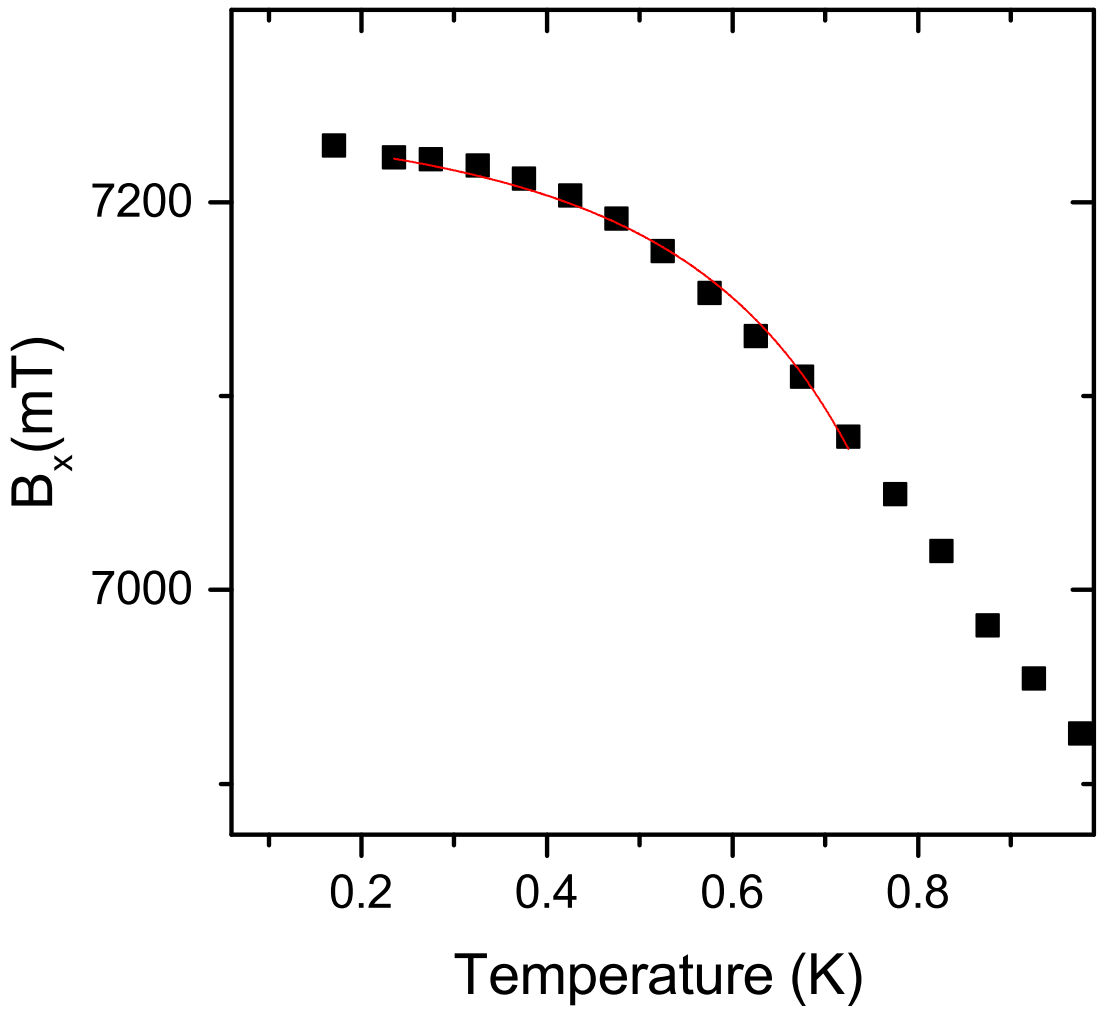

Figure 4.16: Crossing field versus temperature for sample batch 15 chip 2. The solid line is a fit to equation 4.9 which takes into account corrections to scaling. These corrections to scaling will be described in more detail later.

Looking at figure 4.17, once again $(\nu z)_{eff}$ increases as the crossing field increases. It appears to potentially diverge as the maximum crossing field of 7245±10mT is approached, shown in figure 4.16. For this fit the exponent product, $\nu\psi$=0.6, was fixed, as others have done [45, 47]. This value of ν is close to the numerically predicted value of 0.625 for random transverse field Ising model. As explained earlier, superconductor-metal transitions are theoretically believed to belong to the same universality class as this model. This fit provides some evidence of that being the case.

Just like with the previous sample, $(\nu z)_{eff}$ increases as the temperature decreases. As T⇒0 it appears that $(\nu z)_{eff}$ possibly diverges. This is corroborated by the fit of equation 4.6 to the data (figure 4.18). This two-parameter fit yielded T_0=1.21±0.05K and an effective exponent product $(\nu\psi)_{eff}$=0.616±0.020. This is in good agreement with the numerically predicted value of 0.625 and is consistent with the exponent versus crossing field fit. This provides further evidence that the quantum Griffiths effect occurred and that the quantum critical point of this superconductor-metal transition is an infinite-randomness fixed point.

The fits of equations 4.6 and 4.7 to the effective exponent product data and the consistency of the fits provided the strongest evidence to date in the literature for the observation of an infinite randomness fixed point. However, it would be ideal to show that the transport data follows activated scaling as has been theoretically predicted. The fitting parameters from these fits provide a vital starting point for carrying out that analysis.

4.8 Activated Scaling

Prior to the analysis done on sample batch 15 chip 2 [57] there were no examples in the literature of an activated scaling analysis carried out on any quantum phase transition involving a superconducting system. One of the most significant difficulties of carrying

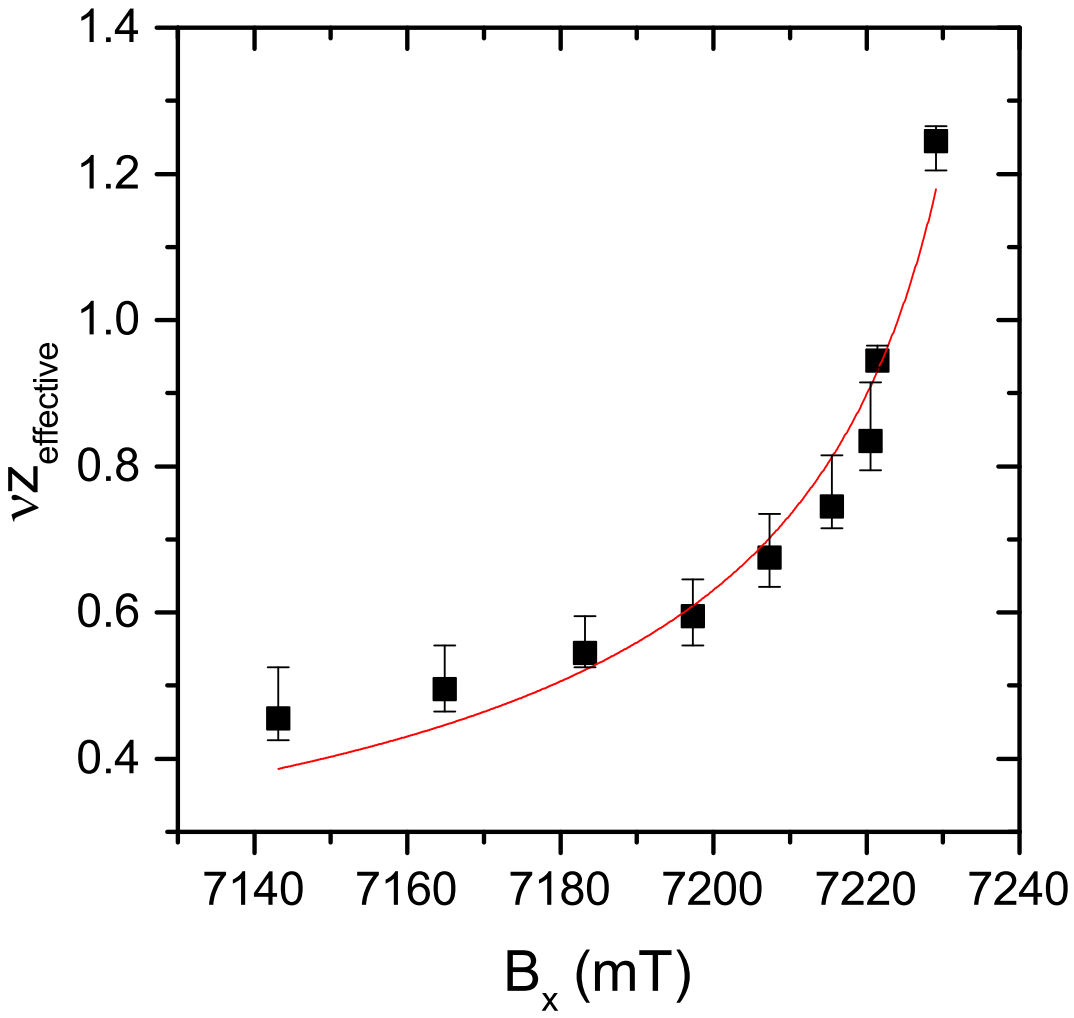

Figure 4.17: Effective exponent product, νz, as a function of crossing field, B_x, as found by the modified power-law scaling technique. This is for sample batch 15 chip 2. The solid line is a two-parameter fit of equation 4.7 to the data.

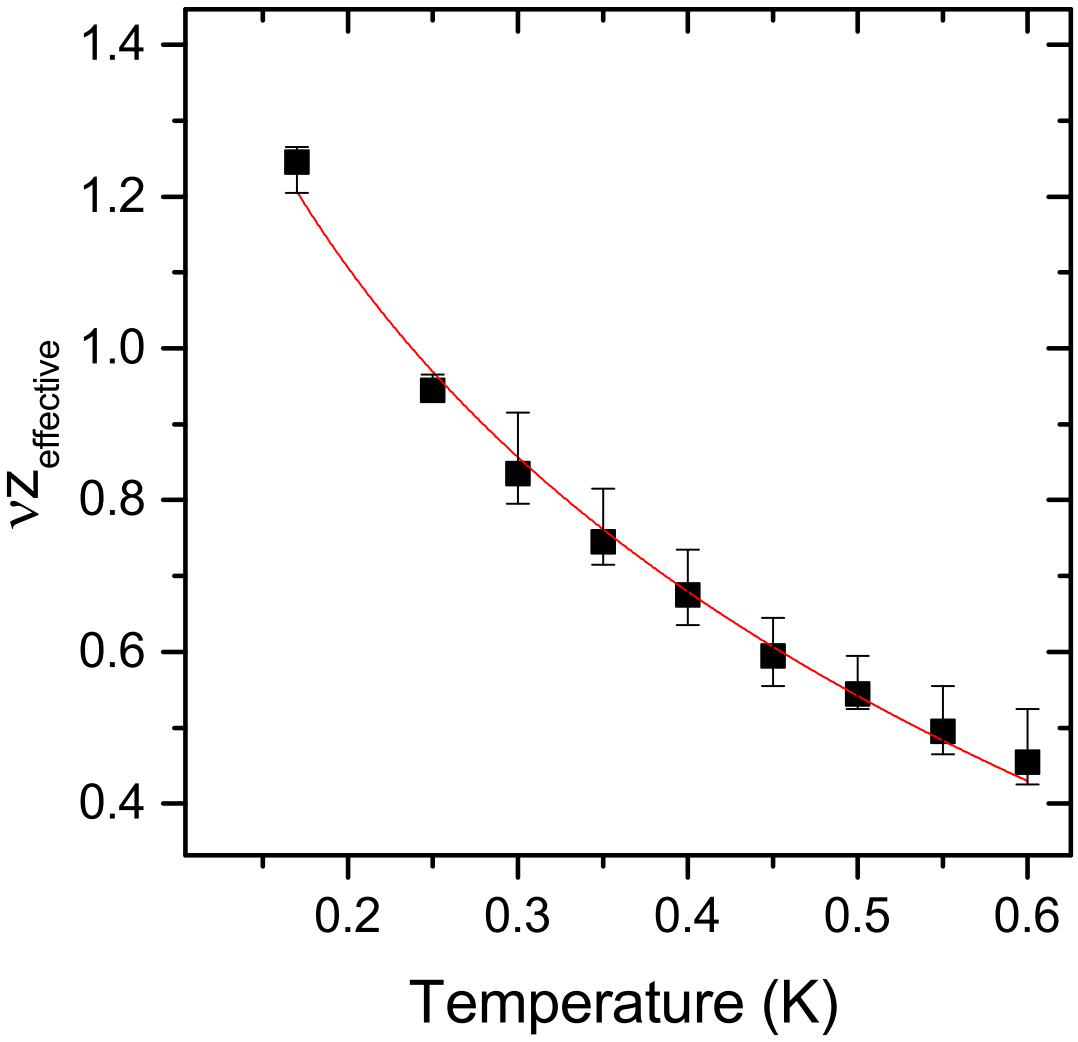

Figure 4.18: Effective exponent product, νz versus temperature for batch 15 chip 2. The solid line is a two-parameter fit to the data of equation 4.6.

out this analysis comes from the activated scaling form, equation 4.2, itself. Unlike the power-law scaling form, the activated scaling form has three free parameters. This in conjunction with the scaling function Φ being an unknown function makes it difficult to perform this analysis. Additionally, a three-parameter fit with no constraints on the parameters and no corroborating evidence is not very convincing. Given enough free parameters many functional forms that are not physically relevant could be fit to a data set.

One of the three free parameters was fairly straight forward to determine. Similar to the case for power-law scaling, the critical field B_c can be determined from the magnetoresistance isotherms. In the case of activated scaling, B_c was taken as the zero-temperature limit of the crossing field. An important step forward with activated scaling can be made by comparing equation 4.2 with equation 4.6. The two free parameters in equation 4.6 also appear in the activated scaling form, equation 4.2. This was an important improvement over determining the free parameters in the activated scaling form through trial and error alone.

With the free parameters in the activated scaling form roughly determined through the fit of equation 4.6 to the effective exponent product data and the crossing field versus temperature data, activated scaling was attempted. The activated scaling shown in figure 4.19 was restricted to temperatures of 600mK and below. This coincides with the region where $(\nu z)_{eff}$ follows the theoretically predicted forms of equations 4.6 and 4.7 and where the crossing field versus temperature is consistent with equation 4.9. Above this temperature the scaling breaks down. The reason for this will be explained in more detail later.

The parameters from the fit of equation 4.6 provided a good start to collapsing the data using activated scaling that was further refined employing a numerical method used by Skinner et. al. [58]. With this method, implemented in Matlab, the quality

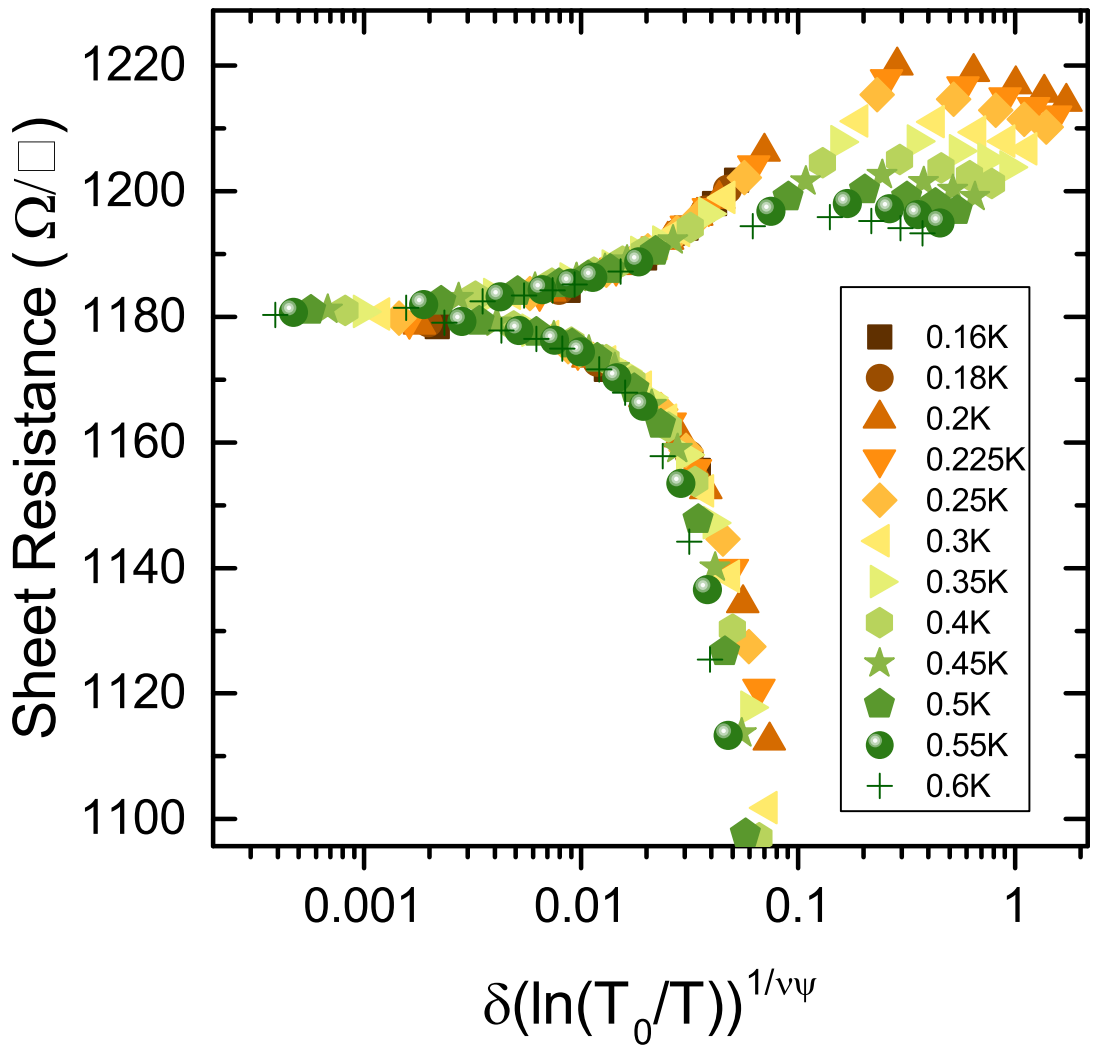

Figure 4.19: Sheet resistance versus the activated scaling parameter given in equation 4.2 for sample batch 15 chip 2. The data collapse around B_c=7.21 T, with $\nu\psi$=0.62 and T_0=1.21 K as determined from the fit in figure 4.18.

of the collapse was quantified. This was done by calculating the scaling parameter at each temperature for a given set of values for the free parameters, B_c, T_0, and $\nu\psi$. Then the resistance versus scaling parameter, x= $\delta(\ln(T_0/T))^{1/(\nu\psi)}$, was interpolated independently for each temperature so that each isotherm would be defined at the same discrete values, x_i, of the scaling parameter. Next the variance of the points corresponding to each temperature at a given value, x_i, of the scaling parameter was found and summed over all values of the scaling parameter over a restricted range near the quantum critical point,

$$V = \sum_{T,i} [R_T(x_i) - \bar{R_T}(x_i)]^2 \tag{4.8}$$

where $R_T(x_i)$ is the measured or interpolated resistance value for a given temperature, T, and value of the scaling parameter, x_i. The value $\bar{R_T}$ (x_i) is the resistance averaged over all temperatures at each value, x_i. This sum of variances, V, was used to quantify the quality of the collapse.

With this technique the quality of the collapse could be quantified for any given set of free parameters. The quality of collapse was then systematically checked for many different sets of values for the free parameters. The quality of the collapse as a function of $\nu\psi$ and T_0 was plotted, shown in figure 4.20. Lower values of this sum correspond to a better collapse.

Looking at figure 4.20, it is clear that the sum of the variances is not uniform over the range of $\nu\psi$ and T_0 values tested. However there also is not an obvious local or global minimum that was found. Instead there is an extended region where the variance is roughly minimized. This was verified by implementing a gradient decent algorithm within Matlab. For this technique the first step was to take the map of the variance as a function of T_0 and $\nu\psi$ and numerically calculate the gradient at each point. Next a random starting point was chosen. From this point a step in the direction

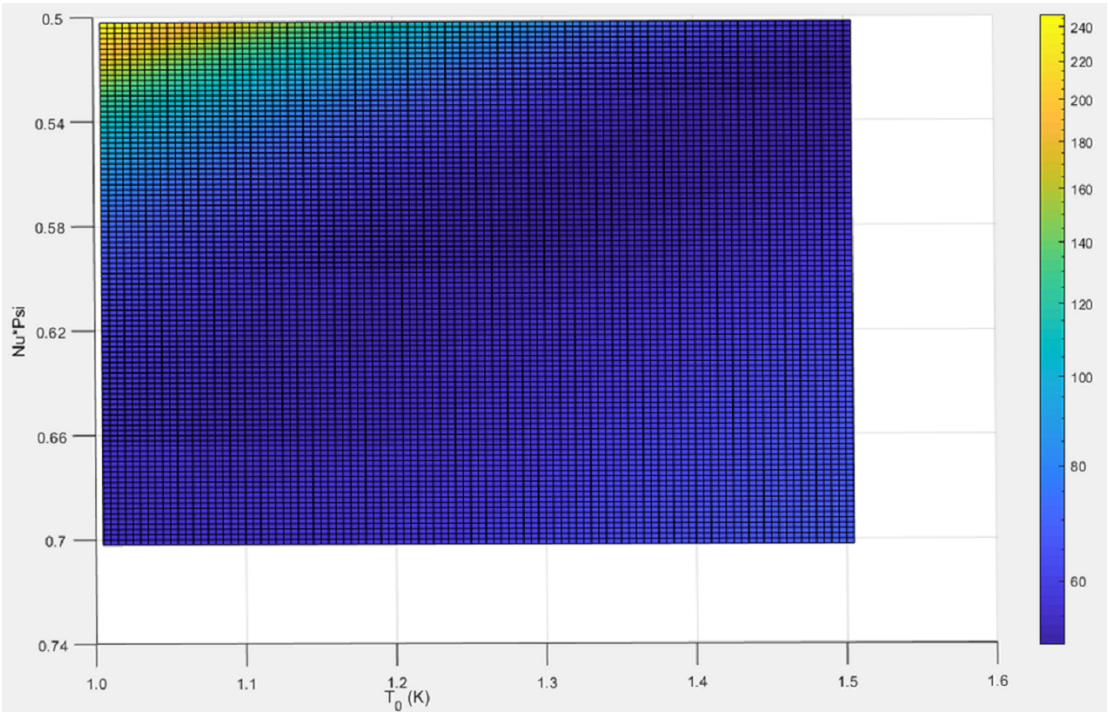

Figure 4.20: Contour plot of the quality of collapse of the scaled data as T_0 and $\nu\psi$ are varied and B_c is fixed. Smaller values indicate a better collapse.

of maximum decrease was taken. This was repeated for a preset large number of steps or until a minimum was found. This was repeated for different starting points with the goal of finding a consistent global minimum. However the minimum value found was consistently on the edge of the range of allowed $\nu\psi$ values.

An extended region of roughly minimal values with the global minimum on the edge was also found to be the case when the range of $\nu\psi$ and T_0 was extended. To reduce the chance that a minimum value was missed because it occurred between tested points, very fine steps of $\nu\psi$ and T_0 were used. 50,000 sets of values within the range shown in figure 4.20 were tested. Even though a set of $\nu\psi$ and T_0 values that definitively resulted in the best collapse was not able to be verified with this method, it did provide a useful consistency check. The set of values previously used did fall within the region of best collapse.

Examining figure 4.19, it is clear that a reasonable scaling collapse was achieved over a select range of temperatures and for magnetic field values in the vicinity of the quantum critical point. For magnetic field values beyond this range, which corresponds to larger values of the scaling parameter, the scaling starts to break down for both the upper and lower branches. For the upper branch this starts rather abruptly at 8T. The five disconnected regions correspond to magnetic fields of 8, 9, 10, 11, and 12T. This also corresponds to where the conductance becomes linear as a function of ln(T) (figure 4.11). This breakdown is believed to occur because the film is in a metallic state and not influenced by quantum fluctuations.

For the lower branch, which corresponds to smaller applied magnetic fields, the scaling breaks down more gradually, starting around 6.7T. The breakdown of scaling here is believed to be due to the film entering an ordered superconducting state at sufficiently low temperatures. In the superconducting state, like the metallic state, quantum fluctuations of the order parameter do not influence the properties of the

film. However, between these two extremes, near the quantum critical point, quantum fluctuations of the order parameter do affect the system leading to the scaling behavior.

4.9 Corrections

An additional complication that has not been taken into account in the analysis thus far is corrections to scaling. Corrections to scaling are caused by irrelevant variables. Taking corrections into account leads to taking on an effective value that is temperature dependent and has the following form,

$$\frac{1}{(\nu\psi)_{eff}} = \frac{1}{\nu\psi} - a\frac{\omega}{\psi} * [ln(T_0/T)]^{-\omega/\psi} \tag{4.9}$$

where a is a constant and ω is the exponent associated with the leading irrelevant variable, u. From equation 4.9 it is clear that in the limit of zero temperature $(\nu\psi)_{eff}$=$\nu\psi$. The scaling analysis is at sufficiently low temperatures that these corrections are negligible. The scaling analysis breaks down at higher temperatures because these corrections are no longer negligible.

These corrections also give rise to the shift in the crossing points that was observed by us and others. Without corrections to scaling there would be no temperature dependence to the crossings, B_x(T), shown in figure 4.16. This shift in the crossings, δ_x(T)=[B_c-B_x(T)]/B_c, takes the form

$$\delta_x(T) \sim u[ln(T_0/T)]^{(-1/\nu\psi)-(\omega/\psi)} \tag{4.10}$$

A fit of the data to this form is shown by the solid line in figure 4.16. The value of T_0 was fixed at T_0=1.21 K as was previously determined and u, B_c, and the exponent were left as free parameters. The best fit was achieved for u=-5.56X10^{-3}, p=2.40, where p is the exponent, and B_c=7.24±0.01T. This value of B_c is slightly higher than the value used for the scaling analysis, but is within 0.3%.

4.10 Conclusions

The smeared crossings and divergent exponent product, νz, observed in both samples batch 15 chip 2 and batch 15 chip 3 provide important evidence of the observation of the quantum Griffiths effect and an infinite-randomness fixed point at the transition. This is qualitatively similar to what has been previously observed by others [45, 46, 47, 48, 49, 50, 51, 52]. However, the analysis was taken several steps further than previously described in the literature, providing the strongest evidence yet of this effect. It is important to note that the smearing crossings, that were the first sign of the exotic behavior of these films, was caused by corrections to scaling. These corrections were not addressed and no other detailed explanation for the smearing was hypothesized in any of the other publications. Additionally, a theoretical prediction for the exponent product as a function of temperature was successfully fit to the data and using this, the data was scaled using activated scaling. This provides strong evidence for an infinite randomness fixed point, but it doesn't explain why it occurred.

As was discussed earlier in this chapter, quenched disorder plays a significant role in the properties of a phase transition. This is even more significant for the case of a quantum phase transition, such as the superconductor-metal transition that was observed in these samples. For amorphous indium oxide the disorder occurs at the atomic length scale and is caused by oxygen vacancies and variations in the interatomic spacing. The oxygen vacancies, between 5% and 30%, cause spatial variations in the carrier concentration. It is also possible that there is structural disorder in the form of extended defect states [59].

Both the disorder and carrier concentration play a role in the transport properties of the film. Increasing disorder causes the film to become more insulating and less metallic. Additionally, increasing the carrier concentration produces a film that is more metallic and less insulating. These variables cannot be independently tuned during deposition,

however after deposition the carrier concentration is relatively fixed and the disorder can be reduced. It is believed that the films studied here had their disorder reduced significantly through annealing at room temperature for several years.

The reduced disorder of these films contributed to their unusual behavior. Highly disordered indium oxide films typically undergo direct quantum superconductor-insulator transitions. Less disordered films have been shown to have broader transitions and in some cases superconductor-metal transitions. In this case, the less disordered films exhibited an infinite randomness fixed point. This is believed to have occurred due to the detailed nature of this disorder.

As was discussed earlier, the effect of disorder on a system depends on whether the Harris criterion was met and how the disorder behaves under coarse graining. For the case of the two dimensional magnetic field tuned superconductor-metal transition ν=1/2 and d=2, thus violating the Harris criterion, dν >2 [41]. Additionally, it has been shown that superconductor-metal transitions fall into the same universality class as the random transverse-field Ising model [37]. Vojta and Schmalian later showed that such a system when in the presence of Ohmic dissipation is exactly at its lower critical dimension [38]. Such a system is expected to exhibit the quantum Griffiths effect and have an infinite-randomness fixed point. This Ohmic dissipation in not present in indium oxide films that exhibit superconductor-insulator transitions instead. Correspondingly they typically follow power-law scaling as opposed to activated scaling.

Another important consideration is how the metallic background interacts with the rare, ordered regions, which in this case are superconducting puddles. In order for the slow dynamics that results in activated behavior to occur, the electrons that cause the dissipation need to penetrate the entire superconducting puddle. Spivak et al. [60, 61] pointed out that these electrons can only penetrate into the puddle as far as the superconducting coherence length. In the limit of large rare-region size, this

results in the dissipation scaling with the surface area rather than the volume of the puddle, cutting off the quantum Griffiths physics at the lowest temperatures. However this crossover temperature is expected to be extremely low because of the exponential dependence of the rare-region energy scale on its size. This leaves a wide temperature range governed by Griffiths physics.

In summary, these samples are believed to exhibit unusual behavior instead of a conventional quantum critical point because of their reduced disorder. Due to the reduced disorder, near the transition, rare regions form. These rare regions take the form of superconducting "puddles" immersed in a metallic background instead of an insulating background. The large ordered rare regions in the presence of Ohmic dissipation leads to the exhibition of the quantum Griffiths effect and an infinite-randomness fixed point.

Chapter 5

Low-Frequency Noise and Percolation Near the SIT

5.1 Introduction

In most experiments noise is unwanted and may obscure the signal of interest. Typically, much work must be done to minimize and avoid any sources of noise. However, in some cases the noise characteristics intrinsic to a material, device, or system can be insightful. This has led to the extensive study of noise in a wide variety of systems for decades. Noise has been studied in semiconducting materials and devices, materials exhibiting quantum phase transitions, graphene devices, granular superconductors to study vortex motion and self-organization, metallic films of Ag, Al, Au, Cr, Cu, Mo, Nb, Ni, Pt, and W, $LaAlO_3/SrTiO_3$ interfaces exhibiting BKT transitions, correlated fluctuations, and metal-insulator transitions [62, 63, 64, 65, 66, 67, 68, 69, 70, 71, 72].

In one such example, excessive noise was used as a test for many-body localization [73]. Low-frequency current noise was measured in amorphous indium oxide films that underwent a field-tuned SIT. When in or near the insulating regime, these films exhibited

a voltage threshold at which the current increased dramatically in a non-Ohmic way. It was found that a sharp peak in the noise occurred at this voltage threshold. This was taken as suggesting that a many-body localization transition governed low temperature transport in these films near the insulating state.

Another example of noise measurements being used to study a SIT is the work of Parendo et. al. [16]. They studied the thickness-tuned SIT of granular bismuth films. Low frequency voltage fluctuations were extensively studied as a function of temperature and film thickness. It was found that the noise was 1/f in the insulating state and white in the superconducting state. Between these two the slope changed gradually with no noteworthy features being found at the critical thickness. Additionally, frequency independent second spectra were found, indicating uncorrelated fluctuations as the source of the observed noise.

Other experiments studying resistance fluctuations have revealed evidence of correlated fluctuations. Raicevic et. al. studied resistance fluctuations in single crystal $La_{2-x}Sr_xCuO_4$ that was doped well into the spin glass phase [74]. They found that the fluctuations exhibited 1/f like noise, however, the value of the exponent in the temperature dependence of the resistance, corresponding to the slope on a log-log plot, decreased as the temperature was increased, until the noise was nearly white above 0.2K. Histograms and second spectra at various temperatures and applied magnetic fields indicated strong temperature dependence, but no field dependence. At low temperatures, below 0.2K, these measurements exhibited correlated fluctuations and suggested a transition to a charge glass state at zero temperature.

The original motivation for pursuing the measurement of noise near the SIT exhibited by indium oxide was to gain a better understanding of the transition. The idea was to use the noise measurements as a tool to determine if Cooper pairs persisted into the

non-superconducting regime. Green et. al [75] had predicted that the noise characteristics of a bosonic metal would differ significantly from those of an ordinary metal in that it would exhibit Johnson noise like behavior with an elevated effective temperature that scaled as $\sqrt{E}$, where E is the electric field across the sample. In practice this difference in noise properties proved too subtle to be detectable over the background noise and was not pursued further.

Support for the idea that low frequency noise studies near the SIT could be valuable was provided by the work of Chen and Yu [76] involving Monte Carlo simulations of the Ising and 5-state Potts models in two dimensions. These models undergo second and first order phase transitions, respectively, as a function of temperature. The goal of these simulations was to determine the outcome of competing effects near the transition, specifically, the growth in intensity of fluctuations near the transition against a reduction in noise due to self-averaging. They found that for both models the low-frequency noise and total noise power increased as the phase transition was approached. While this study was focused on classical phase transitions, it is not a stretch to imagine similar effects occurring near a quantum critical point since classical and quantum phase transitions can often belong to the same universality class.

As described in the introduction, fluctuation phenomena are crucial features of quantum phase transitions since quantum fluctuations persist to zero temperature and thermal fluctuations do not. Kremen et. al. [77] were the first to locally image quantum fluctuations. They studied the thickness tuned SIT in NbTiN films. Using a scanning superconducting quantum interference device, they were able to image fluctuations in the diamagnetic response of the films, both as a function of position and time. The diamagnetic response provided a measure of the local strength of superconductivity. They found that the fluctuations grew in lateral dimension as the critical point was approached, which is consistent with theoretical expectations. Additionally, it was found

that instead of a diverging characteristic time, a wide range of characteristic times were observed. Based on these observations of fluctuations in superconducting strength, it was only natural to further pursue the study of resistance fluctuations in the vicinity of the SIT.

The measurement of resistance fluctuations is not a direct measurement of the superconducting strength, but it is expected to be influenced by these quantum fluctuations. Quantum fluctuations are known to influence the global properties of films, such as the sheet resistance. This is used in scaling analyses of SITs to analyze resistance measurements made at nonzero temperature despite the transition occurring at zero temperature. Since these quantum fluctuations can influence the time averaged resistance of films, it is reasonable to believe they might influence the time dependent fluctuations of the resistance.

As will be described in detail later in this chapter, low frequency resistance fluctuations of an indium oxide thin film undergoing a field-tuned SIT were measured. These resistance fluctuations are believed to be due to the random switching of the Josephson coupling between grains in the film. This chapter will first describe the various types of noise commonly observed in physical systems, and then briefly treat percolation. This will be followed by a presentation of the data and the analysis of resistance fluctuations. Finally, the connections that can be made between the measured noise characteristics and the percolation model will be presented.

5.2 Types of Noise

It is useful to describe some commonly observed types of noise to provide a better understanding of what to look for when characterizing noise, trying to avoid external noise, and estimating the noise floor of the measurement system. A ubiquitous type of noise present in conductors and semiconductors is thermal noise, or Johnson noise.

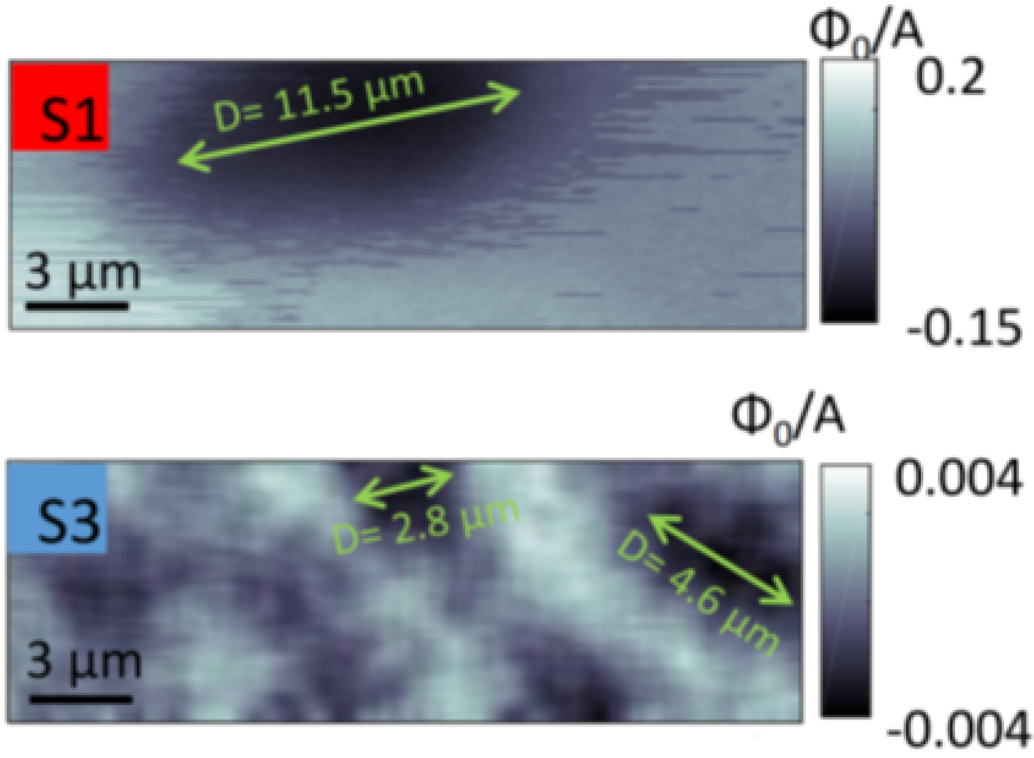

Figure 5.1: The upper and lower plots are maps of the diamagnetic response of two thin films. This corresponds to the superconducting strength and was measured using a scanning SQUID. The upper and lower plots correspond to two different samples, with S1 being closer to the quantum critical point than S3 [77].

Johnson noise is the random fluctuation of the voltage across a resistor [78]. The rms value of this fluctuating voltage is:

$$V_{rms} = \sqrt{4Rk_BT\Delta f} \tag{5.1}$$

where Δf is the bandwidth over which the voltage is measured, R is the resistance, k_B is Boltzmann's constant, and T is the temperature. This noise is called white noise because it is independent of frequency. It is caused by thermal fluctuations which affect the charge carriers in the circuit. As a consequence of the equipartition law of statistical physics; it can be shown that the expected voltage noise takes the form of Eq. (1).

A second type of noise is shot noise. Shot noise is caused by the quantization of the charge carriers in a circuit [78]. Any time a charge carrier passes by, there is a pulse in the measured current. The sum of these random pulses results in the total current and the noise present in the measured current. It can be shown that this noise takes the form:

$$I_{rms} = \sqrt{2eI_{avg}\Delta f} \tag{5.2}$$

The third common type of noise is 1/f noise, also known as pink noise. 1/f noise is noteworthy because of how common it is. This type of noise has been observed in many electronic systems and even macroscopic physical systems such as the ebb and flow of the Nile River [79]. While there are many theories for the cause of 1/f noise in various systems, there is no universally accepted theory covering all examples. This is still an area of ongoing research. The resistance fluctuations of a wide array of conductive materials have normalized power spectra that follow this form.

As the name suggests, the power spectrum found when this noise is present takes the form:

$$S \sim f^{-\gamma} \tag{5.3}$$

Here $\gamma \approx 1$, but other powers are found, depending upon the underlying mechanism.

While the power-law relation is the defining characteristic of 1/f noise, it is not the only useful parameter for describing it. The Hooge parameter is a dimensionless quantity describing the magnitude of the 1/f noise of resistance fluctuations [80]. It is given by;

$$S_v/V^2 = \alpha/(f^\gamma \Omega) \tag{5.4}$$

where α is the Hooge parameter and Ω is the number of atoms in the sample, or sometimes is taken as the volume. This value is typically on the order of 10^{-3}-10^{-2} for ordinary metals, but can be higher for disordered materials.

5.3 Percolation

Percolation theory originated as the mathematical description of liquid flowing through a random maze. The term "percolation" was coined by Broadbent and Hammersley in 1957 [81]. Percolation differs from diffusion in that it pertains to models in which the randomness is applied to the medium instead of the fluid itself. These types of models can be extremely useful for characterizing the conductivity of various systems. The electrons can take the place of the fluid and a disordered atomic lattice takes the place of the random maze.

There are three main categories of percolation problems, lattice problems, continuum problems, and random site problems [82]. The lattice problem is the simplest and most relevant to the random resistor network and Josephson junction array models discussed later in this chapter and therefore will be the primary focus going forward. The lattice problem starts with a two or three dimensional lattice with bonds between all adjacent sites. Bonds allow liquid to flow in both directions and to any connected sites. These bonds can be either blocked or unblocked and their distribution is random. Many properties of the system can be described in terms of the fraction of bonds that are unblocked.

If liquid is sourced at a random site in an infinite lattice the liquid will be able to flow to all connected sites forming a cluster. This cluster can be either finite in size or infinite depending on the fraction of unblocked bonds. Below some critical fraction there are disconnected clusters of finite size throughout the lattice. Above this critical fraction there are enough connections that a cluster of infinite size is formed allowing liquid to flow throughout the lattice instead of being localized around where it is sourced. Additionally, it can be shown that there is a characteristic length,

$$L(x) = |x - x_c|^{-\nu} \tag{5.5}$$

where x is the fraction of unblocked bonds, x_c is the critical fraction, and ν is a critical exponent. In two dimensions ν=4/3 and in three dimensions ν=0.89±0.01. Taking unblocked bonds to represent resistors, the total resistance of a random resistor network can be written in terms of the fraction of unblocked bonds.

Quantum percolation is a modification to the classical percolation model just described. The modification considers the fact that electrons are a quantum particle and have wavelike properties [83]. Due to the wavelike properties, it is possible for interference effects to affect conduction along the various paths. Some paths may conduct less than they would be expected to classically because of this interference. This reduces the overall conductance of the system and effects the critical fraction of bonds. It also changes the scaling properties of the system [84].

5.4 The Perpendicular Magnetic-Field-Tuned SIT

The amorphous indium oxide films studied in this work were very similar to the films discussed in the previous chapter. They were deposited onto pre-patterned SiO_2/Si wafers. These wafers were cut from a single thermal oxide wafer. The polished SiO_2 layer was 300nm thick. The Si (100) wafer was 0.525mm thick and boron doped, p-type.

Its nominal resistivity was 1-20 Ω*cm. The patterning was done using the previously described photolithography technique and included two different geometries for the indium oxide layer and the corresponding electrical leads. These two geometries, shown in figure 5.2, are a Hall bar configuration and a special configuration used for the noise measurements that will be described in more detail later in this chapter.

The amorphous indium oxide films were approximately 30nm thick. They were grown in a similar manner to the films studied in the previous chapter. Several sets of four co-deposited indium oxide films were grown, each with a different oxygen partial pressure during deposition. This was done to tune the properties of the film, specifically the disorder and carrier concentration. Using this tuning ability, films that exhibited a superconductor-insulator transition could be grown. After deposition, the disorder was further reduced by annealing under vacuum to fine tune the critical field of the transition. This was done to ensure the critical field for the SIT was sufficiently low that the insulating side of the transition could be adequately studied with the magnetic fields accessible with the PPMS and the Oxford Kelvinox 400 (K400) dilution refrigerator.

The initial characterization and annealing of the films were done in the ^{3}He insert of the PPMS. This was done because the PPMS allowed for the samples to be annealed under vacuum and subsequently measured at low temperature without exposing them to atmosphere and much quicker than would be possible with the K400. The films from deposition InOx_061520_1, as initially deposited, were insulating in zero applied magnetic field. However, after two hours of annealing at 40℃ followed by another two hours annealing at 50℃, the sample appeared to exhibit a SIT. Looking at figure 5.3, the perpendicular critical magnetic field was between 0 and 3T. Additionally, there was evidence of a magnetoresistance peak occurring somewhere between 3 and 9T. The zero-field transition temperature was approximately 0.97K.

These measurements were restricted to a minimum temperature of 500mK due to

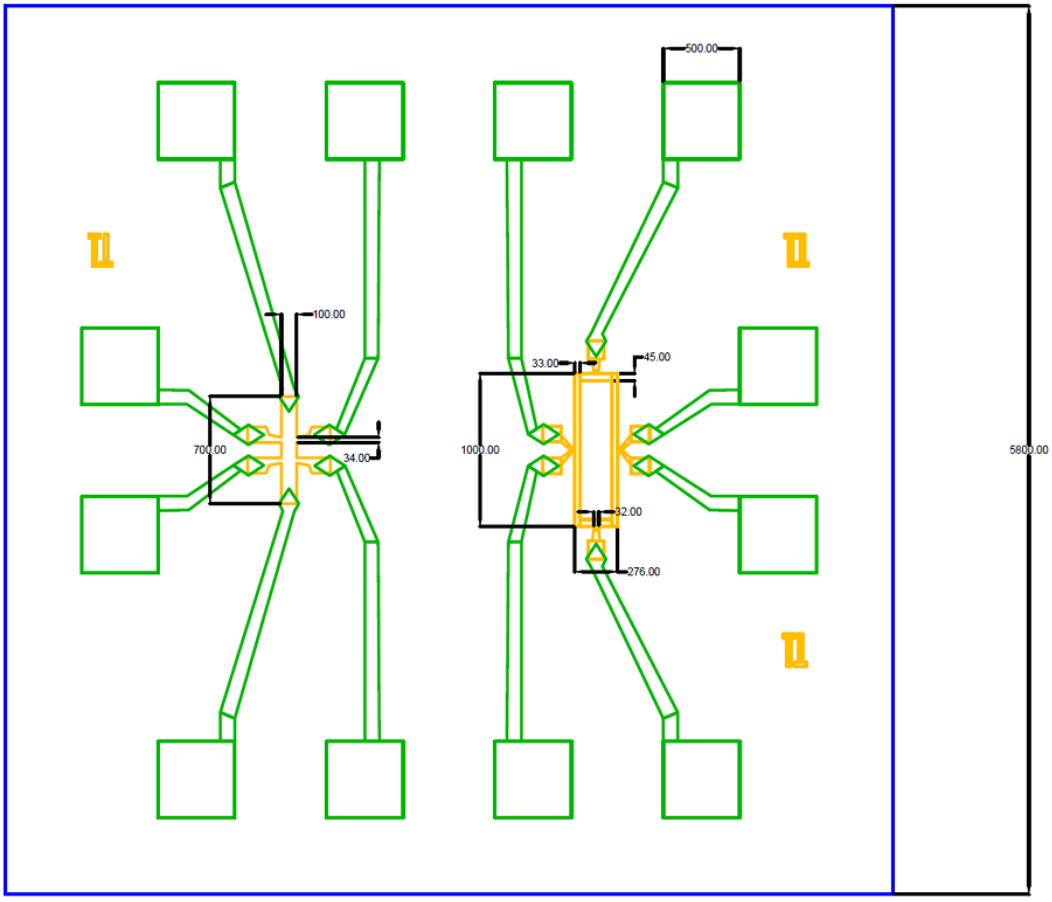

Figure 5.2: Scale diagram of the indium oxide samples used for these studies. On the left is the Hall bar configuration and on the right is the noise measurement geometry, both outlined in lighter lines. Outlined in darker lines is the Ti/Au contact layer. All units are in micrometers.

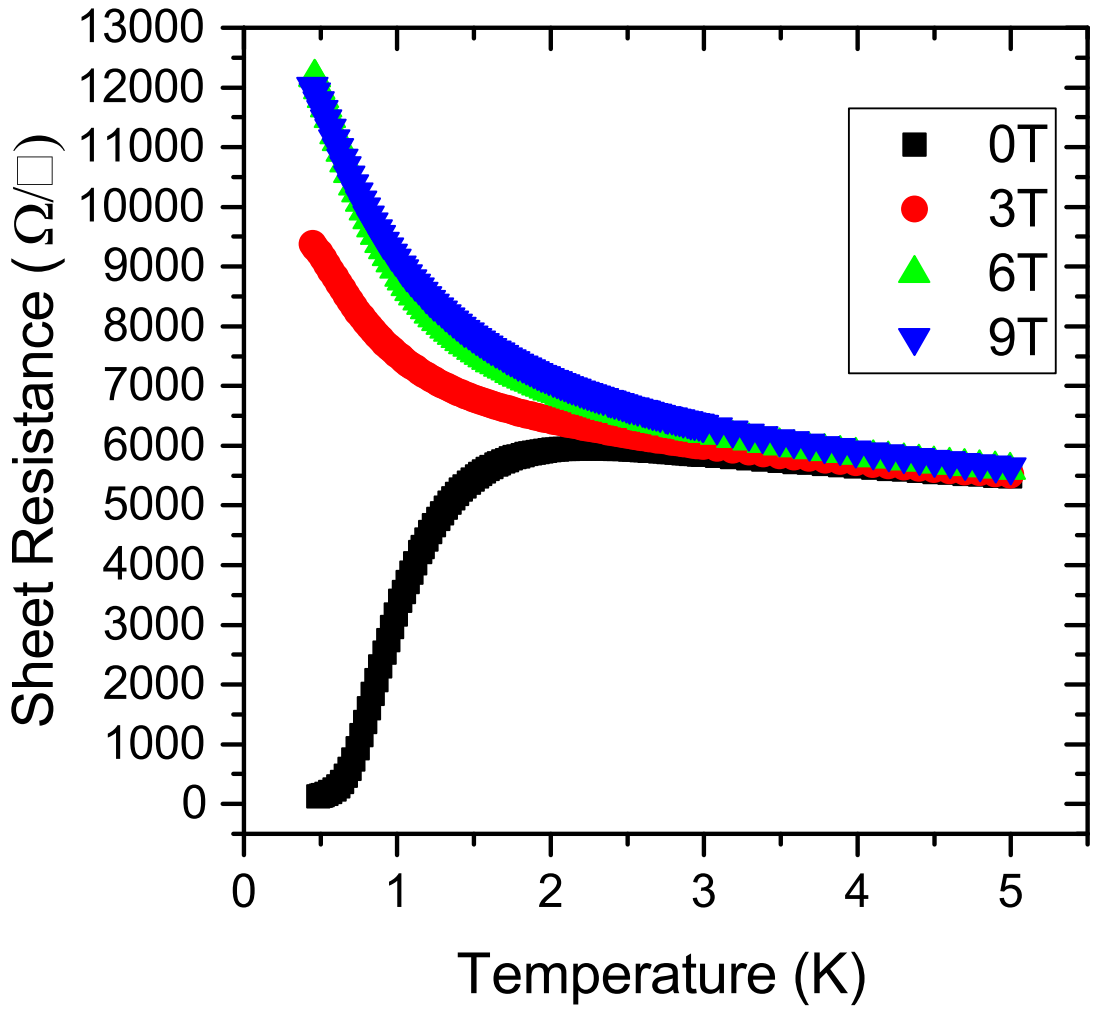

Figure 5.3: Plot of the sheet resistance vs. temperature of sample InOx_061520_1 after 4 hours of annealing under vacuum at a maximum temperature of 50°C under various applied perpendicular magnetic fields.

limitations of the ^{3}He insert of the PPMS. The resistance measurements were made using the Hall bar configuration device on the wafer. A constant current of 200 nA DC was sourced along the length of the bar using a Keithley 6221 current source. The voltage drop was measured across the inner two contacts using a Keithley 2182 nanovoltmeter. This four contact measurement configuration eliminated contact and lead resistance from the measured value. The 200nA measurement current was chosen based on voltage versus current sweeps. It was chosen to be in the linear regime of this sweep and to optimize the tradeoff between signal-to-noise ratio and Joule heating.

It was concluded that films from this batch were worth studying in further detail and to lower temperatures. The K400 was used for this because it could cool samples to ∼100mK instead of the ∼500mK lower limit with the PPMS. Also, the K400 has better electrical filtering, allowing sufficient signal-to-noise ratio to be maintained with a lower bias current and subsequently, less Joule heating. Sample InOx_061520_2, which was co-deposited with InOx_061520_1 and subjected to the same annealing treatment, was chosen to be measured in the K400. A different sample was chosen because of the difficulty of wire bonding between the electrical leads of the K400 sample holder and sample InOx_061520_1 after it had been previously wire-bonded and studied with the PPMS. It was best to start with a sample that had no contact pad damage from previous wire-bonding.

Sample InOx_061520_2 was able to be measured in much more detail in the K400. These measurements were made in a similar manner to the measurements in the PPMS. A DC measurement was made by sourcing a constant current along the Hall bar device and measuring the voltage using separate contacts. The measured voltage was taken as the average of 60 separate readings. The same model Keithley instruments were used. Because of the lower electrical noise level in the K400 compared to that of the PPMS, the measurement current could be significantly lower. A 10nA current, instead of a

200nA current was able to provide a similar signal-to-noise ratio. The signal-to-noise ratio varied from ∼150 at the lowest resistance values to over 10,000 at the highest.

The sheet resistance was not found using the van der Pauw method in this case. The sample geometry was not convenient for this technique. Instead, it was estimated using geometric consideration. Looking at the Hall bar device in figure 5.2, the distance along the length of the bar between the midpoints of the two voltage contacts is ∼1.34 times the width of the bar. Therefore, it was estimated that the measured resistance corresponded to 1.340 squares. The validity of this approximation was verified to a high degree of accuracy using numerical methods.

Laplace's equation in two dimensions was solved for the Hall bar device geometry using the built in PDE solver in Matlab and setting the appropriate boundary conditions. The solution is shown graphically in figure 5.4. The effective number of squares measured by the finite width voltage probes was estimated to be ∼1.327 squares. This agreed with the geometric estimate to within 1%.

The sample temperature was taken to be the average of the temperatures measured just before sourcing a current and just after. Additionally, to ensure the sample was in thermal equilibrium, there was a five-minute wait after reaching the set point temperature before sourcing any current. There was also a 30 second wait after starting to source the current before the voltage measurement was started. This was done to eliminate artifacts due to the electrical filtering present in the measurement circuit. Just as was done with the PPMS, the resistance measurement was repeated with the current sourced in the opposite direction and the average was taken. This eliminated any thermoelectric effects from skewing the measurement.

With the K400, the lowest temperature at which the sample could be reliably measured was 100mK. Below this temperature the R(T) curves all flattened regardless of the field, indicating a failure to cool the film. Based on voltage versus current sweeps

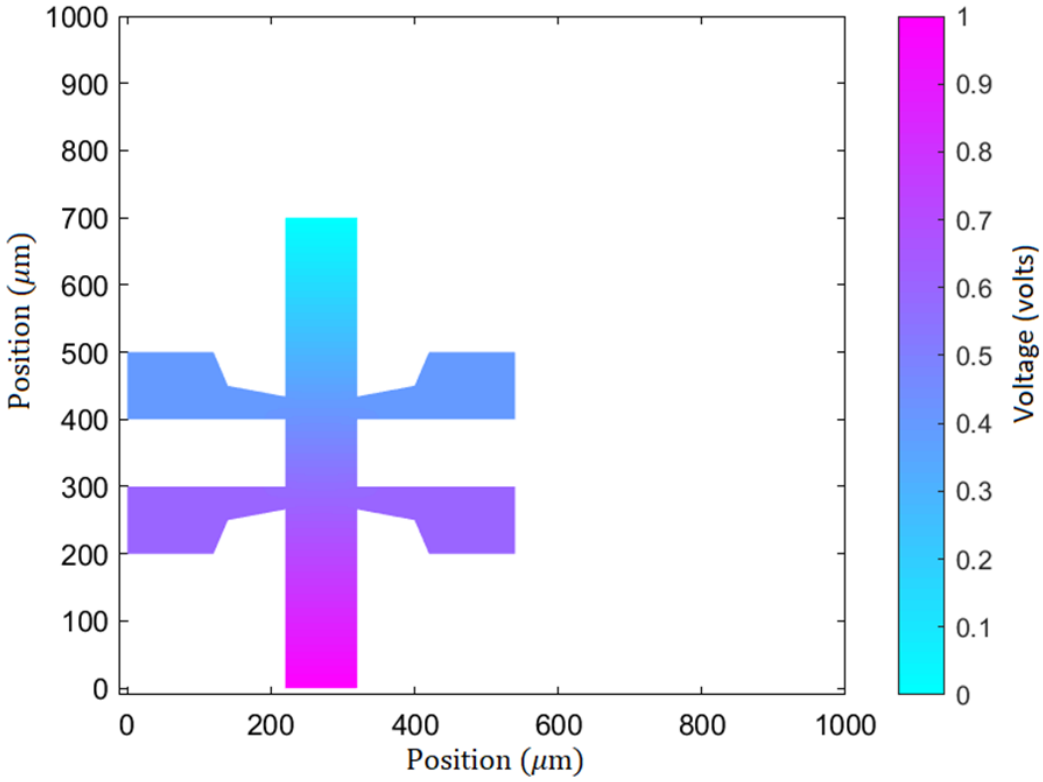

Figure 5.4: Numerical solution to Laplace's equation on the Hall bar device. The boundary conditions are such that there is no net charge on any boundaries except the two ends of the bar, which are held at 1 volt, and the other at ground.

and the long wait times used, this failure to cool below 100mK is believed to be due to a combination of external radiation, thermal radiation, and imperfect thermal contact between the sample holder and the mixing chamber of the dilution refrigerator.

From figure 5.5, it can be seen that this film behaves in a manner similar to InOx_061520_1. At the lowest temperatures the sheet resistance drops to within the noise level of zero resistance and is superconducting. When a magnetic field of 4T is reached, the resistance appears to be diverging as the temperature is reduced, indicating insulating behavior. At the lowest temperatures there is a magnetoresistance peak around 6T. The change from dR/dT being positive at low fields to negative at high fields happens around 2.5T, which is consistent with what was previously observed with the other sample.

This insulating behavior was verified by comparing the temperature dependence of the resistance to various hopping models. It was found that Efros–Shklovskii variable-range hopping [85] provided the best fit to the data. From figure 5.6, it is clear that by 6T this model fits quite well. This provides strong evidence of an insulating state occurring with large applied magnetic fields.

Using the data from the resistance versus temperature sweeps, a series of resistance versus magnetic field isotherms were generated. This was done in the same way that was described in the previous chapter. From figure 5.7, it is clear that the superconducting behavior is suppressed as the applied perpendicular magnetic field is increased. The isotherms peak around 6T, with this being more pronounced at lower temperatures. This would be consistent with what was observed in the co-deposited sample measured in the PPMS.

Additionally, these isotherms cross at a single point. Looking at the crossing in more detail reveals no systematic change of the crossing point at a function of temperature. This is entirely consistent with what is typically observed for systems believed

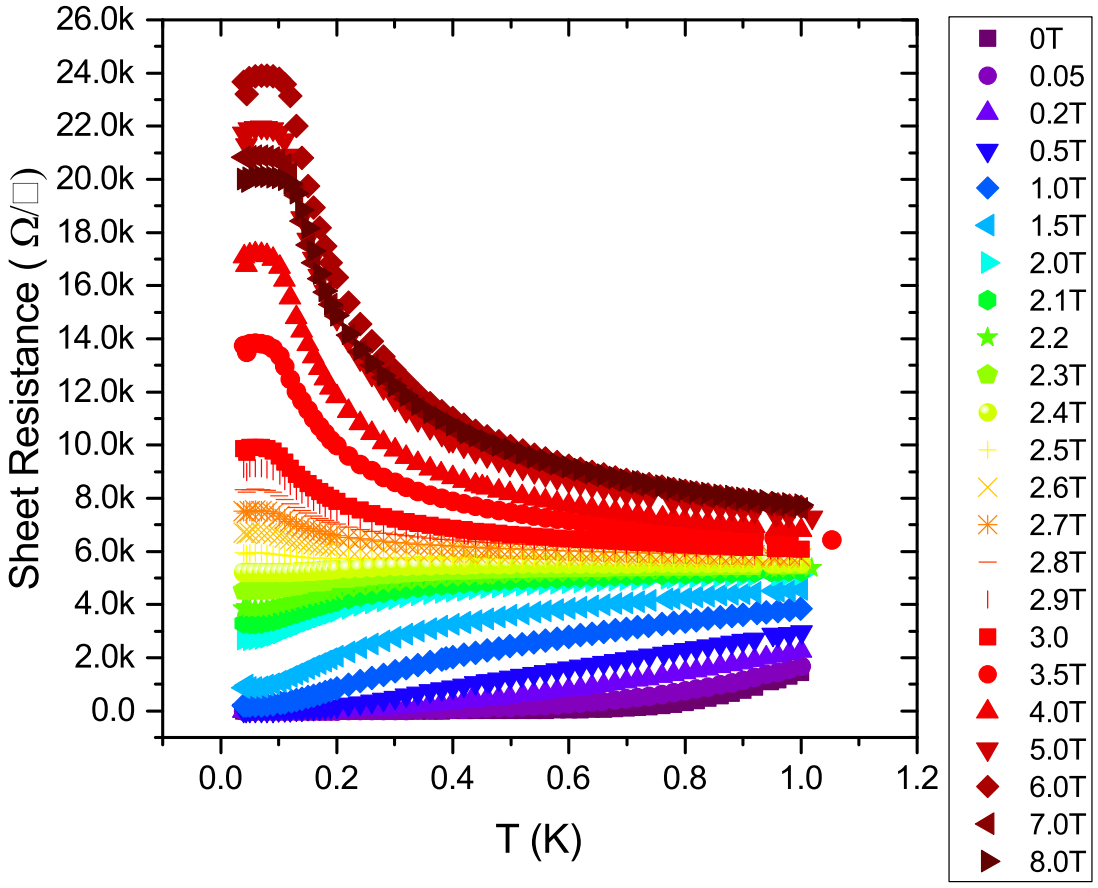

Figure 5.5: Plot of the sheet resistance vs. temperature of sample InOx_061520_2 measured in the K400 with various applied perpendicular magnetic fields. At low temperatures and fields it is superconducting and at high fields it is insulating.

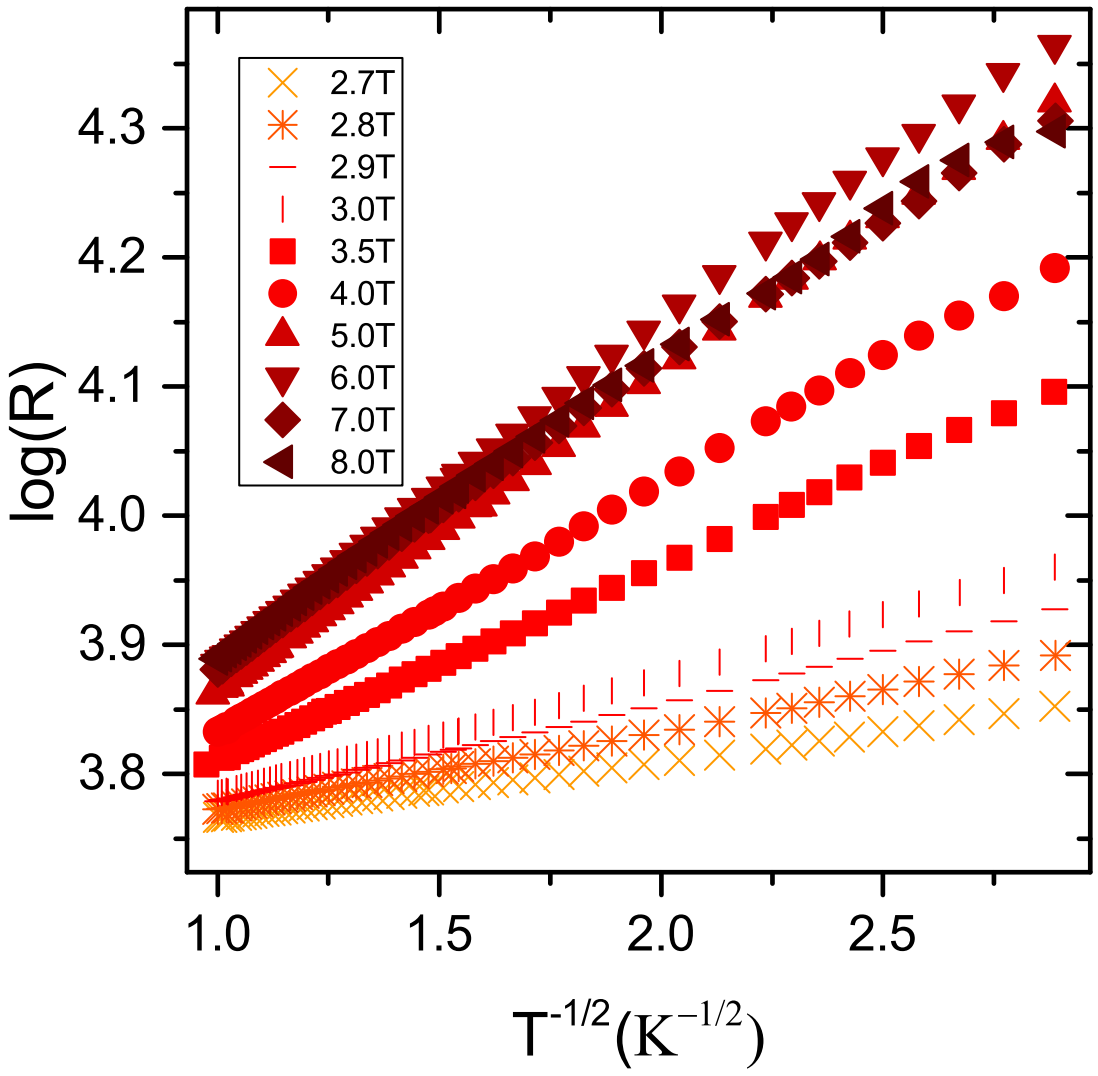

Figure 5.6: Plot of the logarithm of the sheet resistance versus $T^{-1/2}$ for sample InOx_061520_2 with various applied perpendicular magnetic fields. This is clear evidence of hopping conduction.

to undergo superconductor-insulator transitions [17, 86, 87]. A caveat is there is always the possibility of other physics coming into play at temperatures below the range of temperatures traversed in measurements. Apart from this, it is natural to attempt a power-law scaling analysis of the data.

As is typical, the scaling analysis was begun by identifying the critical magnetic field. At the critical field the scaling function is independent of temperature and therefore the resistance is expected to be temperature independent. This point appears as a crossing point in the plots of the isotherms. In the case of this film, the critical point was estimated to be 2.486T using an interpolation between the measured data points. With this value set, the exponent product νz could be found numerically using a Matlab script.

This script used a guess and check algorithm very similar to that described in the previous chapter for the activated scaling fit. It was found that νz=1.25$\pm$0.04 resulted in the best collapse of the data, shown in figure 5.8. This value of νz is similar to what has been previously observed in indium oxide samples exhibiting a SIT [17]. Additionally, with the dynamical critical exponent taken to be z=1 [88, 89], the correlation length exponent, ν=1.25$\pm$0.04, is relatively close to the theoretically predicted value of ν=4/3 for the classical percolation model in two dimensions [90].

Similar results have been found for field-tuned transitions by many research groups and it is consistent with observations made by Steiner et. al. [84]. They found that systems undergoing a SIT, including amorphous indium oxide, could fall toward one of two limiting cases. In the limit of high disorder, systems exhibited a strong magnetoresistance peak, had a low value for the critical magnetic field, and scaled best with νz$\approx$7/3, consistent with quantum percolation. In the low disorder limit, systems exhibited a weak magnetoresistance peak, had a high value for the critical magnetic field, and scaled best with νz$\approx$4/3, consistent with classical percolation. Based on the moderately

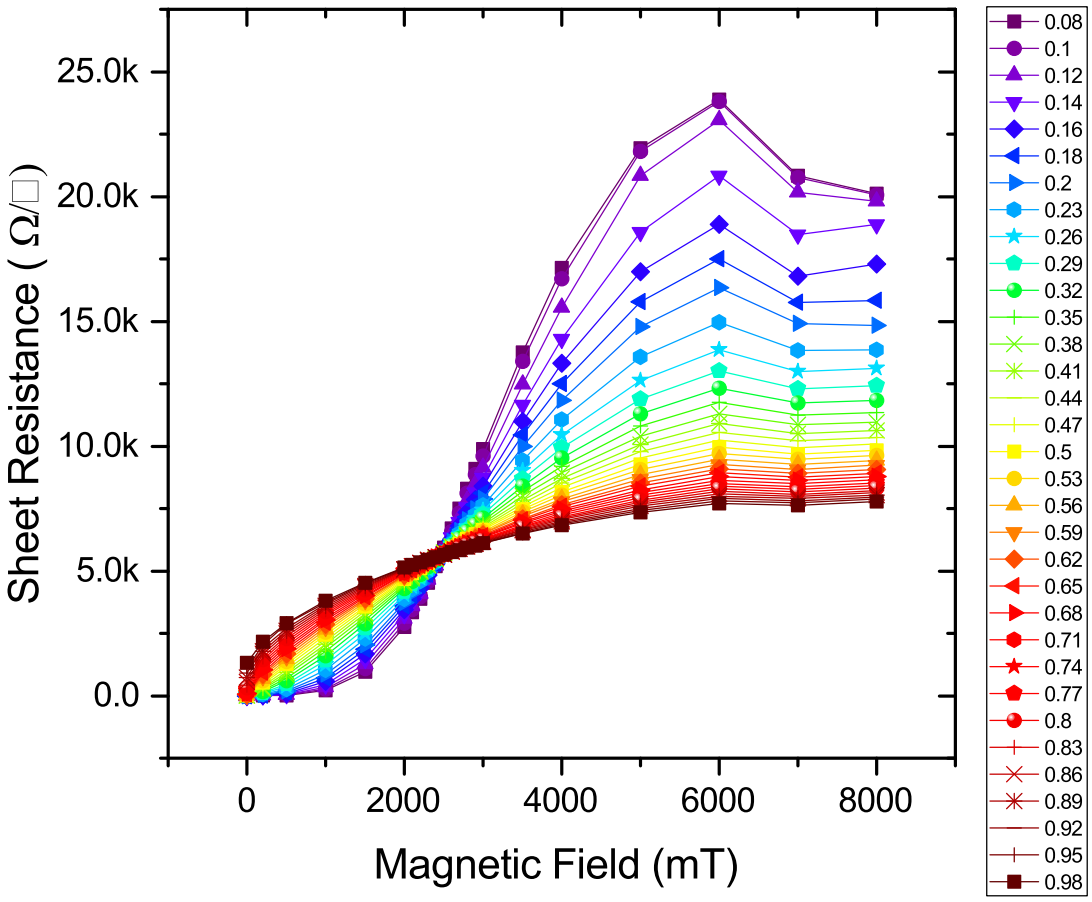

Figure 5.7: Plot of the magnetoresistance isotherms generated from the resistance versus temperature curves. The temperature in Kelvin is indicated on the right. There is a clear crossing of the curves at ∼2.5T with a resistance of ∼5.7kΩ. At ∼6T there is a peak in the isotherms that is more prominent at lower temperatures.

high critical field, weak magnetoresistance peak, and νz value, the film characterized in this chapter falls closer to the low disorder limit.

5.5 Scofield Noise Measurement Technique

One of the biggest issues when trying to measure the electronic noise intrinsic to a particular device or sample is to distinguish intrinsic noise from any external contributions. The external sources of electronic noise can include the measurement electronics themselves. Pre-amplifiers are a common source of 1/f noise in measurements. Other external sources of noise could be caused by ground loops, as was discussed in detail earlier, temperature fluctuations, inductive pick-up, etc. An important technique for dealing with background noise while measuring low frequency resistance fluctuations was developed by John Scofield [91]. This technique was so vital to the noise measurements described later in this chapter that it warrants detailed explanation. This technique has been commonly used in resistance fluctuation studies carried out by various research groups [92, 74, 93].

The simplest way to measure resistance fluctuations is to use a four-probe configuration as is commonly used to make resistance measurements. To do this, a power supply of voltage E_0 is connected in series with two ballast resistors of resistance R1 and R2, and the sample, as shown in figure 5.9. Provided that the resistance of each ballast resistor is large compared to the sample resistance, the sample resistance will be negligible, and the current will be $I \sim E_0/(R1+R2)$. The other two contacts on the sample are used to measure the voltage. The fluctuations can be measured by blocking the average voltage with a capacitor and amplifying and measuring the resulting signal. In this arrangement fluctuations due to the contact resistance are minimized by choosing ballast resistors that are large compared to the contact resistance.

This method has several limitations. One problem is that fluctuations of the output

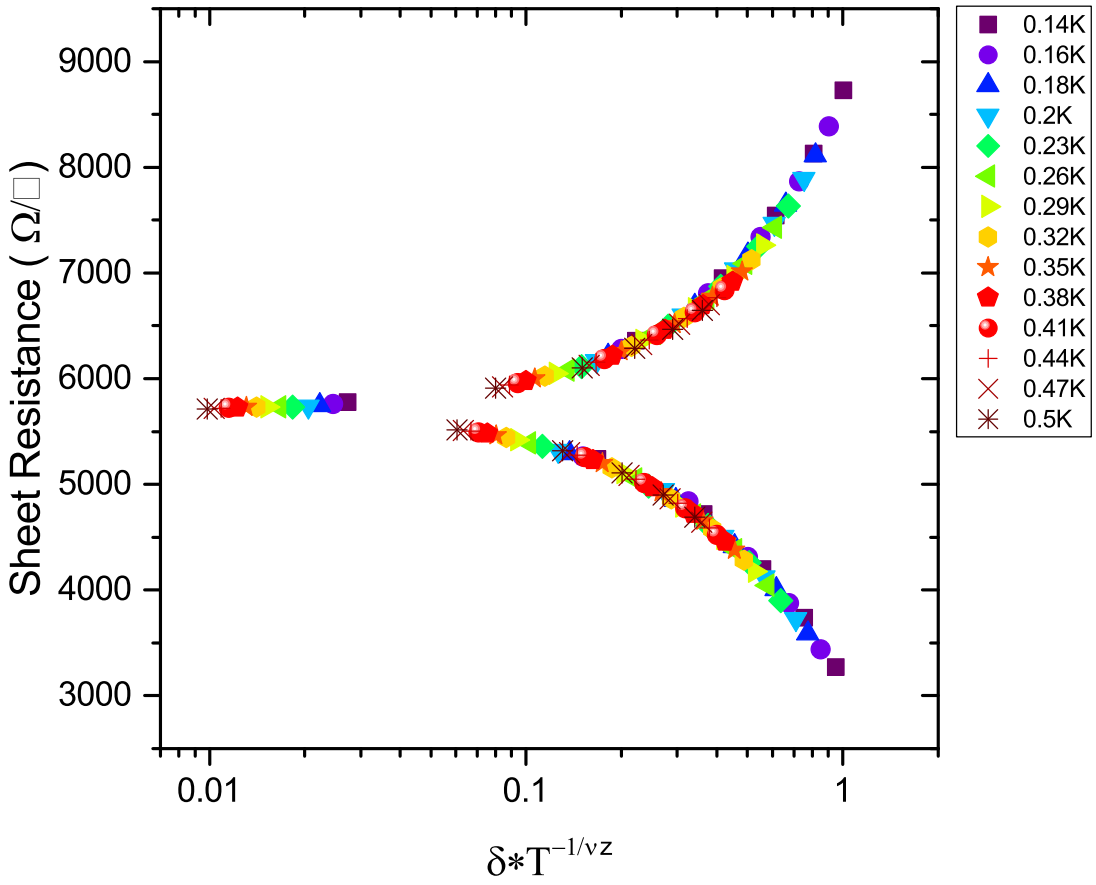

Figure 5.8: Sheet resistance versus the scaling parameter, given in equation 1.3, for InOx_061520_2. It was found that νz=1.25±0.04 resulted in the best collapse.

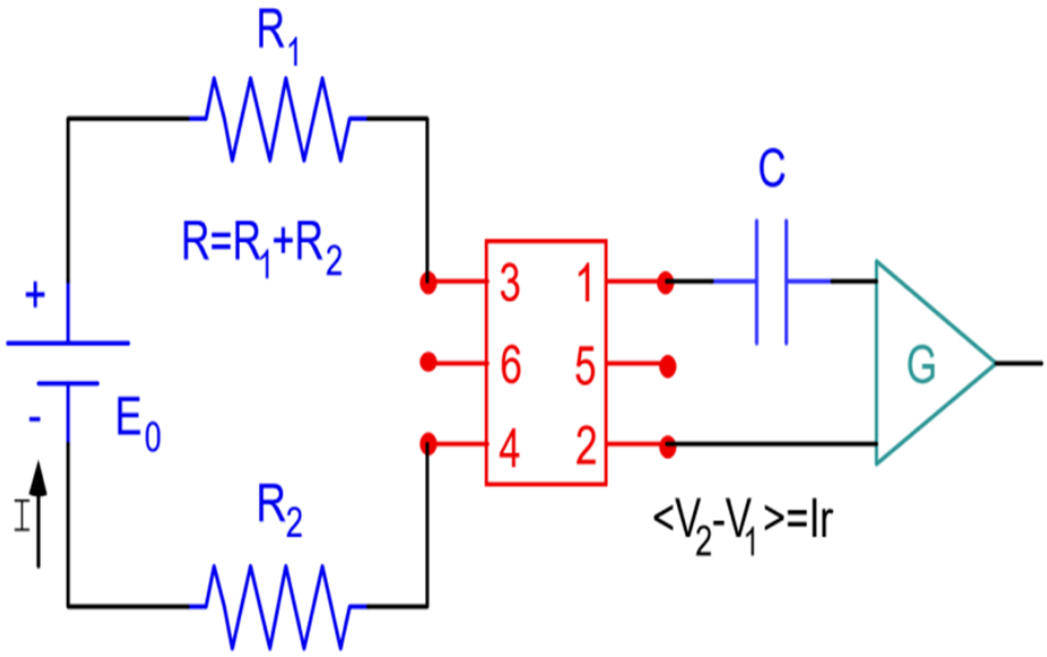

Figure 5.9: Circuit diagram for simple resistance fluctuation measurement circuit [91].

of the battery or power supply will be measured as noise from the sample. Another problem is that at low frequencies any preamplifier used will contribute a large 1/f noise signal that will often be larger than the signal from the sample itself. Also, the capacitor blocking the average voltage will impose a lower limit on the frequency of the noise that can be measured. Lastly, noise due to temperature fluctuations and fluctuations of other external conditions will be present.

Some of these limitations can be overcome through the use of a bridge. Placing the sample in a Wheatstone bridge eliminates the need for an average voltage blocking capacitor, thus allowing lower frequency measurements. It will also remove any fluctuations of the power supply or battery from the measured signal. When used in a five-contact configuration, as shown in Fig. 9, the input impedance and thus the background will be no larger than with the four-probe measurement. These advantages are possible because the bridge can be balanced by adjusting R1 and R2. However, there will still be significant preamplifier noise at low frequencies. Moving the measurement to higher frequencies can mitigate this problem.

Preamplifier noise can be minimized by considering the noise figure contours of the preamplifier to be used and adjusting the frequency and impedance of the measurement to take advantage of the most favorable contours (see figure 5.10). The noise figure is related to the additional noise contributed by the preamplifier and is defined as:

$$NF(f,r) = (10dB) * log\frac{S_v^0(f)}{4k_BT_0r} \tag{5.6}$$

where S_v^0(f) is the background noise power spectral density. As can be seen in Fig. 10, the noise figure can vary significantly as a function of the source resistance and the frequency. An impedance matching transformer can be used to adjust the source resistance to an optimal value for the particular preamplifier. The frequency can also be adjusted through the use of an AC voltage source instead of a DC source.

In the circuit shown in Fig. 9 the constant voltage source is replaced with an

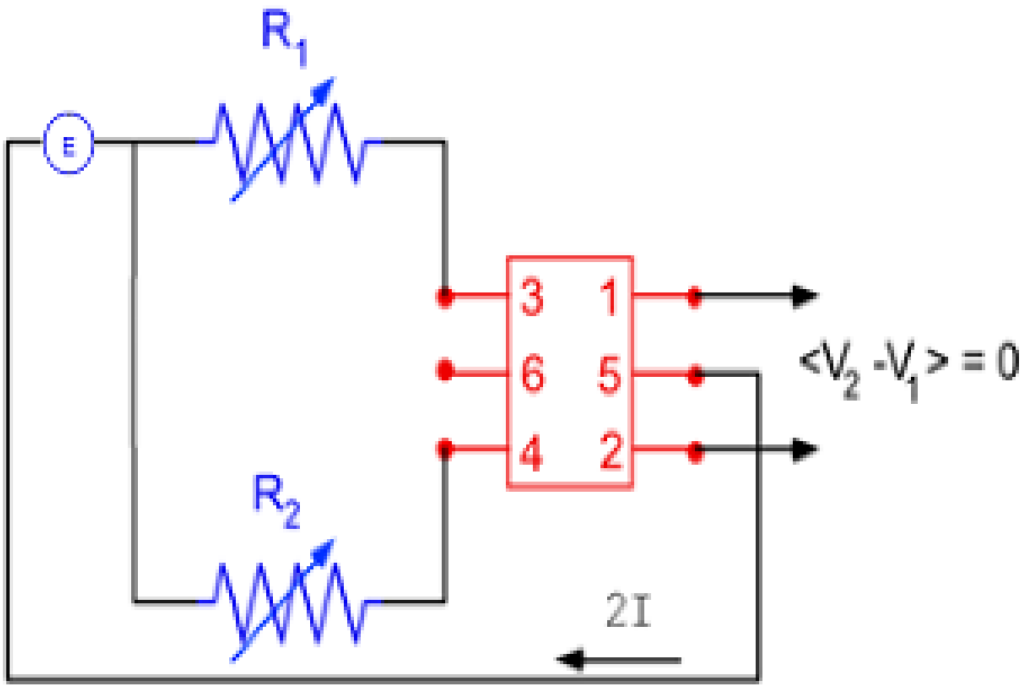

Figure 5.10: Circuit diagram for five-probe resistance fluctuation measurement circuit [91].

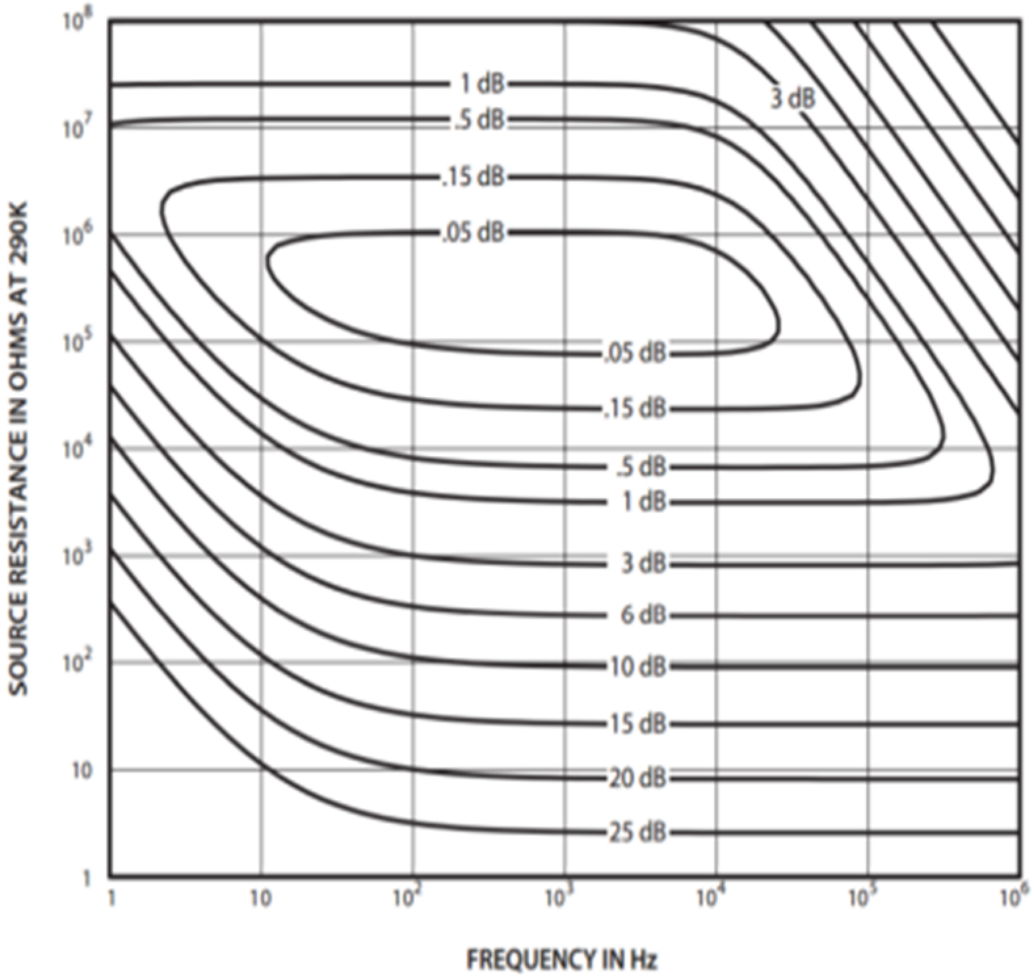

Figure 5.11: Noise contours of the SR560 preamplifier as a function of source resistance and frequency. The noise figure is as defined in equation 5.6 [94].

oscillating source. The frequency of this source can be chosen such that the noise from the preamplifier and transformer is minimized. Then the signal from the voltage contacts can be sent to a lock-in amplifier. The lock-in then demodulates the signal, resulting in an output of:

$$S_v(f;i)G_0^2[S_v^0(f_0-f)+(1/2)i_0^2S_r^-(f)(cos(\delta))^2] \tag{5.7}$$

where S_r^- is the resistance noise, S_v^0 is the background noise, G_0 is the lock-in gain and δ is the phase angle of detection for the lock-in. Thus by subtracting the power spectra found at $\delta=\pi/2$ from the spectra at $\delta=0$, the contribution from the background noise can be removed.

5.6 Resistance Fluctuation Measurement Apparatus

The Scofield 5-probe AC method was employed to measure the low-frequency resistance fluctuations exhibited by an indium oxide thin film. The rectangular device on the right of the diagram shown in figure 5.2 was used for measurement. These measurements were carried out in the K400 at various temperatures and applied perpendicular magnetic fields. The measurement circuit employed was similar to that shown in figure 5.10. The bias current across the sample bridge circuit was provided by a Stanford Research Systems SR2124 Dual-Phase Analog lock-in amplifier. This amplifier has a reference voltage source that has variable amplitude and frequency allowing the bias current to be adjusted and an optimal carrier frequency to be chosen. Voltages between 10mV and 10 volts were used to source the desired current. The front panel of the SR2124 was the location of the measurement circuit ground.

Taking the place of the adjustable resistors shown in figure 5.9, were a series combination of General Resistance Inc. Resist-O-Stat 2 decade resistor boxes and a metal film resistor of 150kΩ. This large resistance was chosen to limit fluctuations in the

total current sourced by the voltage source due to fluctuations in the sample resistance, contact resistance, and lead resistance. The decade resistors were used in balancing the bridge each time the applied magnetic field or temperature was changed. The resistance values set for each decade box was $\sim$5kΩ and the imbalance in the bridge was always less than 1kΩ and generally on the order of hundreds of ohms. A capacitor was placed in parallel to each decade resistor. In parallel to one was a fixed capacitance of 3.3nF. In parallel to the other was a General Radio type 1412-BC decade capacitor. These capacitors were necessary to balance the bridge because of the effects of stray capacitance of the cabling used in the circuit. The imbalance was generally on the order of 100pF.

The voltage across the bridge was amplified by a factor of 10^4 using a Stanford Research Systems model SR560 low-noise preamplifier. This preamp was placed close to the breakout box for the K400 to minimize the length of cabling between it and the sample. This reduced, to some degree, the background noise picked up. This preamp provided some signal filtering in addition to amplification. The SR560 has a built-in adjustable filter that was set to bandpass mode with an upper and lower bound of 10kHz and 100Hz, respectively. The AC bias current frequency was chosen to be 934.6 Hz. Looking at the noise contour for the SR560, shown in figure 5.11, this frequency falls near the center of the lowest noise contour. The two-terminal resistance of the noise measurement device varied between 50kΩ and 600kΩ depending on the applied magnetic field and temperature. This combination of frequency and source resistance effectively minimized the 1/f noise contribution from the preamp.

The output of the SR560 preamp was then sent to the SR2124 lock-in amplifier to demodulate the signal as described in the previous section. The lock-in also provided another stage of signal filtering with its input filter. This filter was set to bandpass mode centered around the carrier signal frequency with a Q-factor of 20. Lastly, the time constant was set to its minimum value to minimize the output filtering provided

by the lock-in.

The output of the lock-in was then sent through a Krohn-Hite model 3362 Butterworth filter. This was chosen to provide the flattest possible frequency response in the passband. It was set to low-pass mode with a cutoff frequency of 40Hz to provide anti-aliasing filtering. The output was then read by a National Instruments USB-6210 16-bit analog to digital converter sampling at 100 samples/S. The data from this converter was read-out and further analyzed using LabVIEW software.

Using LabVIEW, the voltage versus time trace for both the in-phase and out-of-phase components from the lock-in were recorded. Each trial was 16 hours in length. Additionally, a fast Fourier transform algorithm was applied to calculate the power spectrum. A series of 19 consecutively measured spectra were averaged. This averaging significantly increased the minimum frequency limit of the power spectra, but was essential to prevent any random spikes in the spectra from significantly skewing the spectral properties such as the slope or magnitude.

The carrier signal frequency was chosen to be 934.6Hz not just to minimize preamplifier noise. Another important consideration was the carrier signal frequency in relation to the AC power source frequency, 60Hz. The carrier frequency was deliberately chosen to not be near a harmonic of 60Hz to limit the power line noise picked up by the lock-in. The higher frequency also meant that the nearest harmonics (the 15th and 16th) were relatively weak. One drawback of this frequency was capacitive coupling to ground. The higher the carrier signal frequency, the more current that can reach ground without passing though the sample. This limited the maximum current that could be used in any of the measurements.

Ideally, the ballast resistors would be considerably larger than the sample resistance. This was true in the range of low temperature and low applied magnetic field where the sample was near the superconducting state, but not outside of this range. The

maximum resistance that could be used for ballast was limited by the need to source sufficient current to the film. To compensate for this the voltage source was adjusted as the temperature and applied field were changed between trials, to maintain a constant current. This limitation of the maximum ballast resistance was not believed to decrease the accuracy of the measurement because the measured resistance fluctuations of the sample, typically less than 0.5%, were still small compared to the ballast resistance.

By the nature of dilution refrigerator setup, it was not possible to have the measurement electronics near the sample itself. Relatively long cables (several meters) were needed to setup the measurement circuit. Since long cabling was used, it was important to consider the potential for the cabling to pick up external noise. The majority of the cabling in the measurement circuit external to the K400 was triaxial cable.

A triaxial cable has two coaxial signal leads and a grounded shield. This arrangement reduces inductive and capacitive pickup in the signal leads. The wiring inside the K400 used twisted pairs for the majority of its length to limit inductive pick up. The sample signal leads had sections of thermo-coax for filtering. In-line low-pass Pi filters were used at room temperature for every lead running to the sample and placed near the K400. Additionally, both the SR560 and the SR2124 were run in differential mode to take advantage of common-mode rejection to reduce external noise.

Another important consideration was the correct setting of both the carrier signal current and the phase of the lock-in. Since the high frequency carrier signal allowed some current to pass through to ground without passing through the sample, determining how much current was flowing through the indium oxide film was not as straight forward as would be expected. Measuring the current across an in-line resistor, such as a ballast resistor, was not an accurate measure. Instead, the current was forced across half of the sample by disconnecting one of the decade resistors. The voltage across the sample was measured using the SR2124 and compared with the previously measured sheet resistance

of the Hall bar using a DC technique. Using this voltage, the current actually flowing through the film could be calculated and adjusted as desired by changing the amplitude of the carrier signal voltage.

To set the phase, both decade resistors were set to zero and the decade capacitor was set to 3.3nF. The lock-in phase was adjusted until the y-output was zero. Then, both decade resistors were set to 5kΩ. Next, one of the decade resistors was adjusted until the x-output was zero. The decade capacitor was then adjusted until the y-output was zero again, to account for any change in the inductance of the circuit from the decade resistors. These last two steps were repeated for subsequently lower range settings on the lock-in until both outputs were on average zero and the range was as small as possible. This balancing procedure was considerably more difficult for lower sample resistance values, limiting how close to the superconducting state noise measurements could be made. The bridge was typically able to be balanced to at least one part in 10^4.

This experimental setup effectively separated the noise due to sample resistance fluctuations from other sources of noise. This was verified by the consistency of power spectra of the out-of-phase contributions as the applied magnetic field and temperature were varied. Additionally, the temperature was recorded concurrently to voltage fluctuations. The power spectra of the measured temperature fluctuations were measured and found to be frequency independent down to 1mHz and therefore concluded to be unlikely to be a significant contribution to the measured resistance fluctuations that generally exhibited 1/f noise. A noise floor of $\sim 10^{-20} \mathrm{V}^2/\mathrm{Hz}$ was achieved between 10mHz and 10Hz, which is comparable to what others have achieved [95]. This background was higher at lower frequencies, likely due to 1/f noise from the various pieces of electronic equipment used in the measurement.

5.7 Resistance Fluctuations Exhibited by Indium Oxide

The measured resistance fluctuations were analyzed using several techniques, including the calculation of the power spectra, histograms of the resistance fluctuations, and the so called second spectra. Each of these techniques provided useful information with regard to understanding the indium oxide film in the vicinity of the SIT. All three will be discussed in detail in this section starting with the histograms of the resistance fluctuations.

The most straightforward of these analysis techniques is the generation of histograms of the resistance fluctuations. To calculate the histograms, the starting point is the voltage versus time traces. However, the raw voltage versus time traces were not particularly useful without first applying some filtering. As was discussed in the previous section, the Scofield method generated two voltage versus time traces, one in-phase and the other out-of-phase. The in-phase voltage included the sample resistance fluctuations and background fluctuations. The out-of-phase contained only background noise. To generate a voltage versus time trace that was representative of just the sample resistance fluctuations a Weiner filter was applied.

The first step in applying a Weiner filter is to take the Fourier transform of both voltage versus time traces [96]. Once in the frequency domain the filter transfer function, Φ, could be found,

$$\Phi = \frac{|S(f)|^2}{|S(f)|^2 + |N(f)|^2} \tag{5.8}$$

where S(f) is the Fourier transform of the corrected voltage versus time trace and N(f) is the transform of the background trace. Additionally, C(f) is the transform of the time trace including both the signal and background. Since $|C(f)|^2=|S(f)|^2+|N(f)|^2$, equation 5.8 can be rewritten in a more useful form,

$$\Phi = \frac{|C(f)|^2 - |N(f)|^2}{|C(f)|^2} \tag{5.9}$$

Once Φ is calculated, the transform of the filtered time trace can be obtained by multiplying the transform of the in-phase trace by the filter transform function. Then the inverse Fourier transform can be applied to obtain a filtered voltage versus time trace that only includes sample fluctuations. The filter transform function was recalculated for every trial conducted.

Using the filtered trace, the average voltage was calculated and then the deviation from the average at every point in time was found. This deviation was then divided by the current to find deviations in resistance. The resistance deviations were then divided by the total resistance of the sample at the given temperature and applied magnetic field to find the normalized resistance fluctuations. These normalized fluctuations were then grouped into 500 bins and normalized by the number of measurements when calculating the histograms. Both the application of the Weiner filter and the histogram calculations were implemented using Matlab.

Histograms of the normalized resistance fluctuations were calculated at a variety of temperatures and different applied perpendicular magnetic fields, both above and below the critical field for the SIT, 2.486T. To characterize these histograms, they were fit by a Gaussian. The quality of the fit and the full width at half max (FWHM) were useful to quantify the characteristics of the histograms. Essentially, they were a measure of how Gaussian the fluctuations were, as well as their relative intensity. From figure 5.12, with the exception of an outlier at 100mK, 3.5T, the normalized FWHM tends to decrease as the applied magnetic field increases. There also appears to be a tendency for the FWHM to decrease as the temperature increases. Lower resistance corresponds to stronger relative fluctuations in the resistance.

The degree to which the observed fluctuations conformed to a Gaussian distribution was also characterized. This was quantified with the resultant chi-squared values

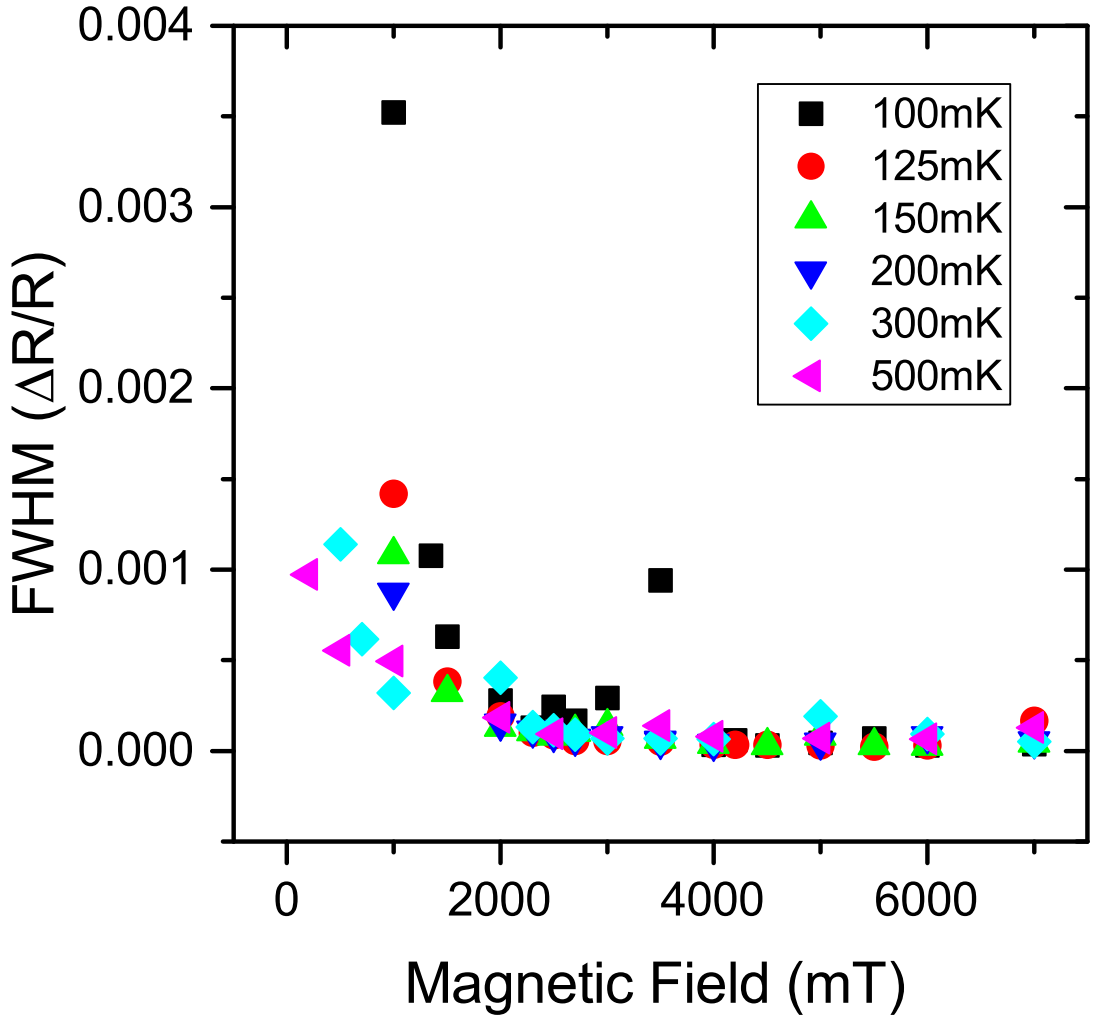

Figure 5.12: FWHM of normalized resistance fluctuations measured at various temperatures and applied magnetic fields. These fluctuations tend to increase at lower temperatures and applied fields. Typical fluctuations never exceeded 0.5% of the total resistance.

obtained when fitting a Gaussian to the data. This is shown in the color plot with figure 5.13. Generally, a Gaussian distribution was observed for the majority of the range of temperature and applied magnetic field. In some instances, non-Gaussian behavior was observed at lower and intermediate field values but was not reproducible. These measurements were disregarded. Near the SIT there seems to be no noteworthy changes in the value of chi-squared. However, at higher field values and lower temperatures, well beyond the SIT, there were some non-Gaussian distributions that were repeatable at times.

From figure 5.13, the change to non-Gaussian behavior does not seem to happen smoothly and systematically. Additionally, not every trial at a fixed temperature and field would produce a similar chi-squared value. It is likely that the fluctuations responsible for this behavior are relatively rare and don't always occur within the 16-hour measurement window. For the cases at lower applied fields where non-Gaussian fluctuations were observed but not repeatable, it is not clear if they were caused by an extremely rare fluctuation, or from an external source that was unable to be effectively filtered. Based on this it seems that non-Gaussian behavior is most likely to occur at low temperatures, below 300mK, and at high fields, above 4.5T.

The Gaussian behavior of the film over the majority of the studied phase space indicates that the fluctuations are predominately caused by independent fluctuators, as opposed correlated fluctuations. This differs from what has been observed in other systems undergoing a phase transition. Non-Gaussian fluctuations have been observed in $LaSrCuO_4$ near the BKT transition, near the metal-insulator transition in silicon inversion layers, and near the BKT transition in NbN films[74, 93, 97].

One possible reason that non-Gaussian behavior was not observed near the SIT for the indium oxide film studied here is the high level of disorder of the film [74, 97]. It has been found by others that high disorder can suppress the correlated fluctuation

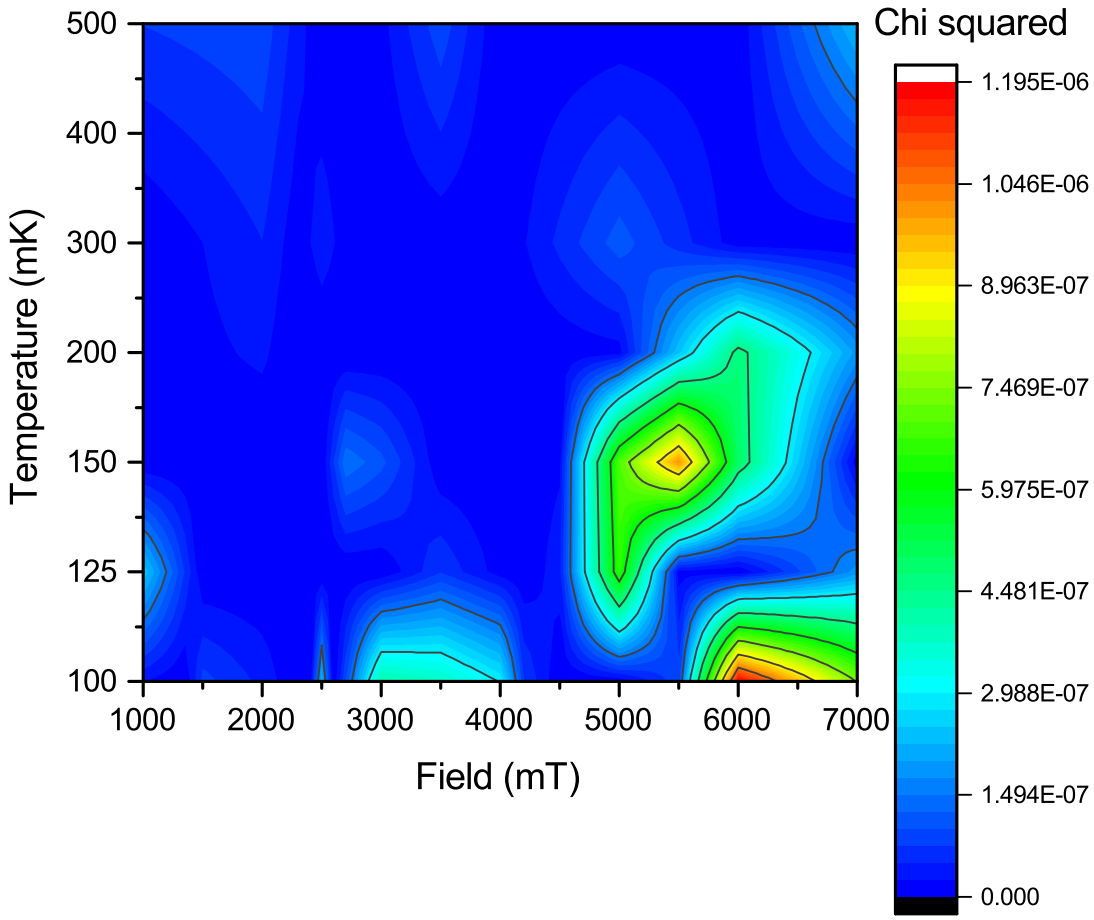

Figure 5.13: Color plot of chi-squared as a function of temperature and applied magnetic field. Low values of chi-squared indicate Gaussian behavior. The high field and low temperature regime indicates a tendency for non-Gaussian fluctuations to occur.

necessary for non-Gaussian behavior to occur. For the case of the BKT transition, the pinning of vortices in disordered or granular superconductors has been shown to limit long-range interactions [98, 99]. The high disorder present in indium oxide films that undergo a SIT may limit non-Gaussian fluctuations that would otherwise be present near the SIT in systems with less disorder.

Another important technique for analyzing resistance fluctuations is to study the first spectra. This was done by taking the Fourier transform of the voltage versus time traces for both the in-phase and out-of-phase components measured using the Scofield method. By subtracting the two, the true power spectra of just the resistance fluctuations could be found at various temperatures and applied magnetic fields. Looking at figure 5.14, typically the corrected spectra exhibited 1/f noise from less than 1mHz up to ∼20Hz.

The lower frequency bound was limited by the total measurement time and the upper bound was limited by the low-pass Butterworth filter. The out-of-phase spectra shown in figure 5.15, which correspond to the background noise, were generally flat between 0.1Hz and 20Hz, however this would vary somewhat between trials. Below ∼0.1Hz the background spectra tended to increase in magnitude. The regime where the background noise was white noise was likely dominated by the Johnson noise of the sample, ballast resistors, and cabling. The deviation from white at low frequency was likely due to 1/f noise from the various measurement electronics becoming the dominant background noise source.

The corrected spectra were characterized using the slope and intercept when plotted on a log-log scale as is typical for 1/f noise. The slope of the various spectra ranged from -0.64 to -1.10, with the vast majority between -1.00 and -1.05. The intercept, which corresponds to the power spectral density at 1Hz, was useful when calculating the Hooge parameter as defined in equation 5.4. No systematic change in the slope as a function of temperature or magnetic field was observed, however, the intercept did

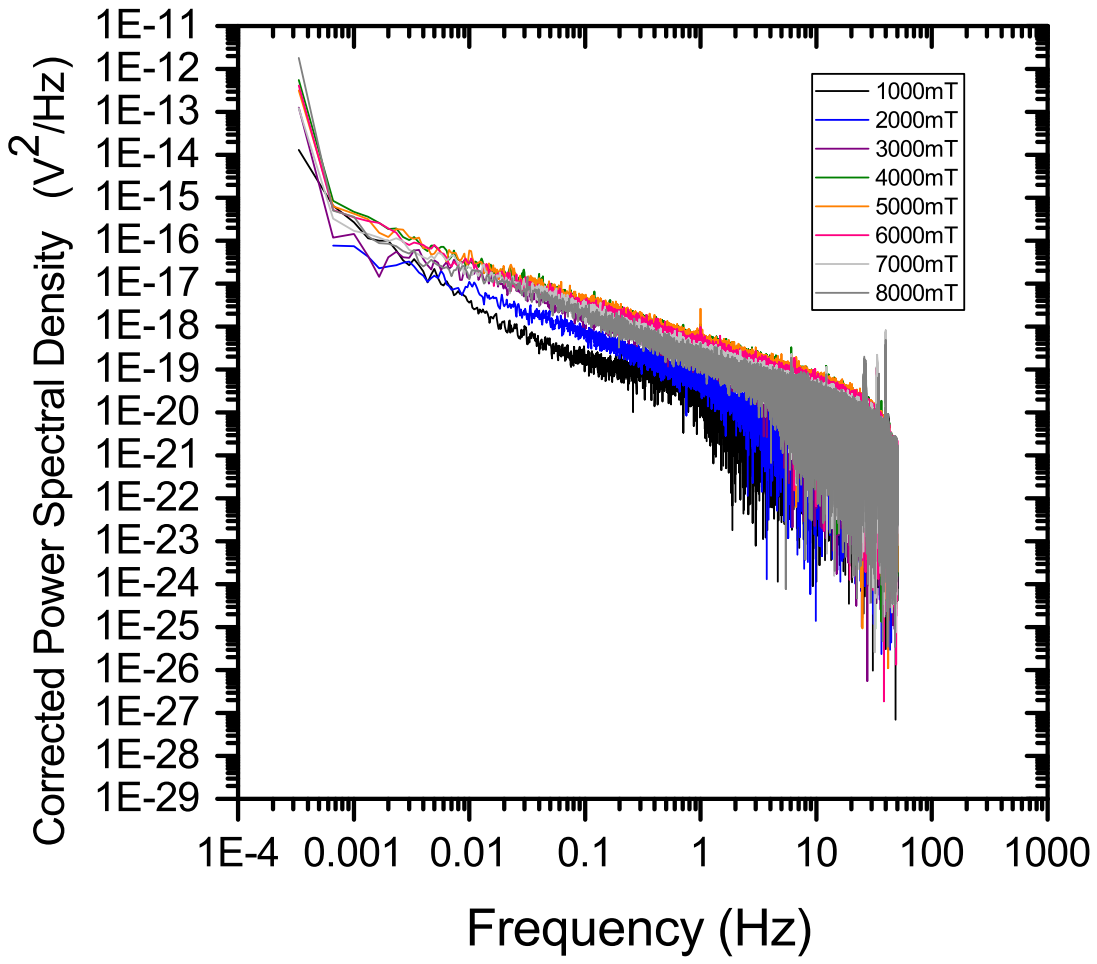

Figure 5.14: Plot of several corrected power spectra measured at a temperature of 100mK and at various applied magnetic fields.

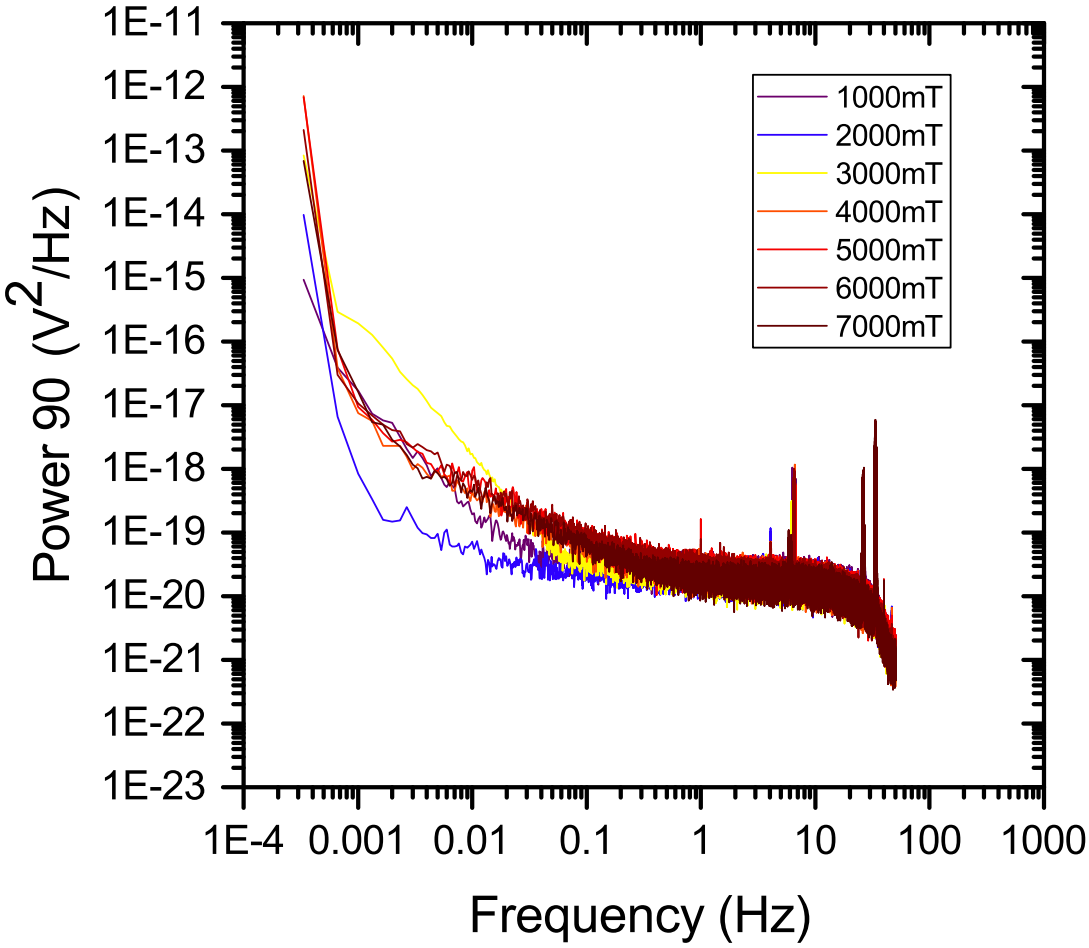

Figure 5.15: Plot of several background noise power spectra, 90 degrees out-of-phase.

change systematically. The Hooge parameter is directly proportional to the intercept and changed considerably as the field and temperature were varied.

The intercept and the uncertainty in the intercept were calculated using Matlab. Each voltage versus time trace was separated into 20 equal length segments. For each segment a Fourier transform was applied to both the in-phase and out-of-phase traces to find a series of corrected spectra. Once the corrected spectra were found the logarithm was taken for both the power and frequency. A linear fit was applied separately to each decade of frequency from 1mHz to 10Hz. The average of the intercept found in each of these fits was taken as the intercept corresponding to that time segment.

The voltage versus time traces were sampled at 100Hz and correspondingly the power spectra were evenly spaced in frequency. When plotted on a log-log scale this results in a progressively higher data density in the higher frequency decades. Equal decade weighting was used to determine the intercept in order to prevent the higher frequency data from completely overwhelming any low frequency contributions to the fit. The value of the intercept at a fixed temperature and applied magnetic field was the average value obtained from the 20 traces. Additionally, the standard error was calculated. With the intercept and standard error, the value of α at each temperature and field could be calculated and error bars could be estimated based on the standard error in the intercept value.

Examining figure 5.16, it is clear that α changes in a roughly linear fashion with respect to the sheet resistance when plotted on a log-log plot. The implications of this behavior will be discussed in great detail in the next section. It is noteworthy that α is considerably larger than for typical metals, such as copper or silver, which have values on the order of 10^{-4}-10^{-1} [100, 67].

Elevated α values for polycrystalline indium oxide films have been previously observed by Ovadyahu [80], who found values ranging from 10^3 to 10^7. The films studied

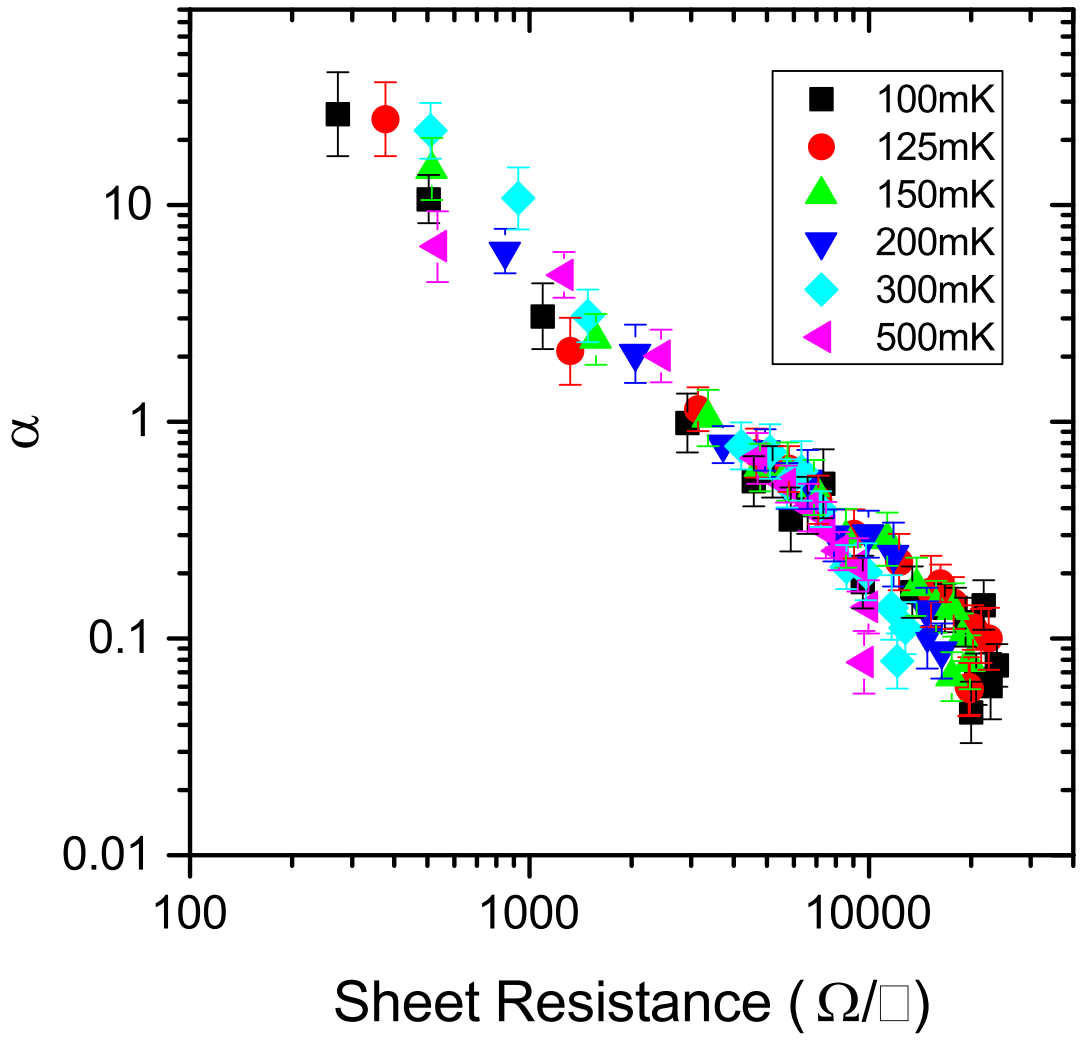

Figure 5.16: Plot of the Hooge parameter, α, as a function of the sheet resistance for temperatures of 100mK, 125mK, 150mK, 200mK, 300mK, and 500mK. The total number of atoms present in the film was estimated to be $9.92*10^{13}$.

by Ovadyahu underwent metal-insulator transitions and it was argued that they were examples of the Anderson transition. The film reported in this chapter instead was undergoing a superconductor-insulator transition and had α values that changed with magnetic field and temperature in between those observed in ordinary metals and in films measured by Ovadyahu. As the sheet resistance increased, α decreased, and approached values more typical of an ordinary metal.

Finally, the resistance fluctuations were characterized by looking at second spectra. Second spectra are calculated by first obtaining the first power spectrum for many consecutive equal length segments of the voltage versus time trace. Next, the power is integrated from some frequency F, to 2F, for both the in-phase and out-of-phase spectra. These two power levels are subtracted. Lastly, the Fourier transform of this integrated power versus time is taken to obtain the second spectra [16].

Second spectra provide important insights on the nature of the fluctuations that are not able to be discerned directly from the first spectra. When the noise consists of uncorrelated fluctuations the second spectra will be frequency independent [101]. The second spectra were calculated for the measured resistance fluctuations of the indium oxide film discussed in this chapter. The first spectra were integrated from 0.1 to 0.2Hz. The resulting second spectra were plotted on a log-log scale and a series of linear fits were performed. The second spectra were essentially frequency independent.

From figure 5.17, the slopes at each temperature as the applied magnetic field was varied exhibited no systematic change. The slope values are scattered about zero. This suggests that there is no discernable frequency dependence to the second spectra and the fluctuations observed are uncorrelated. Similar results were observed with a couple different choices of frequency window used in the integration.

The conclusion that the fluctuations are uncorrelated is consistent with the Gaussian distribution of resistance fluctuations that were seen when generating histograms

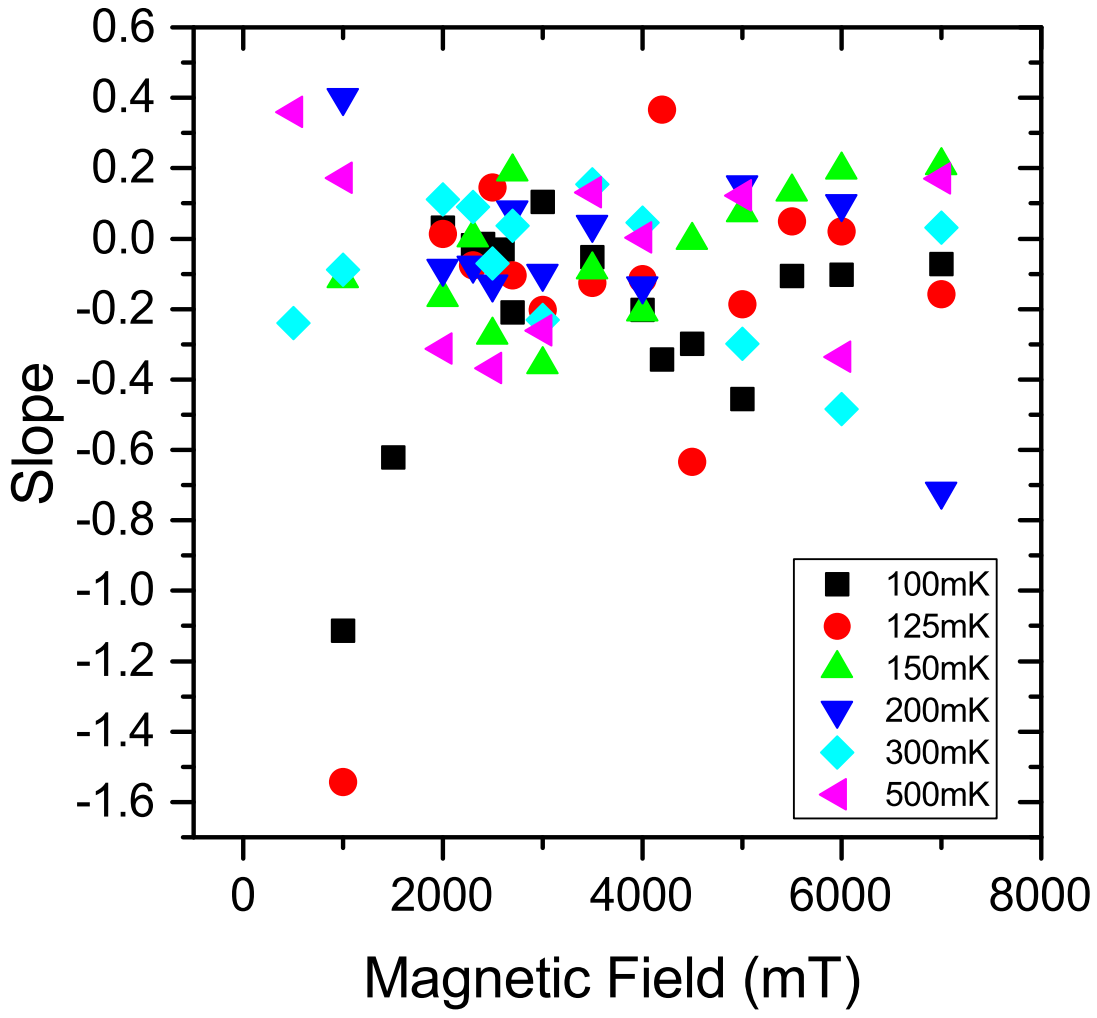

Figure 5.17: Log-log plot of the slope of the second spectra vs. magnetic field obtained for measurements at temperatures of 100mK, 125mK, 150mK, 200mK, 300mK, and 500mK at applied magnetic fields from 500mT to 7000mT. The values of the slopes appear randomly distributed around zero indicating no frequency dependence to the second spectra.

of the fluctuations. It can be shown that uncorrelated fluctuations not only result in a frequency independent second spectrum, but also a Gaussian distribution [101]. The non-Gaussian distributions observed at low temperatures and high magnetic fields indicate the possibility of correlated fluctuations in this regime. This is not necessarily incompatible with the second spectra observations. Correlated fluctuations that occur at frequencies outside of the window of integration, such as those well below 0.1Hz, would not show up in the second spectra.

It is plausible that correlated fluctuations occurred at low frequencies and were relatively rare events. This would explain why at fixed field and temperature the histograms were not always repeatable. Over most of the range of temperature and applied field the histograms were consistently Gaussian, but where non-Gaussian behavior was observed, it did not necessarily occur in every trial. Extremely low frequency fluctuations might not occur even once during a 16-hour measurement, or only once or twice. Evidence of this was also observed in the raw voltage versus time traces. It is not clear why these rare events happened at low temperatures and high fields, but not repeatably anywhere else, especially in the vicinity of the SIT.

While most external sources of noise are significantly rejected from the measurement by careful setup and implementation of the Scofield method, it was important to thoroughly rule out temperature fluctuations as a possible source of the measured fluctuations. Since the resistance of the sample is strongly temperature dependent, any temperature fluctuation could cause resistance fluctuations. Due to this, if significant temperature fluctuations were to occur, they would still be present in the corrected spectra. A test for this is to compare the measured spectra as the field and temperature are varied against dR/dT.

Taking $S_v(f)$ to be the Fourier transform of the corrected voltage versus time trace, the resistance noise power can be defined as $S_R(f) = S_v(f)/I^2$. For fluctuations caused

by temperature fluctuations modulating the sample resistance, S_R is expected to be proportional to $(dR/dT)^2 * T^2$ [88]. Figure 5.18 and figure 5.19 show S_R(f=1Hz) and $(dR/dT)^2 * T^2$, respectively. Looking at figure 5.19, there is a significant drop in the value of $(dR/dT)^2 * T^2$ around 2500mT. This corresponds to the critical field for the SIT where the resistance is expected to be temperature independent and hence (dR/dT) is small. No sign of this feature is evident in 5.18. The noise power continues to increase without interruption until 5000mT where it begins to gradually decline. The absence of the dramatic dip in $(dR/dT)^2 * T^2$ around 2500mT showing up in S_R provides further evidence that temperature fluctuations are not a significant contributor to the observed fluctuations.

5.8 Noise Exponents and Percolation

In classical percolation models there is a mixture of two materials, one with a finite resistivity and one with an infinite resistivity that is insulating. As the mixture of the two materials is tuned from fully insulating toward fully resistive, the overall mixture will remain insulating until some critical fraction, p_c, consists of the resistive material. Prior to reaching p_c there are regions of resistive material with finite size, but these regions are not connected. Any current that passes through the material must pass through at least some insulating material.

At p_c the last link between resistive clusters is formed and current is able to pass. This single link would have a significant effect on the total current flowing and any fluctuations of this single link have a dramatic effect on the total voltage fluctuations across the entire system. As p continues to increase there are more and more parallel paths for current to flow through the material. This lowers the overall resistance and decreases the influence any single link can have on the overall voltage noise. This is qualitatively consistent with equation 5.4.

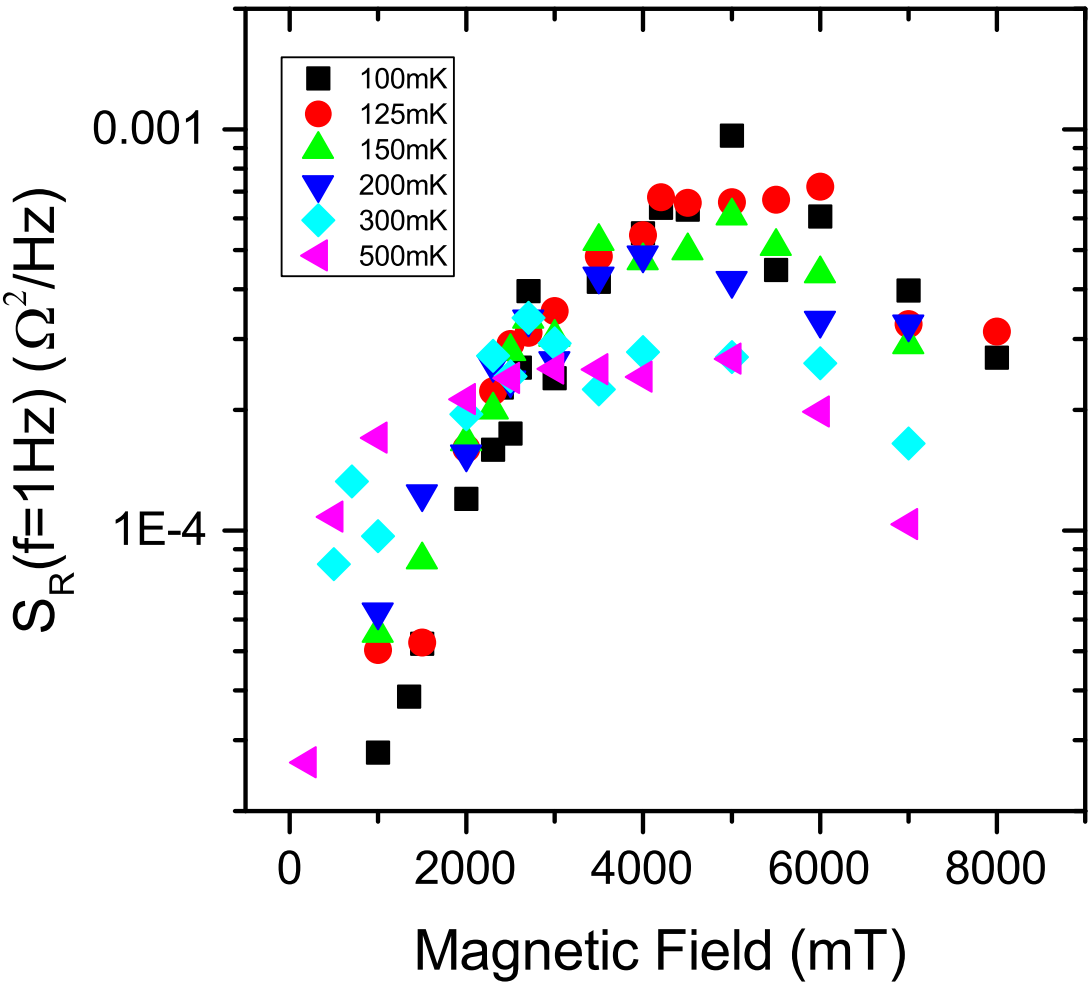

Figure 5.18: Plot of the resistance noise power at 1Hz as a function of applied magnetic field at various temperatures.

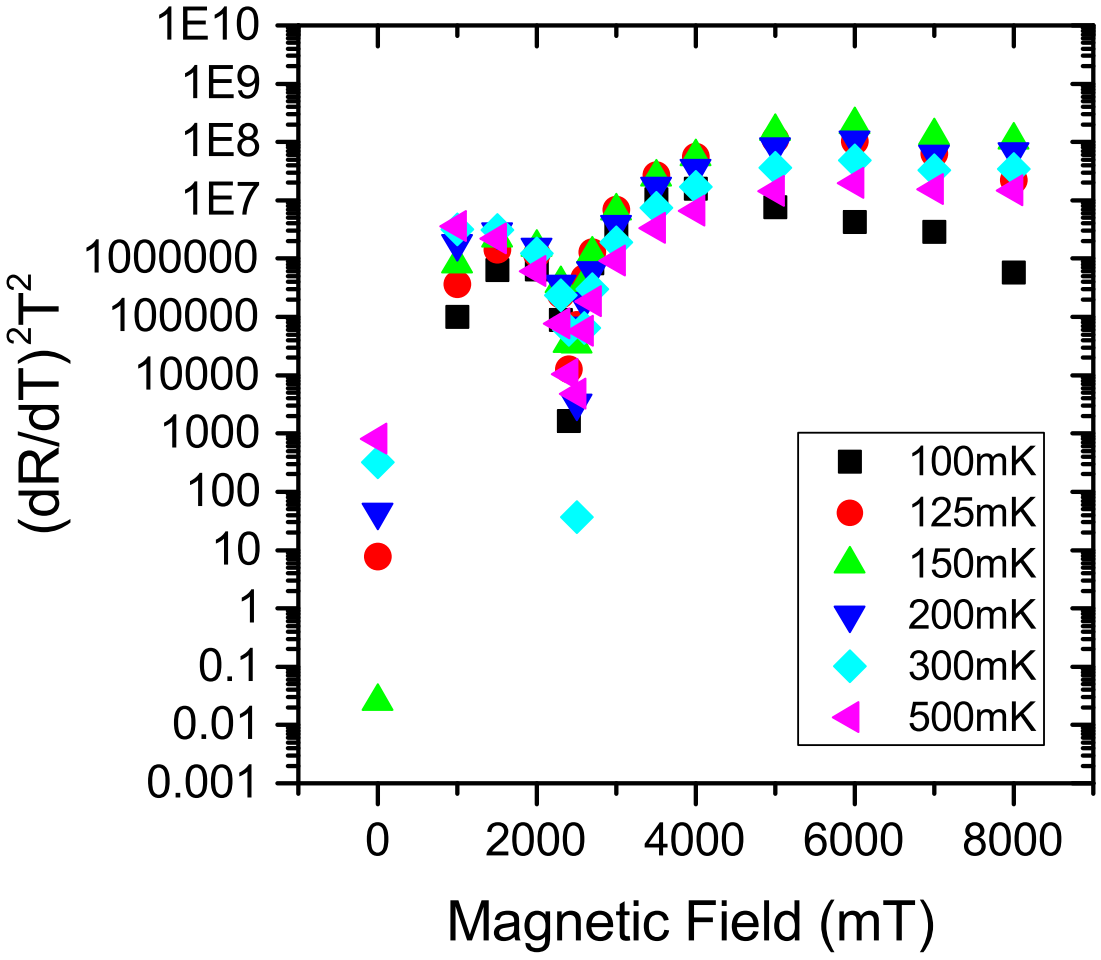

Figure 5.19: Plot of $(dR/dT)^2 * T^2$ as a function of applied magnetic field at various temperatures.

In equation 5.4, Ω is the sample volume or the number of atoms in the sample, both of which are proportional. In the percolation model, well above p_c, there are many conductive paths and the effective volume is large. As p decreases toward p_c there are fewer parallel conductive paths causing a larger current density at various bottlenecks. This leads to reduction in the effective volume that controls both the sample resistance and resistance noise. As would be expected from equation 5.4, this reduced effective volume leads to a larger voltage noise power as the percolation threshold is approached from the conductive side.

A similar argument can be made for the percolation transition from a superconductor to a metal. This case is modeled as a mixture of superconducting and resistive material. Once again p is the volume fraction of resistive material. For $p<p_c$ there is at least one superconducting path through the material and the system is superconducting. At p_c, the threshold for finite resistance, there is a single resistive path connecting superconducting clusters. This single resistive link controls the resistance and resistance fluctuations of the entire system. As p continues to increase there are more resistive links along the path of minimal resistance and more parallel resistive paths. This increases the effective volume controlling the resistance and noise, thus resulting in less noise.

The change in resistance and noise levels near the percolation threshold can be quantified [102, 103, 104, 105, 106, 107, 108, 109, 110, 111, 112, 113]. The resistance is expected to change in the following ways,

$$R_{rs} \propto (p - p_c)^s, (p > p_c) \tag{5.10}$$

for the superconductor-metal mixture, and

$$R_{ri} \propto (p - p_c)^{-t}, (p > p_c) \tag{5.11}$$

for the metal-insulator mixture. The values of s are 1, 1.297±0.07, and 0.73±0.011 for one, two and three dimensions, respectively. The values of t are 1.297±0.07 and

1.96±0.1 for two and three dimensions, respectively. The normalized noise level can be quantified by,

$$S_R/R^2 \propto R^{-l} \tag{5.12}$$

for both cases. The value of l for the superconductor-metal mixture takes values of 1, 0.86±0.02, and 0.9±0.32 for one, two, and three dimensions, respectively. For the metal-insulator mixture l takes values of 0.86±0.02 and 0.80±0.1 for two and three dimensions, respectively.

The classical model of percolation of random resistor networks described so far in this section falls short of describing some superconducting and insulating materials. In some systems quantum effects are more significant and new exponents taking these corrections into account need to be used. These new exponents were found by Kiss and Svedlindh [114]. This model takes the system to be a network of Josephson junctions.

This approach has been commonly applied to describe granular superconductors, including the work of Deutscher et. al., Orr et. al., and Frydman et. al. [115, 116, 117]. The system is modeled as a random array of junctions between neighboring superconducting grains and as a percolation problem. Starting with all the junctions connected with random strength coherent superconducting links when at low temperature and zero applied field, the film is overall superconducting. Then as the applied magnetic field is increased it progressively weakens the Josephson coupling and causes additional links to become resistive. Each additional resistive link is of lower resistance. Eventually there will be one final superconducting link suppressed resulting in the breaking of the infinite cluster.

At the point that the infinite cluster just breaks there will be a single resistive link that all the current must pass through. This bottleneck controls both the resistance and the noise of the overall system. Links with resistance higher than this value do not influence the properties of the system since they are shunted by superconducting

or lower resistance links. Links that are superconducting or lower resistance than the bottleneck do not form an infinite cluster and current must still pass through the bottleneck. The resistance of the link comprising the bottleneck is expected to be $h/4e^2$. In the limit of zero temperature the system would be expected to abruptly change from superconducting to this critical resistance and exhibit maximal noise at this point since the effective volume controlling the noise is at its minimum.

At nonzero temperatures individual junctions will exceed their critical temperature at progressively lower temperature as the field increases making it possible for resistance values between zero and the universal resistance to be realized. The breaking of the infinite cluster at finite temperature, which corresponds to the minimum effective volume controlling the noise, will occur at far lower resistance values, as soon as the film exhibits finite resistance. This moves the resistance corresponding to maximum normalized noise well into the superconducting regime. Even at nonzero temperatures, the universal resistance is still expected to separate the R(T) curves with positive and negative slope, corresponding to the superconducting and insulating regimes.

Kiss and Svedlindh assumed that the Josephson coupling energy would fluctuate to a large enough degree that some of the Josephson junctions in the array would switch on and off [114]. This random switching of the junctions would produce random fluctuations in the resistance of the system and hence resistance noise. Taking $\Delta p_r(t)$ to be the spontaneous fluctuations in the density of resistive junctions as a function of time and $p_r(T)$ to be the average density of resistive junctions at a given temperature, the change in resistance can be written as,

$$\Delta R(T;t) = \frac{dR(p_r(T))}{dp_r} * \delta p_r(t) \tag{5.13}$$

Next taking the derivative of equation 5.10 and rearranging,

$$\Delta R(T;t) \propto R^{1-1/s} \Delta p_r(t) \tag{5.14}$$

The normalized noise power is then,

$$\frac{<\Delta R^2(T;t)>}{R^2(T)} \propto R^{-2/s} < \delta p_r^2(t) > \tag{5.15}$$

Finally, taking the Fourier transform to obtain the normalized noise spectrum,

$$\frac{S_R(f,T)}{R^2(T)} \propto R^{-2/s}(T) S_p(f,T) \tag{5.16}$$

where S_p(f,T) is the noise spectrum of Δp_r(t) at temperature T. If the temperature dependence of Δp_r(t) is weak compared to the temperature dependence of R, the normalized noise can be expressed as a power function of R with a new exponent when compared to equation 5.12. This new noise form is called p-Noise [118].

The distinguishing characteristic of p-model percolation from classical percolation is the random switching of the junctions. In classical percolation, whether or not an individual bond is resistive or not is fixed for a given value of the tuning parameter. The resistive bonds act like noisy resistors. In the p-model the resistive bonds are not noisy, and their number is not fixed. For a given value of the tuning parameter, there is an average number of resistive bonds, but the actual number at any given time can fluctuate around this average. The source of noise is the random switching of bonds from being resistive to either superconducting or insulating as opposed to resistance noise intrinsic to individual resistive bonds.

The fluctuation of the coupling energy that causes the switching have several different causes [119]. One such cause is defect motion changing the electron scattering cross-section. Another cause is the fluctuation of the occupation of trapping sites in the junction area. Another source is random magnetic flux motion. Lastly, temperature fluctuations can cause fluctuations in the coupling energy, however this was ruled out for this indium oxide film for the reasons argued in the previous section.

The previously described derivation can be repeated in an analogous manner to find a corrected exponent for the case of a metal-insulator mixture as well. The new exponent

values for the superconductor-metal mixture are 2, 1.54±0.09, and 2.74±0.04 for one, two and three dimensions, respectively. For the case of the metal-insulator mixture the exponents are 1.54±0.09 and 1.02±0.05 for two and three dimensions, respectively. Experimental results consistent with these new exponents have been observed in some high-Tc superconductors.

Kiss et. al. [119] studied conductivity noise in $YBa_2Cu_3O_7$ thin films. These films are high-T_c superconductors with a T_c of ∼90K. Films were made using both ex situ and in situ processes and the two exhibited markedly different noise behavior. Comparing equations 5.16 and 5.4 it is clear that α scales with the resistance with the same power-law relation. It was found for the ex situ grown films that the two films studied had scaling exponents of -1.0 and -0.9. This is in close agreement with the value of 0.86 expected for the classical percolation model.

For in situ films the noise properties were different. Once again two films were studied, and both exhibited a power-law relation between the resistance and α. However, the transition in this case had two stages separated by a crossover from two-dimensional behavior at the lowest temperatures to three-dimensional behavior at higher temperatures, as shown in figure 5.20. This crossover happened because the correlation length increases as temperature increases and once it is larger than the thickness of the film, the system is effectively two dimensional. The exponent values found were -1.51 and -2.76 for sample one and -1.58 and -2.75 for sample two for the two and three-dimensional regimes, respectively. This is in good agreement with the predicted values of -1.54 for two dimensions and -2.74 for three dimensions.

Similar behavior has been observed in other materials. For example, in quasi-two-dimensional organic charge-transfer salts (BEDT-TTF)2X (where BEDT-TTF stands for bis-ethylenedithio-tetrathiafulvalene, representing $C_6S_8[C_2H_4]_2$, often abbreviated as

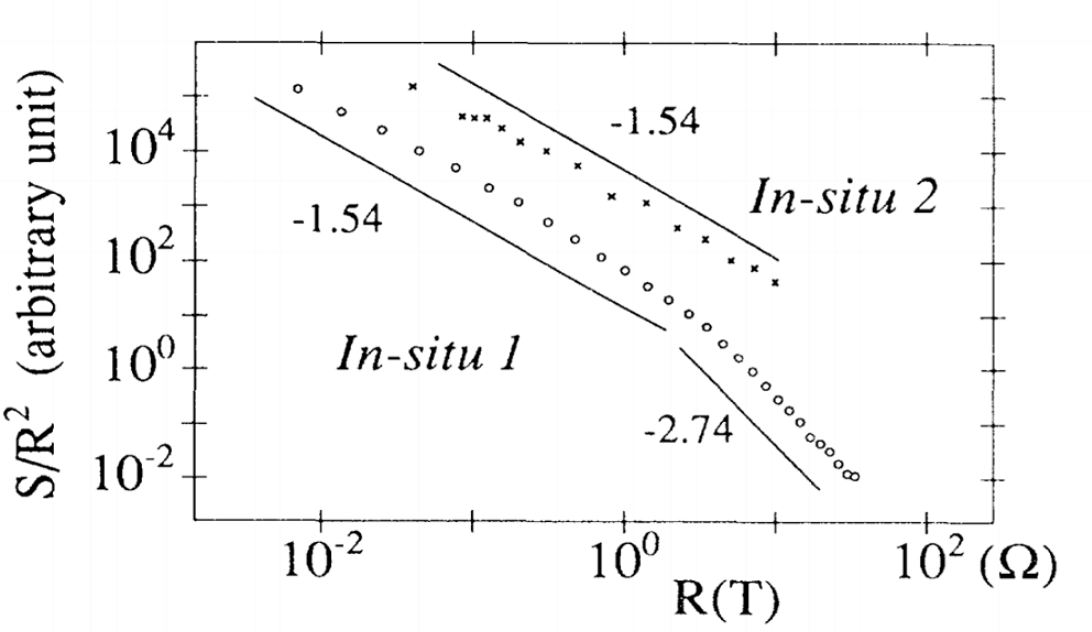

Figure 5.20: Above is a plot of the normalized noise levels for two in situ films. The added lines are to guide the eye and have slopes that correspond to the exponent values predicted for two and three-dimensional systems following p-model percolation [119].

ET, and X is $Cu[N(CN)_2]Cl$), which undergo a field-tuned superconductor-metal transition, a noise exponent of 2.74 was observed in the high field regime [120]. This value is consistent with what was predicted for a 3D system. In WSe_2 field effect transistors exhibiting metal-insulator transitions noise exponents of -1.5±0.2 were observed by Paul et. al., in agreement with the prediction for 2D [121]. $BaFe_2As_2$ superconducting films and $FeTe_{0.5}Se_{0.5}$ epitaxial thin films exhibited exponents consistent with the predicted values for 3D and 2D, respectively [122, 123].

Looking back to figure 5.16, it is clear that α changes in a linear fashion with respect to the sheet resistance when plotted on a log-log scale. The slope would then correspond to the exponent value of a data set that follows a power law relation. To more clearly illustrate the linear behavior and lack of temperature dependence, figure 5.21 shows the same data with the temperature not indicated and some linear fits. These linear fits include a best fit line of the data, a line corresponding to the classical percolation exponent and a line corresponding to the p-model percolation exponent.

The line of best fit is shown with the dashed line. This linear fit was done from the lowest resistance value at which α was measured up to ∼6000 Ω/□. This cutoff was chosen because at higher resistance values the data starts to spread and the linear approximation begins to breakdown. This systematic deviation at the highest resistances can be more clearly seen in figure 5.16. In this regime, across the temperature range, α decreases at fixed or even decreasing resistance. Additionally, the critical resistance for the SIT is ∼5700 Ω/□ which is a natural choice to cutoff the fit. The best fit indicates an exponent value of -1.33±0.14. This isn't in perfect agreement with the predicted value for p-model percolation, but is much closer to p-model percolation than classical.

The classical percolation fit is indicated by the dot-dashed line. This fit clearly does not fall within the spread and uncertainty of the data. The p-model percolation fit is indicated by the solid line. This doesn't match the ideal fit line, but it does fall within

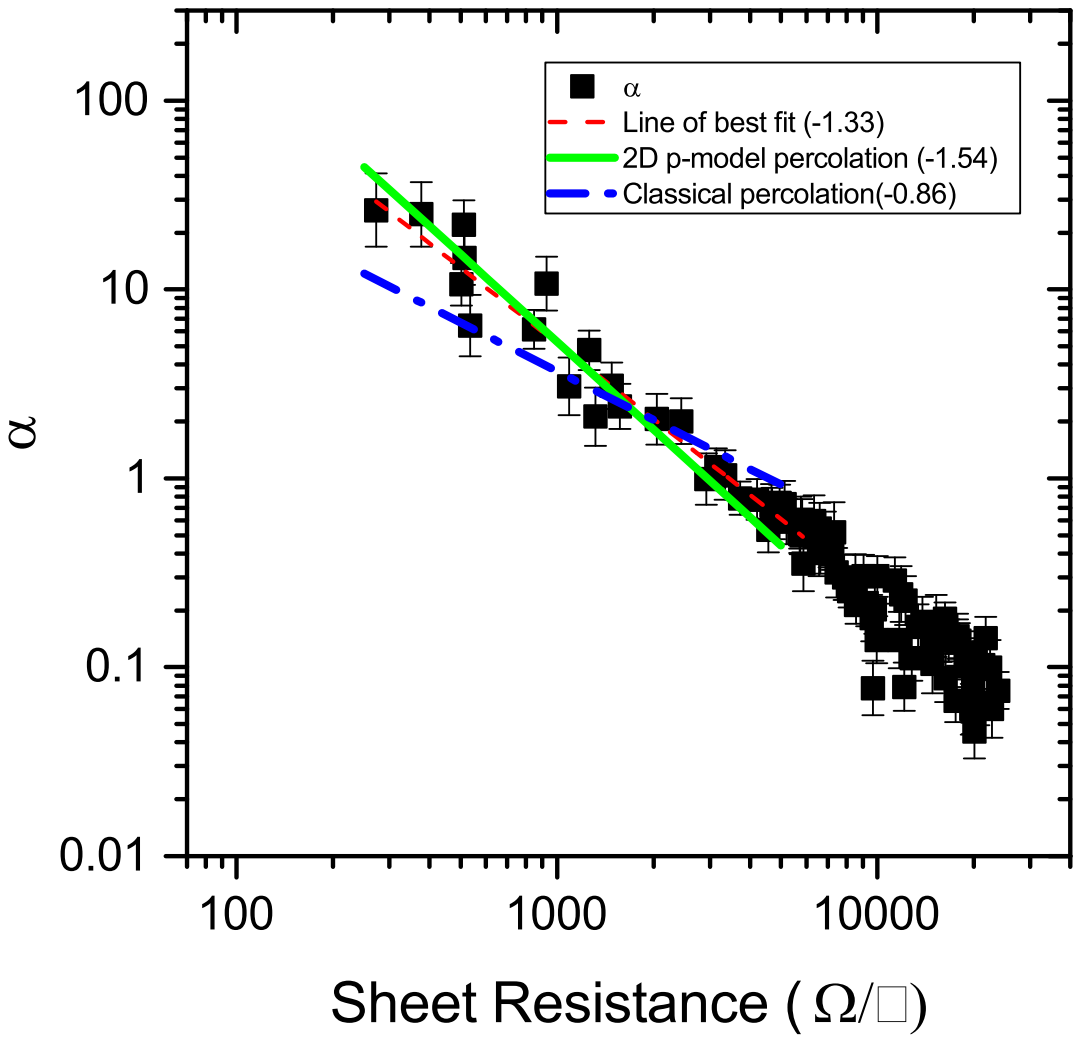

Figure 5.21: Log-log plot of α versus sheet resistance. The line of best fit, shown with a dashed line, has a slope of -1.33±0.14. The lines corresponding to the p-model and classical percolation models are indicated with a solid line and a dot-dash line, respectively. The slope values are listed in the legend.

the spread and uncertainty of the α data. This suggests that the p-model percolation model based on a network of fluctuating Josephson junctions models the transition out of the superconducting state, toward insulating, exhibited by this indium oxide film. Additional evidence for the p-model percolation model was provided by looking at the current dependence of α at a fixed current and applied magnetic field.

Once again, Kiss and Svedlindh [114] used a Josephson junction array to model the behavior of the systems as superconductor-metal transitions. The junctions in this array, like all Josephson junctions, have some critical current above which the junction becomes resistive and no longer passes a supercurrent. In a random network modeling a disordered material, like amorphous indium oxide, not all junctions will have the same critical current. Instead there is expected to be a wide distribution of critical currents for individual junctions. For a given current sourced across the system, the local current will exceed the critical current for some junctions and not others. As more current is sourced, the local current densities will exceed the critical current of a larger fraction of the junctions. Similar to the field tuned case, this will lead to an increase in the effective volume controlling both the resistance and noise.

Looking at figure 5.22, the Hooge parameter decreases as the applied current increases for each applied field value tested. This is consistent with the Josephson junction array model. As the current increases, more of the junctions become resistive, thus increasing the effective volume and decreasing the normalized noise levels. The applied currents are not sufficiently small to rule out heating of the film, however the observed changes in α are not consistent with resistance changes due to heating. For example at 2500mT, as shown in figure 5.5, the sample resistance changes less than 3% from 100mK to 500mK, but α decreases by a factor of $\sim$300. Additionally, at an applied field of 5000mT, the resistance decreases dramatically as the temperature increases. From figure 5.21, it would be expected that α would increase as the resistance decreases. In

figure 5.22, it is clear that at 5000mT α decreases by almost an order of magnitude as the current increases. If heating was the dominant factor α should be increasing.

At high enough temperatures all the Josephson junctions are expected to be resistive and the normalized noise levels should be field and current independent since there are no more superconducting junctions to suppress. This can be seen in figures 5.23 and 5.24. Figure 5.23 shows α as a function of current at a temperature of 5.0K with zero applied magnetic field. From 10nA to 80nA of applied current α remains constant to within the standard error. Figure 5.24 shows α as a function of applied magnetic field. α doesn't remain constant within the standard error, but it does not seem to exhibit any systematic change. The values of α found at high temperature are lower than all but the highest resistance measurements done at low temperature, even though the resistance is considerably lower. The values are only slightly higher than those found in ordinary metals. This isn't surprising as the film should be in a metallic state by 5.0K, but is still more disordered than most metals.

The observed exponent value differs slightly from the prediction for p-model percolation. Any systematic deviation from the predicted value of 1.54 is likely due to the assumption of a two-state mixture, superconductor and metal, not perfectly representing the indium oxide system. In the low field regime on the superconducting side of the SIT the two-state system is a reasonably good assumption. In this regime the grains of the film are superconducting and the junctions between them are either superconducting or resistive. On the insulating side of the transition the system isn't strictly a mixture of metallic and insulating regions. There is substantial experimental evidence of superconducting regions persisting well into the insulating state.

Steiner and Kapitulnik [124] found evidence of superconductivity occurring above the critical field in indium oxide films exhibiting an SIT. A sign of superconductivity persisting into the insulating regime is the observation of a magnetoresistance peak,

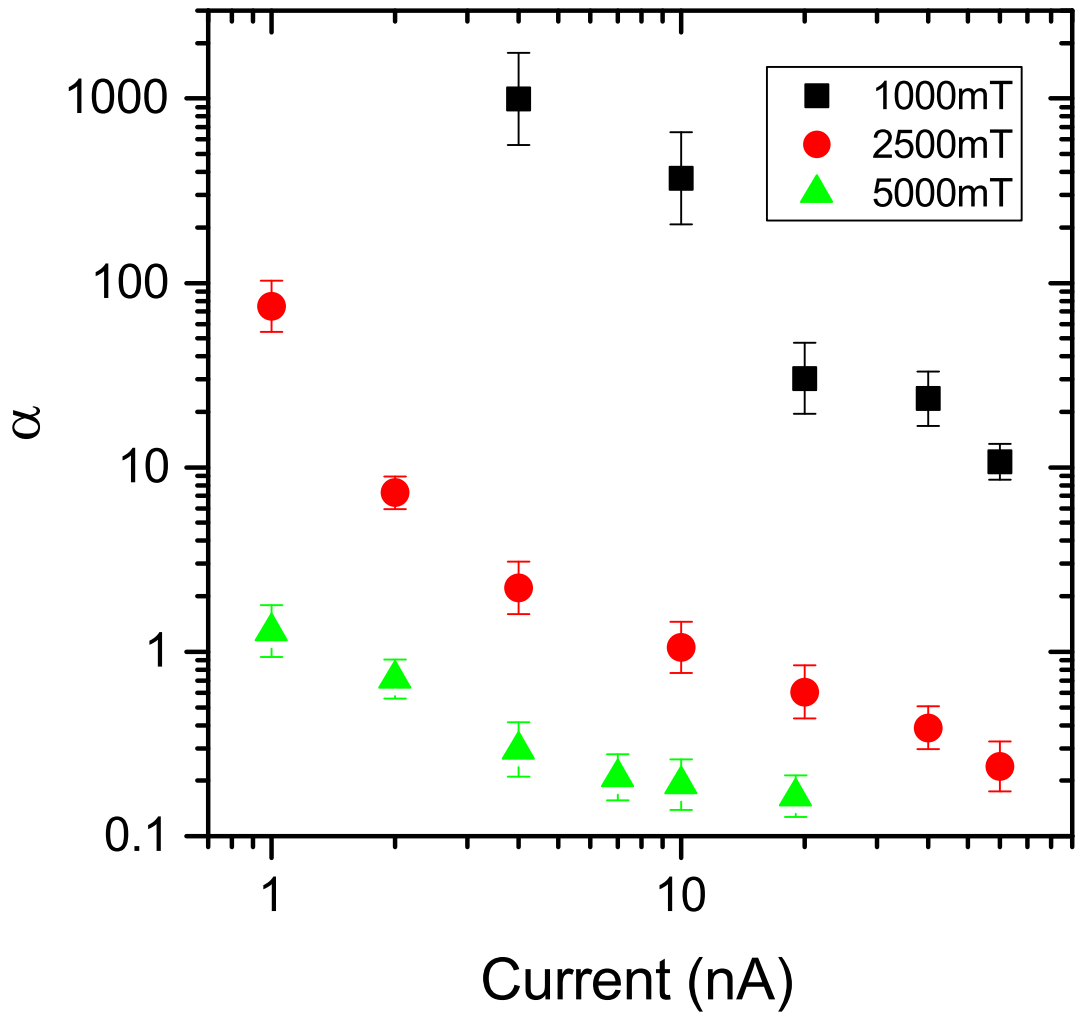

Figure 5.22: Log-log plot of α versus current for applied perpendicular magnetic fields of 1000, 2500, and 5000mT at a temperature of 100mK. For each field value, α decreases as the applied current increases.

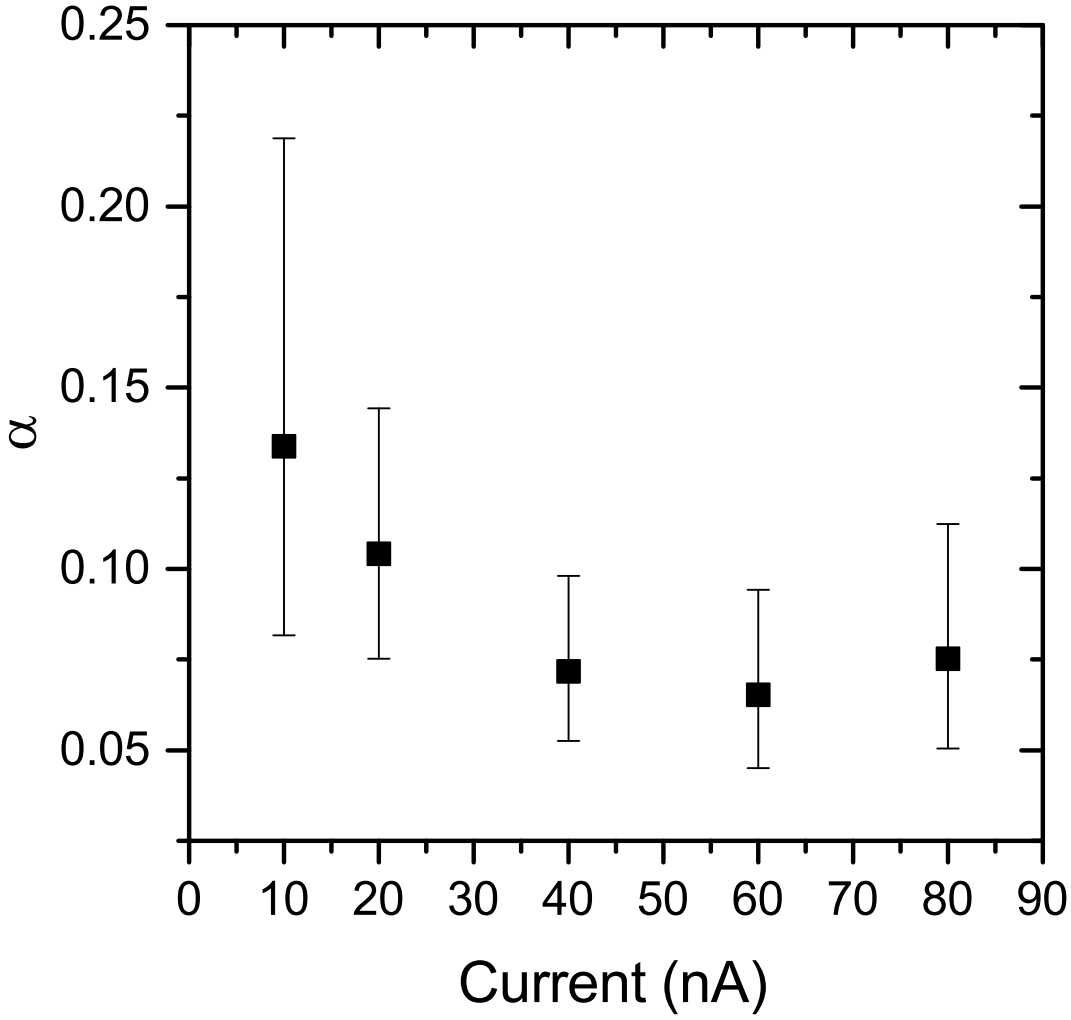

Figure 5.23: Plot of α as a function of applied current with zero applied field at a temperature of 5.0K.

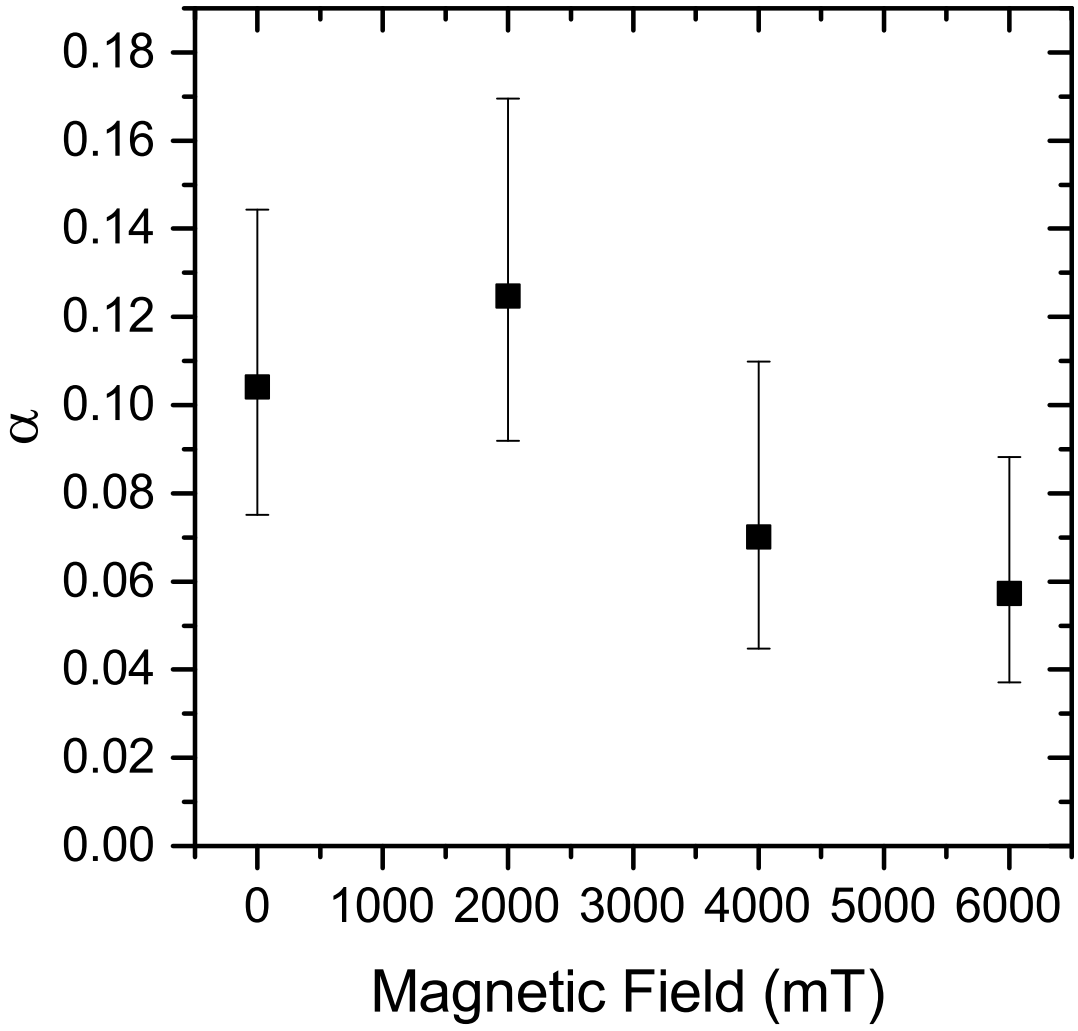

Figure 5.24: Plot of α versus applied magnetic field with 20nA sourced across the sample and a temperature of 5.0K.

similar to what was observed in this indium oxide film, as shown in figure 5.7. The peak is caused by the competition between the magnetic field driving the system further into the Bose-insulating phase and breaking up the Cooper pairs. They found that the resistivity still stayed well above the normal state resistance beyond the peak and interpreted this as evidence of Cooper pairs still being present. Additional evidence of this was found by looking at the characteristic activation energy. Direct evidence of Cooper pairs persisting into the insulating state was found by Sacepe et. al. [125] using scanning tunneling spectroscopy of amorphous indium oxide.

In high fields it seems likely that the assumption of a two-part mixture describing amorphous indium oxide films breaks down. It may be more reasonable to model the system as a three part mixture of superconductor, metal, and insulator. In this scenario only the metallic portion would contribute to the effective volume of the system contributing to the measured noise. In this case the effective volume would not increase as quickly as for the two part mixture since in high fields some of the regions where superconductivity is suppressed would be insulating and still not contribute to the effective volume. The more gradual increase in the effective volume would result in the normalized noise decreasing more gradually, resulting in a lower value of the noise exponent than would be expected for a two state mixture. This is consistent with what was observed.

The systematic deviation from linear behavior of α on the log-log plot shown in figure 5.16 in the region of highest resistance and lowest values could occur because of the crossover from a Bose-insulator to a fermionic system. In this regime, beyond the magnetoresistance peak, the fraction of the system volume that is resistive would increase as the resistance decreases. This would result in α decreasing as the resistance decreases. There are signs of this occurring in figure 5.16 when looking at the lowest values of α. These values of α were found when measured in applied fields of 6T and 7T

which are at and just beyond the magnetoresistance peak seen in figure 5.7. Stronger evidence of whether this is causing the broadening at high resistances would require extending the measurement to higher applied magnetic fields than were accessible with the K400.

There are also more subtle signs of α deviating from the expected behavior at lower resistance values than the obvious deviation seen at the highest resistance values in applied fields of 6T and 7T. Figure 5.25 is a plot of the derivative of plot 15, d[log(α)]/d[log(R)]. Therefore, the values in figure 5.25 correspond to the slope from figure 5.16, and thus the exponent value from equation 5.16. At lower fields these values are consistent with the slope of the best fit line, -1.33. At higher fields there is a significant broadening in the exponent values.

This broadening starts around 6590$\Omega/\square$. This is relatively close to the critical field from the scaling analysis, $\sim$5700 $\Omega/\square$. It is even closer to the theoretically predicted universal resistance for superconductor-insulator transitions that can be described by a percolation transition, which is $\sim$6450 $\Omega/\square$ [116]. This is suggestive of the p-model noise level prediction starting to breakdown on the insulating side of the transition. This would not be unexpected.

5.9 Conclusions

Extensive transport measurements were carried out on an amorphous indium oxide thin film. This film had the carrier concentration and disorder tuned such that it underwent a superconductor-insulator transition. The probable presence of a quantum phase transition was verified by performing a power-law scaling analysis. The resulting exponent product, νz=1.25$\pm$0.04, was similar to what Steiner et. al. [84] have reported for this system in the case of what they termed to be weak disorder. It is consistent with the transition being governed by classical percolation rather than quantum percolation.

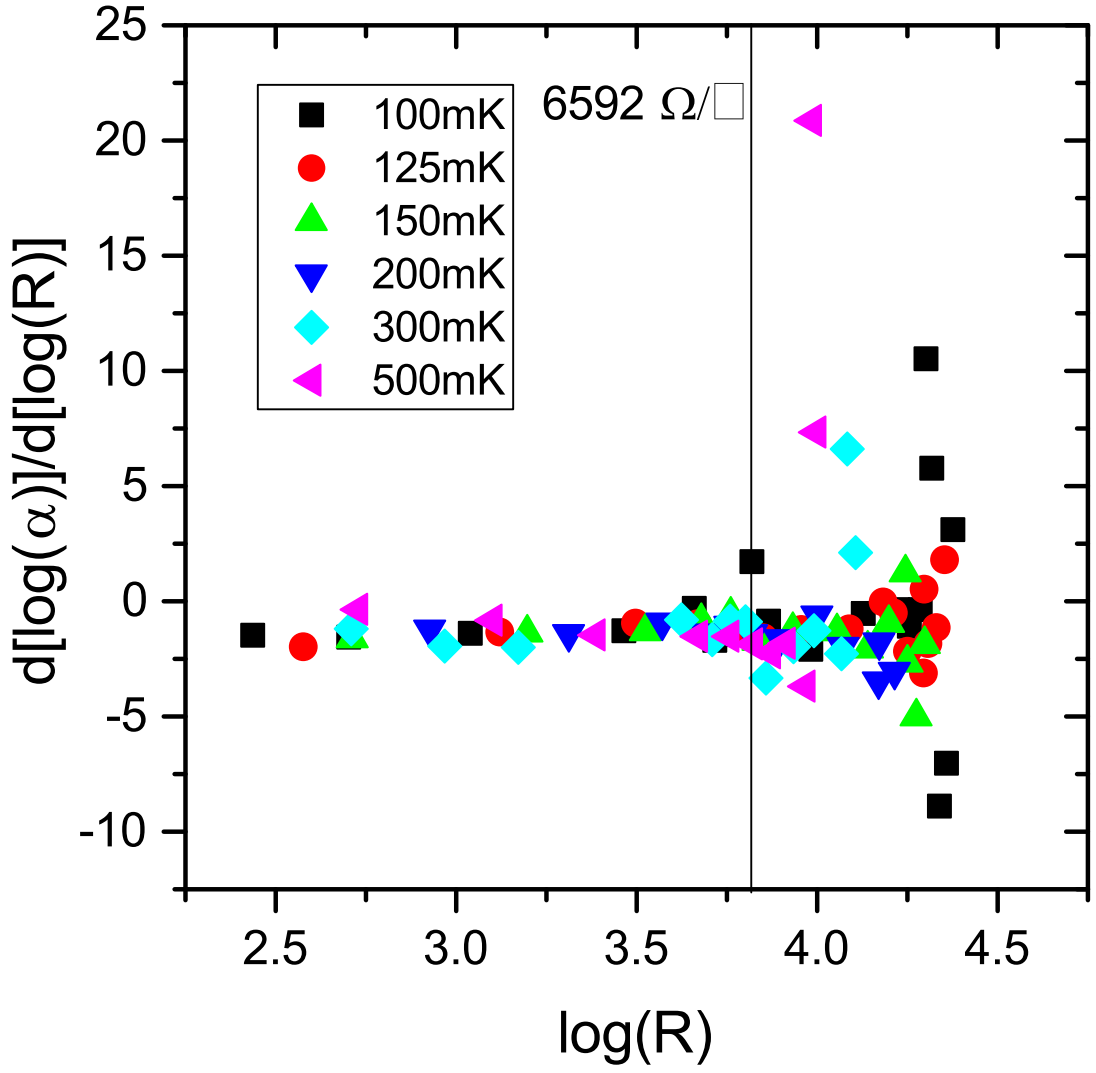

Figure 5.25: Plot of d[log(α)]/d[log(R)] versus log(R) corresponding to the exponent value -2/s from equation 5.16. The vertical line at 6592 Ω/□ is an estimate of where the broadening in the exponent value begins and is near the critical resistance for the SIT.

Additionally, resistance fluctuations exhibited by this film were measured extensively using a low-frequency measurement technique. These measurements were conducted as a function of applied perpendicular magnetic field and temperature. The nature of the fluctuations was analyzed by studying histograms of the resistance fluctuations, the power spectral density, and the second spectra.

Contrary to expectations, there was no significant change in the noise characteristics at the critical field for the SIT over the temperature range studied. The only subtle change that occurred near the SIT was increased uncertainty in the slope of α versus sheet resistance, indicated in figure 5.25. Additionally, there was only limited evidence for correlated fluctuations, and this occurred well into the insulating state, not near the transition, where the correlation length should diverge. This differs from what was found by Kremen et. al [77] in NbTiN films. They observed fluctuations that grew in size as the critical point was approached. This may be due to the significant disorder present in amorphous indium oxide films, compared to that of a typical metal.

Finally, the noise exponent determined from analyzing the corrected power spectra was within experimental uncertainty of the value predicted by Kiss and Svedlindh for a 2D system [114]. This strongly suggests that the percolation transition observed more closely followed p-model percolation than classical percolation, while possibly still being consistent with the scaling analysis predicting classical percolation over quantum percolation, since p-model percolation is a modification to classical percolation. The p-model is based on a random Josephson junction array with randomly switching junctions. Similar random Josephson junction array models have been used extensively to describe other transport properties of granular superconductors. Others have observed noise exponents consistent with this prediction in systems exhibiting superconductor-metal transitions or metal-insulator transitions, but this is the first example in an indium oxide film and the first example in a system undergoing a SIT.

Chapter 6

Conclusion

The magnetic-field-tuned superconductor-insulator transitions of disordered amorphous indium oxide films are a paradigm in the study of quantum phase transitions. These films commonly follow power-law scaling and it was the first system in which a magnetic-field tuned superconductor-insulator transition was observed. However, this is only one of many materials that are known to exhibit a quantum phase transition. Others such as TiN, underdoped $La_{2-x}Sr_xCuO_4$, and $LaAlO_3$/ $SrTiO_3$ interfaces [126, 127, 128], among others.

Amorphous indium oxide is of particular interest because it is one of the simplest systems to undergo a quantum phase transition, but also can exhibit a wide variety of behavior and is highly tunable. The methods that can be used to tune the properties of this material, such as deposition conditions and annealing, were discussed in detail in Chapter 2. The effects that tuning these parameters has on the type of phase transition that the system undergoes was discussed in Chapters 4 and 5.

In Chapter 4, a set of films that undergo a superconductor-metal transition and are believed to exhibit quantum Griffiths effects were discussed. The initial motivation for studying these films was an unusual smeared crossing of the magnetoresistance

isotherms. In the past films with similar smeared crossings were typically disregarded because it was believed to be the result of inhomogeneity of the film. While that can happen, and the conditions where that would be expected to happen were discussed, it was not the cause in this case. In this case it was shown to be the result of corrections to scaling.

In Chapter 5, a film that undergoes a more conventional superconductor-insulator transition was studied in detail. The resistance fluctuations and how they changed near the quantum critical point were of particular interest. Based on the work done by others [77] measuring the diamagnetic response of films near an SIT in conjunction with theory, it was expected that the size and time scale of the fluctuations would grow near the transition. The goal was to observe evidence of this using a much simpler measurement, resistance fluctuations, instead of a scanning SQUID. Surprisingly, no noteworthy changes in the characteristics of the noise were found near the critical point. Instead it was found that the changes in the resistance fluctuations were consistent with the transition being governed by percolation, specifically p-model percolation.

The very different behavior exhibited by amorphous indium oxide films in these two experiments is believed to be the result of differing degrees of disorder present in the two sets of films. The films that underwent a superconductor-metal transition have the lowest disorder and correspondingly the lowest normal state resistance, $\sim 1200\Omega/\square$. Films with moderate disorder underwent a superconductor-insulator transition and the transition was governed by a modified classical percolation model, called p-model percolation. These films had a normal state resistance of $\sim 6000\Omega/\square$. Films with even higher disorder are expected to exhibit quantum percolation. Hints of this were observed in another film that was briefly studied, but not discussed previously in this dissertation. It followed power-law scaling and had an exponent product value, $\nu z \approx 2.6$. This is in the vicinity of the value expected for quantum percolation, $\nu z = 7/3$. It had a normal

state resistance of $\sim$6500 $\Omega/\square$ indicating it was even more disordered than the films discussed in Chapters 4 and 5.

Connections between these various types of transitions have also been theoretically predicted. Dubi et. al. [129] have proposed a model connecting quantum percolation, classical percolation and superconductor-metal transitions. Their model is based on a tunable mixture of superconducting links, classical or incoherent links, and quantum tunneling links. Using this model they were able to predict a phase diagram with crossovers between the different transition types, depending on the fraction of links consisting of each type. This model may be applicable to indium oxide films with the links corresponding to coupling between grains of the film.

Future experiments on amorphous indium oxide could explore the ability to tune between the various types of transitions. Starting with a highly disordered film that exhibits quantum percolation, it may be possible to reduce the disorder through annealing and observe a crossover to another type of transition. Observing all three transitions, first a quantum percolation governed SIT, and then a classical percolation governed SIT, followed by a superconductor-metal transition governed by activated scaling, all in the same film could provide useful clues on how the three are connected.

It may also be of interest to study the noise properties of films exhibiting other types of transitions. Films with an infinite randomness fixed point may have different noise characteristics. Additionally, it may be possible to test the prediction of Green et. al [75] of Johnson noise like behavior with an elevated effective temperature. The Scofield method would not be useful for such an experiment, but mounting a low temperature pre-amplifier at the mixing chamber of the dilution refrigerator may make it possible to observe this effect, if it does occur.

Lastly, it would be interesting to observe another superconducting system with a transition following activated scaling instead of power-law scaling. As was discussed in

Chapter 4, there are several other examples of systems that appear to exhibit quantum Griffiths effects and an infinite randomness fixed point. These systems have been shown to likely have a diverging exponent product, but none have been shown to follow activated scaling.

References

[1] Michael Tinkham. *Introduction to Superconductivity*. Courier Corporation, 2012.

[2] J. File and R. G. Mills. Observation of persistent current in a superconducting solenoid. *Phys. Rev. Lett.*, 10:93–96, Feb 1963.

[3] H Kamerlingh Onnes. Leiden comm. 120b, 122b. Technical report, 124c, 1911.

[4] Elliot Snider, Nathan Dasenbrock-Gammon, Raymond McBride, Xiaoyu Wang, Noah Meyers, Keith V. Lawler, Eva Zurek, Ashkan Salamat, and Ranga P. Dias. Synthesis of yttrium superhydride superconductor with a transition temperature up to 262 k by catalytic hydrogenation at high pressures. *Phys. Rev. Lett.*, 126:117003, Mar 2021.

[5] J. Bardeen, L. N. Cooper, and J. R. Schrieffer. Theory of superconductivity. *Phys. Rev.*, 108:1175–1204, Dec 1957.

[6] C. C. Tsuei and J. R. Kirtley. Pairing symmetry in cuprate superconductors. *Rev. Mod. Phys.*, 72:969–1016, Oct 2000.

[7] A. D. Hillier, J. Quintanilla, B. Mazidian, J. F. Annett, and R. Cywinski. Nonunitary triplet pairing in the centrosymmetric superconductor laniga$_2$. *Phys. Rev. Lett.*, 109:097001, Aug 2012.

[8] Daniel Schroeder. *An Introduction To Thermal Physics*. Oxford University Press, 1999.

[9] Yen-Hsiang Lin, J. Nelson, and A.M. Goldman. Superconductivity of very thin films: The superconductor–insulator transition. *Physica C: Superconductivity and its Applications*, 514:130–141, 2015. Superconducting Materials: Conventional, Unconventional and Undetermined.

[10] Durham emergence project : Fellowship - durham university, https://www.dur.ac.uk/emergence/fellowships/xiao/.

[11] S. L. Sondhi, S. M. Girvin, J. P. Carini, and D. Shahar. Continuous quantum phase transitions. *Rev. Mod. Phys.*, 69:315–333, Jan 1997.

[12] Josephson junction - thin film deposition for superconducting circuits, https://angstromengineering.com/josephson-junction-thin-film-deposition-superconducting-circuits/.

[13] B.D. Josephson. Possible new effects in superconductive tunnelling. *Physics Letters*, 1(7):251–253, 1962.

[14] B. Abeles. Effect of charging energy on superconductivity in granular metal films. *Phys. Rev. B*, 15:2828–2829, Mar 1977.

[15] Enzo Granato and J. M. Kosterlitz. Superconductor-insulator transition and universal resistance in josephson-junction arrays in a magnetic field. *Phys. Rev. Lett.*, 65:1267–1270, Sep 1990.

[16] Kevin A. Parendo, K. H. Sarwa B. Tan, and A. M. Goldman. Evolution towards superconductivity in granular films of bismuth. *Phys. Rev. B*, 76:100508, Sep 2007.

[17] A. F. Hebard and M. A. Paalanen. Magnetic-field-tuned superconductor-insulator transition in two-dimensional films. *Phys. Rev. Lett.*, 65:927–930, Aug 1990.

[18] Wei Xie, Xin Zhang, Chris Leighton, and C. Daniel Frisbie. 2d insulator–metal transition in aerosol-jet-printed electrolyte-gated indium oxide thin film transistors. *Advanced Electronic Materials*, 3(3):1600369, 2017, https://onlinelibrary.wiley.com/doi/pdf/10.1002/aelm.201600369.

[19] Ilana M. Percher, Irina Volotsenko, Aviad Frydman, Boris I. Shklovskii, and Allen M. Goldman. Vortex variable range hopping in a conventional superconducting film. *Phys. Rev. B*, 96:224511, Dec 2017.

[20] Z. Ovadyahu. Slow dynamics of electron glasses: The role of disorder. *Phys. Rev. B*, 95:134203, Apr 2017.

[21] U. Givan and Z. Ovadyahu. Compositional disorder and transport peculiarities in the amorphous indium oxides. *Phys. Rev. B*, 86:165101, Oct 2012.

[22] J. R. Bellingham, A. P. Mackenzie, and W. A. Phillips. Precise measurements of oxygen content: Oxygen vacancies in transparent conducting indium oxide films. *Applied Physics Letters*, 58(22):2506–2508, 1991, https://doi.org/10.1063/1.104858.

[23] Yeonbae Lee, Aviad Frydman, Tianran Chen, Brian Skinner, and A. M. Goldman. Electrostatic tuning of the properties of disordered indium-oxide films near the superconductor-insulator transition. *Phys. Rev. B*, 88:024509, Jul 2013.

[24] B. Sacépé, C. Chapelier, T. I. Baturina, V. M. Vinokur, M. R. Baklanov, and M. Sanquer. Disorder-induced inhomogeneities of the superconducting state close to the superconductor-insulator transition. *Phys. Rev. Lett.*, 101:157006, Oct 2008.

[25] Karim Bouadim, Yen Lee Loh, Mohit Randeria, and Nandini Trivedi. Single- and two-particle energy gaps across the disorder-driven superconductor–insulator transition. *Nature Physics*, 7(11):884–889, Nov 2011.

[26] Nandini Trivedi, Yen Lee Loh, Karim Bouadim, and Mohit Randeria. Emergent granularity and pseudogap near the superconductor-insulator transition. *Journal of Physics: Conference Series*, 376:012001, jul 2012.

[27] Z Ovadyahu. Some finite temperature aspects of the anderson transition. *Journal of Physics C: Solid State Physics*, 19(26):5187–5213, sep 1986.

[28] J. Pearl. Current distribution in superconducting films carrying quantized fluxoids. *Applied Physics Letters*, 5, Jun 1964.

[29] M. R. Beasley, J. E. Mooij, and T. P. Orlando. Possibility of vortex-antivortex pair dissociation in two-dimensional superconductors. *Phys. Rev. Lett.*, 42:1165–1168, Apr 1979.

[30] Boris L. Altshuler, Vladimir E. Kravtsov, Igor V. Lerner, and Igor L. Aleiner. Jumps in current-voltage characteristics in disordered films. *Phys. Rev. Lett.*, 102:176803, Apr 2009.

[31] B. Huard, H. Pothier, D. Esteve, and K. E. Nagaev. Electron heating in metallic resistors at sub-kelvin temperature. *Phys. Rev. B*, 76:165426, Oct 2007.

[32] T. Levinson, A. Doron, I. Tamir, G. C. Tewari, and D. Shahar. Direct determination of the temperature of overheated electrons in an insulator. *Phys. Rev. B*, 94:174204, Nov 2016.

[33] I. Tamir, A. Benyamini, E. J. Telford, F. Gorniaczyk, A. Doron, T. Levinson, D. Wang, F. Gay, B. Sacépé, J. Hone, K. Watanabe, T. Taniguchi,

C. R. Dean, A. N. Pasupathy, and D. Shahar. Sensitivity of the superconducting state in thin films. *Science Advances*, 5(3), 2019, https://advances.sciencemag.org/content/5/3/eaau3826.full.pdf.

[34] Ahmed K Ibrahim. *Disorder at First-Order Classical and Quantum Phase Transitions*. PhD thesis, 2018.

[35] V. F. Gantmakher, M. V. Golubkov, V. T. Dolgopolov, G. E. Tsydynzhapov, and A. A. Shashkin. Scaling analysis of the magnetic field-tuned quantum transition in superconducting amorphous in-o films. *Journal of Experimental and Theoretical Physics Letters*, 71(4):160–164, Feb 2000.

[36] Robert B. Griffiths. Nonanalytic behavior above the critical point in a random ising ferromagnet. *Phys. Rev. Lett.*, 23:17–19, Jul 1969.

[37] Thomas Vojta. Quantum griffiths effects and smeared phase transitions in metals: Theory and experiment. *Journal of Low Temperature Physics*, 161(1):299–323, Oct 2010.

[38] Thomas Vojta and Jörg Schmalian. Quantum griffiths effects in itinerant heisenberg magnets. *Phys. Rev. B*, 72:045438, Jul 2005.

[39] José A. Hoyos, Chetan Kotabage, and Thomas Vojta. Effects of dissipation on a quantum critical point with disorder. *Phys. Rev. Lett.*, 99:230601, Dec 2007.

[40] Thomas Vojta, Chetan Kotabage, and José A. Hoyos. Infinite-randomness quantum critical points induced by dissipation. *Phys. Rev. B*, 79:024401, Jan 2009.

[41] Daniel S. Fisher. Critical behavior of random transverse-field ising spin chains. *Phys. Rev. B*, 51:6411–6461, Mar 1995.

[42] Thomas Vojta, Adam Farquhar, and Jason Mast. Infinite-randomness critical point in the two-dimensional disordered contact process. *Phys. Rev. E*, 79:011111, Jan 2009.

[43] István A. Kovács and Ferenc Iglói. Critical behavior and entanglement of the random transverse-field ising model between one and two dimensions. *Phys. Rev. B*, 80:214416, Dec 2009.

[44] C. L. Seaman, M. B. Maple, B. W. Lee, S. Ghamaty, M. S. Torikachvili, J.-S. Kang, L. Z. Liu, J. W. Allen, and D. L. Cox. Evidence for non-fermi liquid behavior in the kondo alloy $y_{1-x}u_xpd_3$. *Phys. Rev. Lett.*, 67:2882–2885, Nov 1991.

[45] Ying Xing, Hui-Min Zhang, Hai-Long Fu, Haiwen Liu, Yi Sun, Jun-Ping Peng, Fa Wang, Xi Lin, Xu-Cun Ma, Qi-Kun Xue, Jian Wang, and X. C. Xie. Quantum griffiths singularity of superconductor-metal transition in ga thin films. *Science*, 350(6260):542–545, 2015, https://science.sciencemag.org/content/350/6260/542.full.pdf.

[46] Yu Saito, Tsutomu Nojima, and Yoshihiro Iwasa. Quantum phase transitions in highly crystalline two-dimensional superconductors. *Nature Communications*, 9(1):778, Feb 2018.

[47] Shengchun Shen, Ying Xing, Pengjie Wang, Haiwen Liu, Hailong Fu, Yangwei Zhang, Lin He, X. C. Xie, Xi Lin, Jiacai Nie, and Jian Wang. Observation of quantum griffiths singularity and ferromagnetism at the superconducting $LaAlo_3/SrTio_3(110)$ interface. *Phys. Rev. B*, 94:144517, Oct 2016.

[48] Yi Liu, Ziqiao Wang, Pujia Shan, Yue Tang, Chaofei Liu, Cheng Chen, Ying Xing, Qingyan Wang, Haiwen Liu, Xi Lin, X. C. Xie, and Jian Wang. Anomalous

quantum griffiths singularity in ultrathin crystalline lead films. *Nature Communications*, 10(1):3633, Aug 2019.

[49] Enze Zhang, Jinhua Zhi, Yi-Chao Zou, Zefang Ye, Linfeng Ai, Jiacheng Shi, Ce Huang, Shanshan Liu, Zehao Lin, Xinyuan Zheng, Ning Kang, Hongqi Xu, Wei Wang, Liang He, Jin Zou, Jinyu Liu, Zhiqiang Mao, and Faxian Xiu. Signature of quantum griffiths singularity state in a layered quasi-one-dimensional superconductor. *Nature Communications*, 9(1):4656, Nov 2018.

[50] Yi Liu, Yong Xu, Jian Sun, Chong Liu, Yanzhao Liu, Chong Wang, Zetao Zhang, Kaiyuan Gu, Yue Tang, Cui Ding, and et al. Type-ii ising superconductivity and anomalous metallic state in macro-size ambient-stable ultrathin crystalline films. *Nano Letters*, 20(8):5728–5734, Jun 2020.

[51] Nicholas P. Breznay, Mihir Tendulkar, Li Zhang, Sang-Chul Lee, and Aharon Kapitulnik. Superconductor to weak-insulator transitions in disordered tantalum nitride films. *Phys. Rev. B*, 96:134522, Oct 2017.

[52] Chao Zhang, Yunjie Fan, Qiaoling Chen, Tianyi Wang, Xiang Liu, Qi Li, Yuewei Yin, and Xiaoguang Li. Quantum griffiths singularities in tio superconducting thin films with insulating normal states. *NPG Asia Materials*, 11(1):76, Dec 2019.

[53] Xiaofu Zhang, Adriana E. Lita, Huanlong Liu, Varun B. Verma, Qiang Zhou, Sae Woo Nam, and Andreas Schilling. Size dependent nature of the magnetic-field driven superconductor-to-insulator quantum-phase transitions. *Communications Physics*, 4(1):100, May 2021.

[54] L. J. van der Pauw. A method of measuring specific resistivity and hall effect of discs of arbitrary shape. *Philips Research Reports*, 13(1), Feb 1958.

[55] B L Altshuler, A G Aronov, and D E Khmelnitsky. Effects of electron-electron collisions with small energy transfers on quantum localisation. *Journal of Physics C: Solid State Physics*, 15(36):7367–7386, Dec 1982.

[56] B Kramer and A MacKinnon. Localization: theory and experiment. *Reports on Progress in Physics*, 56(12):1469–1564, Dec 1993.

[57] Nicholas A. Lewellyn, Ilana M. Percher, JJ Nelson, Javier Garcia-Barriocanal, Irina Volotsenko, Aviad Frydman, Thomas Vojta, and Allen M. Goldman. Infinite-randomness fixed point of the quantum superconductor-metal transitions in amorphous thin films. *Phys. Rev. B*, 99:054515, Feb 2019.

[58] Brian Skinner, Jonathan Ruhman, and Adam Nahum. Measurement-induced phase transitions in the dynamics of entanglement. *Phys. Rev. X*, 9:031009, Jul 2019.

[59] Julia E. Medvedeva, D. Bruce Buchholz, and Robert P. H. Chang. Recent advances in understanding the structure and properties of amorphous oxide semiconductors. *Advanced Electronic Materials*, 3(9):1700082, 2017, https://onlinelibrary.wiley.com/doi/pdf/10.1002/aelm.201700082.

[60] Aharon Kapitulnik, Steven A. Kivelson, and Boris Spivak. Colloquium: Anomalous metals: Failed superconductors. *Rev. Mod. Phys.*, 91:011002, Jan 2019.

[61] B. Spivak, P. Oreto, and S. A. Kivelson. Theory of quantum metal to superconductor transitions in highly conducting systems. *Phys. Rev. B*, 77:214523, Jun 2008.

[62] Emanuele G. Dalla Torre, Eugene Demler, Thierry Giamarchi, and Ehud Altman. Quantum critical states and phase transitions in the presence of non-equilibrium noise. *Nature Physics*, 6(10):806–810, Oct 2010.

[63] Birger Horstmann, J. Ignacio Cirac, and Géza Giedke. Noise-driven dynamics and phase transitions in fermionic systems. *Phys. Rev. A*, 87:012108, Jan 2013.

[64] Alexander A. Balandin. Low-frequency 1/f noise in graphene devices. *Nature Nanotechnology*, 8(8):549–555, Aug 2013.

[65] C. M. Knoedler and Richard F. Voss. Voltage noise measurement of the vortex mean free path in superconducting granular tin films. *Phys. Rev. B*, 26:449–451, Jul 1982.

[66] N. W. Carlson, A. J. Taylor, and A. L. Schawlow. Identification of rydberg states in na_2 by two-step polarization labeling. *Phys. Rev. Lett.*, 45:18–21, Jul 1980.

[67] John H. Scofield, Joseph V. Mantese, and Watt W. Webb. 1/f noise of metals: A case for extrinsic origin. *Phys. Rev. B*, 32:736–742, Jul 1985.

[68] Gopi Nath Daptary, Shelender Kumar, Pramod Kumar, Anjana Dogra, N. Mohanta, A. Taraphder, and Aveek Bid. Correlated non-gaussian phase fluctuations in $laalo_3/srtio_3$ heterointerfaces. *Phys. Rev. B*, 94:085104, Aug 2016.

[69] S. L. Ginzburg and N. E. Savitskaya. Self-organization and 1/f noise in granular superconductors. *Journal of Experimental and Theoretical Physics Letters*, 73(5):209–213, Mar 2001.

[70] Amrit De. Noise from glauber dynamics: Self-consistent interaction and temperature dependent correlations. *Advances in Condensed Matter Physics*, 2015:607021, Jan 2015.

[71] Emanuele G Dalla Torre, Eugene Demler, Thierry Giamarchi, and Ehud Altman. Noisy quantum phase transitions: an intuitive approach. *Physica Scripta*, T151:014026, nov 2012.

[72] Oded Cohen and Zvi Ovadyahu. 1/f noise near the metal-insulator transition. *International Journal of Modern Physics B*, 08(07):897–903, 1994, https://doi.org/10.1142/S0217979294000440.

[73] I. Tamir, T. Levinson, F. Gorniaczyk, A. Doron, J. Lieb, and D. Shahar. Excessive noise as a test for many-body localization. *Phys. Rev. B*, 99:035135, Jan 2019.

[74] I. Raičević, Dragana Popović, C. Panagopoulos, and T. Sasagawa. Non-gaussian noise in the in-plane transport of lightly doped $la_{2-x}sr_xcuo_4$: Evidence for a collective state of charge clusters. *Phys. Rev. B*, 83:195133, May 2011.

[75] A. G. Green, J. E. Moore, S. L. Sondhi, and A. Vishwanath. Current noise in the vicinity of the 2d superconductor-insulator quantum critical point. *Phys. Rev. Lett.*, 97:227003, Dec 2006.

[76] Zhi Chen and Clare C. Yu. Measurement-noise maximum as a signature of a phase transition. *Phys. Rev. Lett.*, 98:057204, Jan 2007.

[77] A. Kremen, H. Khan, Y. L. Loh, T. I. Baturina, N. Trivedi, A. Frydman, and B. Kalisky. Imaging quantum fluctuations near criticality. *Nature Physics*, 14(12):1205–1210, Dec 2018.

[78] Dennis V. Perepelitsa. Johnson noise and shot noise. Nov 2006.

[79] Per Bak, Chao Tang, and Kurt Wiesenfeld. Self-organized criticality: An explanation of the 1/f noise. *Phys. Rev. Lett.*, 59:381–384, Jul 1987.

[80] O. Cohen, Z. Ovadyahu, and M. Rokni. 1/f noise and incipient localization. *Phys. Rev. Lett.*, 69:3555–3558, Dec 1992.

[81] S. R. Broadbent and J. M. Hammersley. Percolation processes: I. crystals and mazes. *Mathematical Proceedings of the Cambridge Philosophical Society*, 53(3):629–641, 1957.

[82] *Electronic Properties of Doped Semiconductors*. Springer, 1979.

[83] Y. Avishai and J. M. Luck. Quantum percolation and ballistic conductance on a lattice of wires. *Phys. Rev. B*, 45:1074–1095, Jan 1992.

[84] Myles A. Steiner, Nicholas P. Breznay, and Aharon Kapitulnik. Approach to a superconductor-to-bose-insulator transition in disordered films. *Phys. Rev. B*, 77:212501, Jun 2008.

[85] A L Efros and B I Shklovskii. Coulomb gap and low temperature conductivity of disordered systems. *Journal of Physics C: Solid State Physics*, 8(4):L49–L51, feb 1975.

[86] E. Bielejec and Wenhao Wu. Field-tuned superconductor-insulator transition with and without current bias. *Phys. Rev. Lett.*, 88:206802, May 2002.

[87] N. Marković, C. Christiansen, A. M. Mack, W. H. Huber, and A. M. Goldman. Superconductor-insulator transition in two dimensions. *Phys. Rev. B*, 60:4320–4328, Aug 1999.

[88] Nobuhito Kokubo, Takahisa Terashima, and Satoshi Okuma. Voltage noise of an amorphous $\mathrm{mo}_x\mathrm{si}_{1-x}$ film near the superconducting transition in magnetic fields. *Journal of the Physical Society of Japan*, 67(3):725–728, 1998, https://doi.org/10.1143/JPSJ.67.725.

[89] Matthew P. A. Fisher, G. Grinstein, and S. M. Girvin. Presence of quantum diffusion in two dimensions: Universal resistance at the superconductor-insulator transition. *Phys. Rev. Lett.*, 64:587–590, Jan 1990.

[90] N. Mason and A. Kapitulnik. Dissipation effects on the superconductor-insulator transition in 2d superconductors. *Phys. Rev. Lett.*, 82:5341–5344, Jun 1999.

[91] John H. Scofield. ac method for measuring low-frequency resistance fluctuation spectra. *Review of Scientific Instruments*, 58(6):985–993, 1987, https://doi.org/10.1063/1.1139587.

[92] Gopi Nath Daptary, Hemanta Kumar Kundu, John Jesudasan, Pramod Kumar, Anjana Dogra, Pratap Raychaudhuri, R. C. Budhani, and Aveek Bid. Resistance fluctuations near the berezinskii-kosterlitz-thouless transition temperature in low dimensional superconductors. In *2015 International Conference on Noise and Fluctuations (ICNF)*, pages 1–4, 2015.

[93] J. Jaroszyński, Dragana Popović, and T. M. Klapwijk. Universal behavior of the resistance noise across the metal-insulator transition in silicon inversion layers. *Phys. Rev. Lett.*, 89:276401, Dec 2002.

[94] *MODEL SR560 LOW-NOISE PREAMPLIFIER.*

[95] Arindam Ghosh, Ayan Guha, and Arup Kumar Raychaudhuri. Low-frequency conductance fluctuations in a shape memory alloy near the martensite transition. In Dragana Popovic, Michael B. Weissman, and Zoltan A. Racz, editors, *Fluctuations and Noise in Materials*, volume 5469, pages 51 – 60. International Society for Optics and Photonics, SPIE, 2004.

[96] Arindam Ghosh, S. Kar, A. Bid, and A. Raychaudhuri. A set-up for measurement of low frequency conductance fluctuation (noise) using digital signal processing techniques. *arXiv: Other Condensed Matter*, 2004.

[97] R. Koushik, Siddhartha Kumar, Kazi Rafsanjani Amin, Mintu Mondal, John Jesudasan, Aveek Bid, Pratap Raychaudhuri, and Arindam Ghosh. Correlated conductance fluctuations close to the berezinskii-kosterlitz-thouless transition in ultrathin nbn films. *Phys. Rev. Lett.*, 111:197001, Nov 2013.

[98] Thierry Giamarchi and Pierre Le Doussal. Elastic theory of flux lattices in the presence of weak disorder. *Phys. Rev. B*, 52:1242–1270, Jul 1995.

[99] T. Giamarchi and P. Le Doussal. Phase diagrams of flux lattices with disorder. *Phys. Rev. B*, 55:6577–6583, Mar 1997.

[100] Jonathan Pelz and John Clarke. Dependence of $\frac{1}{f}$ noise on defects induced in copper films by electron irradiation. *Phys. Rev. Lett.*, 55:738–741, Aug 1985.

[101] Sh. Kogan. *Electronic Noise and Fluctuations in Solids*. Cambridge University Press, 1996.

[102] Dietrich Stauffer and Amnon Aharony. *Introduction to Percolation Theory*. Taylor and Francis, 2010.

[103] Alexander Gerber and Guy Deutscher. Superconducting properties of in-ge mixture films. *Phys. Rev. B*, 35:3214–3218, Mar 1987.

[104] R. Rammal, C. Tannous, P. Breton, and A. M. S. Tremblay. Flicker ($\frac{1}{f}$) noise in percolation networks: A new hierarchy of exponents. *Phys. Rev. Lett.*, 54:1718–1721, Apr 1985.

[105] B Nienhuis. Analytical calculation of two leading exponents of the dilute potts model. *Journal of Physics A: Mathematical and General*, 15(1):199–213, jan 1982.

[106] D. W. Heermann and D. Stauffer. Phase diagram for three-dimensional correlated site-bond percolation. *Zeitschrift für Physik B Condensed Matter*, 44(4):339–344, Dec 1981.

[107] H. J. Herrmann, B. Derrida, and J. Vannimenus. Superconductivity exponents in two- and three-dimensional percolation. *Phys. Rev. B*, 30:4080–4082, Oct 1984.

[108] J. G. Zabolitzky. Monte carlo evidence against the alexander-orbach conjecture for percolation conductivity. *Phys. Rev. B*, 30:4077–4079, Oct 1984.

[109] C. J. Lobb and D. J. Frank. Percolative conduction and the alexander-orbach conjecture in two dimensions. *Phys. Rev. B*, 30:4090–4092, Oct 1984.

[110] Derrida, B., Stauffer, D., Herrmann, H.J., and Vannimenus, J. Transfer matrix calculation of conductivity in three-dimensional random resistor networks at percolation threshold. *J. Physique Lett.*, 44(17):701–706, 1983.

[111] David C. Wright, David J. Bergman, and Yacov Kantor. Resistance fluctuations in random resistor networks above and below the percolation threshold. *Phys. Rev. B*, 33:396–401, Jan 1986.

[112] J. M. NORMAND and H. J. HERRMANN. Precise numerical determination of the superconducting exponent of percolation in three dimensions. *International Journal of Modern Physics C*, 01(02n03):207–214, 1990, https://doi.org/10.1142/S0129183190000116.

[113] P. M. Hui and D. Stroud. Noise exponent in superconducting-normal metal mixtures. *Phys. Rev. B*, 34:8101–8103, Dec 1986.

[114] L. B. Kiss and P. Svedlindh. New noise exponents in random conductor-superconductor and conductor-insulator mixtures. *Phys. Rev. Lett.*, 71:2817–2820, Oct 1993.

[115] G. Deutscher, Y. Imry, and L. Gunther. Superconducting phase transitions in granular systems. *Phys. Rev. B*, 10:4598–4606, Dec 1974.

[116] B. G. Orr, H. M. Jaeger, A. M. Goldman, and C. G. Kuper. Global phase coherence in two-dimensional granular superconductors. *Phys. Rev. Lett.*, 56:378–381, Jan 1986.

[117] A. Frydman, O. Naaman, and R. C. Dynes. Universal transport in two-dimensional granular superconductors. *Phys. Rev. B*, 66:052509, Aug 2002.

[118] L.B. Kiss and P. Svedlindh. Noise in high t_c superconductors. *IEEE Transactions on Electron Devices*, 41(11):2112–2122, 1994.

[119] L.B. Kiss, T. Larsson, P. Svedlindh, L. Lundgren, H. Ohlsén, M. Ottosson, J. Hudner, and L. Stolt. Conductance noise and percolation in $yba_2cu_3o_7$ thin films. *Physica C: Superconductivity*, 207(3):318–332, 1993.

[120] Jens Müller and Tatjana Thomas. Low-frequency dynamics of strongly correlated electrons in (bedt-ttf)2x studied by fluctuation spectroscopy. *Crystals*, 8(4), 2018.

[121] Tathagata Paul, Subhamoy Ghatak, and Arindam Ghosh. Percolative switching in transition metal dichalcogenide field-effect transistors at room temperature. *Nanotechnology*, 27(12):125706, feb 2016.

[122] C. Barone, F. Romeo, S. Pagano, M. Adamo, C. Nappi, E. Sarnelli, F. Kurth, and K. Iida. Probing transport mechanisms of bafe2as2 superconducting films

and grain boundary junctions by noise spectroscopy. *Scientific Reports*, 4(1):6163, Aug 2014.

[123] C. Barone, S. Pagano, I. Pallecchi, E. Bellingeri, M. Putti, and C. Ferdeghini. Thermal and voltage activated excess $1/f$ noise in $\mathrm{fete_{0.5}se_{0.5}}$ epitaxial thin films. *Phys. Rev. B*, 83:134523, Apr 2011.

[124] Myles Steiner and Aharon Kapitulnik. Superconductivity in the insulating phase above the field-tuned superconductor–insulator transition in disordered indium oxide films. *Physica C: Superconductivity*, 422(1):16–26, 2005.

[125] Benjamin Sacépé, Thomas Dubouchet, Claude Chapelier, Marc Sanquer, Maoz Ovadia, Dan Shahar, Mikhail Feigel'man, and Lev Ioffe. Localization of preformed cooper pairs in disordered superconductors. *Nature Physics*, 7(3):239–244, Mar 2011.

[126] M. M. Mehta, D. A. Dikin, C. W. Bark, S. Ryu, C. M. Folkman, C. B. Eom, and V. Chandrasekhar. Magnetic field tuned superconductor-to-insulator transition at the $\mathrm{laalo_3/srtio_3}$ interface. *Phys. Rev. B*, 90:100506, Sep 2014.

[127] T. I. Baturina, D. R. Islamov, J. Bentner, C. Strunk, M. R. Baklanov, and A. Satta. Superconductivity on the localization threshold and magnetic-field-tuned superconductor-insulator transition in tin films. *Journal of Experimental and Theoretical Physics Letters*, 79(7):337–341, Apr 2004.

[128] Xiaoyan Shi, Ping V. Lin, T. Sasagawa, V. Dobrosavljević, and Dragana Popović. Two-stage magnetic-field-tuned superconductor–insulator transition in underdoped $\mathrm{la_{2\mathit{x}}sr_{\mathit{x}}cuo_4}$. *Nature Physics*, 10(6):437–443, Jun 2014.

[129] Yonatan Dubi, Yigal Meir, and Yshai Avishai. Unifying model for several classes of two-dimensional phase transition. *Phys. Rev. Lett.*, 94:156406, Apr 2005.

Appendices

In this appendix we provide a derivation of Eq. 4.6, and a discussion of the effect of corrections to scaling. For simplicity, we first consider the case without corrections to scaling. Including such corrections is straight forward and does not change the results qualitatively. The standard power-law scaling form of the resistance at a magnetic-field-tuned transition is given by

$$R\left(\delta,T\right)=\Phi\left(\delta T^{-\frac{1}{\nu z}}\right) \tag{1}$$

where Φ is the scaling function, ν is the correlation length exponent, z is the dynamical critical exponent, and $\delta=\left|B-B_c\right|/B_c$ measures the distance from the critical field B_c. The critical resistance, $R_c=R(0,T)=\Phi(0)$. Curves of R vs. δ at different temperatures cross at $\delta=0$. Now consider the slope of the resistance w.r.t. δ,

$$S(T)=\left.\frac{\partial R}{\partial\delta}\right|_{\delta=0}=T^{-1/\nu z}\ \Phi'(0) \tag{2}$$

from which it follows that

$$\frac{1}{\nu z}=-\frac{d\ln S}{d\ln T} \tag{3}$$

This value will be independent of T as long as there are no corrections to scaling.

We now turn to activated scaling as expected for the random transverse field Ising model. The scaling form of the resistance is given by

$$R\left(\delta,\ln\frac{T_0}{T}\right)=\Phi\left[\delta\left(\ln\frac{T_0}{T}\right)^{\frac{1}{\nu\psi}}\right] \tag{4}$$

Here, ψ is the tunneling exponent. Note that at $\delta=0$, this form predicts a single-valued critical resistance R_c, i.e. a single crossing point for isotherms. To find the exponent product $\nu\psi$, one can repeat the procedure used for power-law scaling,

$$S(T)=\left.\frac{\partial R}{\partial\delta}\right|_{\delta=0}=\left(\ln\frac{T_0}{T}\right)^{\frac{1}{\nu\psi}}\phi'(0) \tag{5}$$

Thus, $S(T)$ behaves as a power of $\ln\left(T_0/T\right)$. Taking the appropriate logarithmic derivative yields

$$\frac{1}{\nu\psi}=\frac{d\ln S}{d\ln[\ln\left(T_0/T\right)]}. \tag{6}$$

If there are no corrections to scaling this value will not depend upon temperature. An extra complication stems from the microscopic scale, T_0, which is an additional fitting parameter.

Let us now work out what happens if one insists on analyzing data that follow the activated scaling form by using the procedure for power-law scaling. In other words, we calculate the logarithmic derivative w.r.t. T of the slope given in Eq. 5:

$$\left(\frac{1}{\nu z}\right)_{\text{eff}} = -\frac{d\ln S}{d\ln T} \tag{7}$$

$$= -\frac{d}{d\ln T}\ln\left[\phi'(0)\left(\ln\frac{T_0}{T}\right)^{\frac{1}{\nu\psi}}\right] \tag{8}$$

$$= -\frac{d}{d\ln T}\left[\frac{1}{\nu\psi}\ln\left(\ln\frac{T_0}{T}\right)\right]. \tag{9}$$

This becomes

$$\begin{aligned}\left(\frac{1}{\nu z}\right)_{\text{eff}} =& -\frac{1}{\nu\psi}\frac{1}{\ln(T_0/T)}\frac{d\ln(T_0/T)}{d\ln T}\\ =& \frac{1}{\nu\psi}\frac{1}{\ln(T_0/T)},\end{aligned} \tag{10}$$

which completes the derivation of Eq. 4.6.

The r.h.s. of the last expression vanishes in the limit of zero temperature, which means that νz determined in this manner would diverge in the zero-temperature limit.

A similar result is obtained if corrections to scaling are included in the derivation, where the corrections are due to a leading irrelevant variable, u. Near an infinite randomness critical point the inverse disorder strength serves as an irrelevant scaling variable. The form then becomes

$$R\left(\delta, \ln\frac{T_0}{T}, u\right) = \bar{\Phi}\left[\delta\left(\ln\frac{T_0}{T}\right)^{\frac{1}{\nu\psi}}, u\left(\ln\frac{T_0}{T}\right)^{-\frac{\omega}{\psi}}\right] \tag{11}$$

where the exponent $\omega > 0$. We expand the scaling function in the second argument,

such that

$$R\left(\delta, \ln\frac{T_0}{T}, u\right) = \Phi\left[\delta\left(\ln\frac{T_0}{T}\right)^{\frac{1}{\nu\psi}}\right] + u\left(\ln\frac{T_0}{T}\right)^{-\frac{\omega}{\psi}}\Phi_u\left[\delta\left(\ln\frac{T_0}{T}\right)^{\frac{1}{\nu\psi}}\right] \tag{12}$$

where both Φ and Φ_u are unknown functions.

One consequence of this corrected scaling form is that R is not temperature-independent at $\delta = 0$, as in Eq. 4. Instead, $R(0, \ln T_0/T, u) = R_c + u(\ln T_0/T)^{-\omega/\psi}\Psi_n(0)$, where R only approaches R_c as $T \to 0$. A second consequence is that $R(\delta)$ curves at finite temperatures do not cross right at $\delta = 0$. The crossing points shift as a function of temperature, and approach $\delta = 0$ in the $T \to 0$ limit.

The temperature-dependence of the crossing points, $B_x(T)$, can be determined by expanding the scaling functions in Eq. 12 linearly around $\delta = 0$ and determining where two isotherms cross. Let us take isotherms at T and $2T$, though any multiplier can be used, and determine where

$$\begin{aligned} &R_c + \delta\left(\ln\frac{T_0}{T}\right)^{\frac{1}{\nu\psi}}\Phi'(0) + u\left(\ln\frac{T_0}{T}\right)^{-\frac{\omega}{\psi}}\Phi_u(0) \\ &= R_c + \delta\left(\ln\frac{T_0}{2T}\right)^{\frac{1}{\nu\psi}}\Phi'(0) + u\left(\ln\frac{T_0}{2T}\right)^{-\frac{\omega}{\psi}}\Phi_u(0). \end{aligned} \tag{13}$$

Critical resistance R_c here is the value at the critical point without corrections, as in Eq. 4. This equation can be rearranged and simplified by making the approximation

$$\begin{aligned} \left(\ln\frac{T_0}{2T}\right)^{\frac{1}{\nu\psi}} &= \left(\ln\frac{T_0}{T} - \ln 2\right)^{\frac{1}{\nu\psi}} \\ &= \left(\ln\frac{T_0}{2T}\right)^{\frac{1}{\nu\psi}}\left(1 - \frac{\ln 2}{\ln T_0/T}\right)^{\frac{1}{\nu\psi}} \\ &\approx \left(\ln\frac{T_0}{2T}\right)^{\frac{1}{\nu\psi}}\left(1 - \frac{\ln 2}{\nu\psi}\frac{1}{\ln T_0/T}\right). \end{aligned} \tag{14}$$

This can be used to show that the difference between the scaling terms can be written

$$\left(\ln\frac{T_0}{T}\right)^{-\frac{1}{\nu\psi}} - \left(\ln\frac{T_0}{2T}\right)^{-\frac{1}{\nu\psi}} = -\frac{\omega\ln 2}{\psi}\left(\ln\frac{T_0}{T}\right)^{-\frac{1}{\nu\psi}-1}, \tag{15}$$

while, analogously, the correction terms can be written

$$\left(\ln\frac{T_0}{T}\right)^{-\frac{\omega}{\psi}} - \left(\ln\frac{T_0}{2T}\right)^{-\frac{\omega}{\psi}} = -\frac{\omega\ln 2}{\psi}\left(\ln\frac{T_0}{T}\right)^{-\frac{\omega}{\psi}-1}. \tag{16}$$

This can be inserted into the crossing condition, Eq. 13, to show that the crossing points vary with temperature as

$$\delta_x(T) \sim u\left(\ln\frac{T_0}{T}\right)^{-\frac{1}{\nu\psi}-\frac{\omega}{\psi}} \tag{17}$$

where $\delta_x(T) = ((B_c - B_x(T))/B_c$ and $B_x(T)$ is the crossing point. Deviation of the crossing point δ_x vanishes as $T \to 0$.

By following a calculation similar to that leading to Eq. 10, it can also be shown that if the data are analyzed using power law scaling at the crossing points,

$$\left(\frac{1}{\nu z}\right)_{\text{eff}} = \left(\frac{1}{\nu\psi}\right)_{\text{eff}}\frac{1}{\ln(T_0/T)}, \tag{18}$$

where

$$\left(\frac{1}{\nu\psi}\right)_{\text{eff}} = \frac{1}{\nu\psi} - \frac{a\omega}{\psi}\left(\ln\frac{T_0}{T}\right)^{-\frac{\omega}{\psi}}, \tag{19}$$

where $a = (c\Phi''_u(0) + u\Phi'_u(0))/\Phi'(0)$. In the limit of $T \to 0$, $(1/\nu z)_{\text{eff}} \to 0$ and $(1/\nu\psi)_{\text{eff}} \to 1/\nu\psi$.